Chapter 7

Effect of Ice and Hydrate Formation on Thermal Conductivity of Sediments

Evgeny Chuvilin, Boris Bukhanov, Viktor Cheverev,
Rimma Motenko and Erika Grechishcheva

Additional information is available at the end of the chapter

http://dx.doi.org/10.5772/intechopen.75383

Abstract

Thermal conductivity of ice- and hydrate-bearing fine-grained porous sediments (soils) has multiple controls: mineralogy, particle size, and physical properties of soil matrix; type, saturation, thermal state, and salinity of pore fluids; and pressure and temperature. Experiments show that sediments generally increase in thermal conductivity upon freezing. The increase is primarily due to fourfold difference between thermal conductivity of ice and water (~2.23 against ~0.6 W/(m·K)) and is controlled by physicochemical processes in freezing sediments. Thermal conductivity of frozen soils mainly depends on lithology, salinity, organic matter content, and absolute negative temperature, which affect the amount of residual liquid phase (unfrozen water). It commonly decreases as soil contains more unfrozen water, in the fining series 'fine sand – silty sand – sandy clay – clay', as well as at increasing temperatures, salinity, or organic carbon contents. According to experimental evidence, the behavior of thermal conductivity in hydrate-bearing sediments strongly depends on conditions of pore hydrate formation. It is higher when pore hydrates form at positive temperatures ($t > 0^{o}C$) than in the case of hydrate formation in frozen samples. Freezing and thawing of hydrate-bearing sediments above the equilibrium pressure reduces their thermal conductivity due to additional hydrate formation.

Keywords: thermal conductivity, sediments, temperature, ice, gas hydrate, freezing, permafrost, unfrozen water, salinity, hydrate saturation, organic matter

1. Introduction

Thermal conductivity of rocks depends on their origin and deposition environments and related lithology, mineralogy, structure and texture, as well as on thermal state and thermodynamic conditions [1–13]. There is a wealth of published evidence on thermal conductivity control by mineralogy, particle size, pore space structure, and pore fluid state and composition: whether it is fresh or saline water, ice, gas, organic compounds, and so on [14–21]. However, the effect of some pore filling materials on thermal properties of sediments remains poorly investigated, especially that of pore hydrates [22, 23]. Natural gas hydrates share much physical similarity with ice (heat capacity, density, and acoustic properties) and thus pore hydrates in permafrost, though being known since the 1970s [24], are hard to identify and study with conventional geophysical methods, mainly seismic. Meanwhile, pore gas hydrate and ice differ markedly in thermal conductivity, which is 2.23 W/(m·K) in hydrate, 0.54–0.65 W/(m·K) in ice, and 0.6 W/(m·K) in liquid water [25–27].

Knowledge of thermal properties, especially thermal conductivity, of frozen and freezing porous sediments is valuable in geocryological predictions for reducing geological engineering risks during construction and operation of buildings and utilities in regions of Arctic and highland permafrost [28, 29]. True thermal conductivity values of frozen soils are also indispensable to choose optimal strategies of mitigating risks from permafrost thawing as a result of global warming or local manmade impacts.

The development of hydrate-bearing gas and oil reservoirs likewise requires knowing their thermal properties [30]. Methane production from these reservoirs is most often simulated with reference to thermal conductivity of pure methane hydrates [31], but this simplistic assumption can entrain serious errors during methane recovery, especially for permafrost containing hydrates and ice.

The marked thermal conductivity difference between hydrate and ice is a prerequisite for creating a method of identifying and mapping intra-permafrost gas hydrates.

2. Thermal conductivity of sediments in unfrozen and frozen state and freezing effect

Thermal properties of rocks, soils, water, and air vary as a function of their composition, structure and state, as well as thermodynamic conditions. Thermal conductivity values of different materials are quoted in **Table 1** per unit volume of rocks, sediments, water, ice, snow and air. Note that it linearly depends on temperature for water, ice and air.

Comparative analysis of experimental data shows that thermal conductivity of igneous (granite, basalt), metamorphic (quartzite, schists), and sedimentary (sandstone, limestone, dolomite) rocks can vary from 1.0 to 5.0 W/(m·K) as a function of different factors. The mineralogy dependence is associated with the presence of thermally conductive minerals, such as SiO_2 quartz (~7.0 W/(m·K)) or iron-bearing phases (e.g., pyrite). Density and porosity effects appear as greater thermal conductivity in denser and less porous rocks, that is, it is lower in sediments than in igneous or metamorphic rocks. Experiments show that 15–20% densening of skeleton in sand leads to about twice higher thermal conductivity. The variations result from more or less close packing of particles. Manmade compaction likewise leads to thermal conductivity increase in sediments, which is often used in civil engineering.

Cemented porous sediments fall into three thermal conductivity groups: (1) coarse clastics (conglomerates, gritstones, and sandstones); (2) fine clastics (silt and clay); (3) chemogenic and biogenic carbonates and silicates (dolomite, anhydrite, limestone, diatomite, etc.). Thermal conductivity of coarse clastics is from 1.5 to 4.5 W/(m·K), estimated separately for matrix and cement, and reaches 5.8 W/(m·K) in low-porosity monomineral sediments (dolomite, limestone). Thermal conductivity is anizotropic in many sedimentary and metamorphic rocks: it is on average 10–30% higher along than across the bedding, especially in shale and gneiss [32]. The reason is that interactions of mineral particles and heat transfer are more active along the bedding controlled by the origin and deposition environments of rocks.

Thermal conductivity variations in sediments and soils, which are multicomponent and multiphase systems, depend on relative percentages of solid, liquid, and gas phases; soil chemistry and mineralogy; structure and texture (particle size, porosity, layering, etc.); moisture contents; and temperature. Saturation of sediments affects significantly their thermal properties: thermal conductivity reaches its maximum at full water saturation [11] as water with $\lambda = 0.54$ (W/(m·K) supplants gas with $\lambda = 0.024$ (W/(m·K).

The dependence on particle size composition shows up in higher thermal conductivity of coarse and very coarse soils (of boulder, pebble, gravel, and sand particles) compared to finer-grained varieties, the moisture content, density, and other parameters being equal. The upper limit for coarse sediments (up to 3–9 W/(m·K)) corresponds to hard components while the lower limit (0.3–0.5 W/(m·K)) represents dry fine-grained material. Thermal conductivity decreases with fining, in a descending series of sand – silt – clay – peat (**Table 1**), because of a greater number of loose contacts between particles [33].

Saturated frozen sediments and soils with medium or high moisture contents have higher thermal conductivity than their unfrozen counterparts because pore ice is four times more conductive than water (**Table 1**): 2.22 W/(m·K) against 0.54 W/(m·K). However, the temperature dependence of thermal conductivity in wet porous sediments is rather controlled by relative percentages of pore ice and water and conditions of heat transfer at their contacts. Within the range of positive temperatures, thermal conductivity decreases slowly from 25 to 0°C, in accordance with linear dependence on water temperature, but rises abruptly at the transition from 0 to –1°C when pore water rapidly converts to ice (**Figure 1**). Note that thermal conductivity of ice-rich soil depends more on the conditions of cooling and heating than on absolute temperature. Of special importance is the direction of heat transfer at alternating pressures and temperatures, when pore water converts to ice and back, and changes in their relative amounts [15]. **Figure 2** shows qualitative variations of thermal conductivity in frozen sediments subject to further freezing and subsequent thawing. The curves comprise several segments corresponding to different temperature intervals. Thermal conductivity decreases linearly within the range of positive temperatures till the onset of freezing (segment A-B) and then increases dramatically in the region of rapid water-to-ice transition (segment B-C), when ice, with its thermal conductivity four times that of water, appears as a new pore filling component, while the amount of unfrozen pore water reduces. Further freezing to –15°C and colder (segment C-D) corresponds to notable (30–40%) decrease in thermal conductivity. The reason is that increasing crystallization of unfrozen bound water and related thermomechanic stress, as well as thermal expansion variations, cause rapid growth of cracks. Saline

Material	Thermal conductivity λ (W/(m·K))
Water	
At +4.1°C	0.54
At +20°C	0.60
Ice	2.22–2.35
Air	
At 0°C	0.024
At −23°C	0.022
Snow	
Loose	0.1
Dense	0.3–0.4
Granite	2.3–4.1
Basalt	1.74–2.91
Quartzite	2.9–6.4
Shale	1.74–2.33
Sandstone	0.7–5.8
Limestone	0.8–4.1
Dolomite	1.1–5.2
Sand	
Dry	0.3–0.35
Unfrozen, water-saturated	1.7–2.6
Frozen, ice-saturated	1.5–3.0
Silty clay	
Dry	0.19–0.22
Unfrozen, water-saturated	0.6–1.0
Frozen, ice-saturated	1.2–1.4
Clay	
Air-dry	0.8–1.0
Unfrozen, water-saturated	1.2–1.4
Frozen, ice-saturated	1.4–1.8
Peat	
Dry	0.012–0.14
Unfrozen, water-saturated	0.7–0.9
Frozen, ice-saturated	1.1–1.2

Table 1. Thermal conductivity of different materials [19].

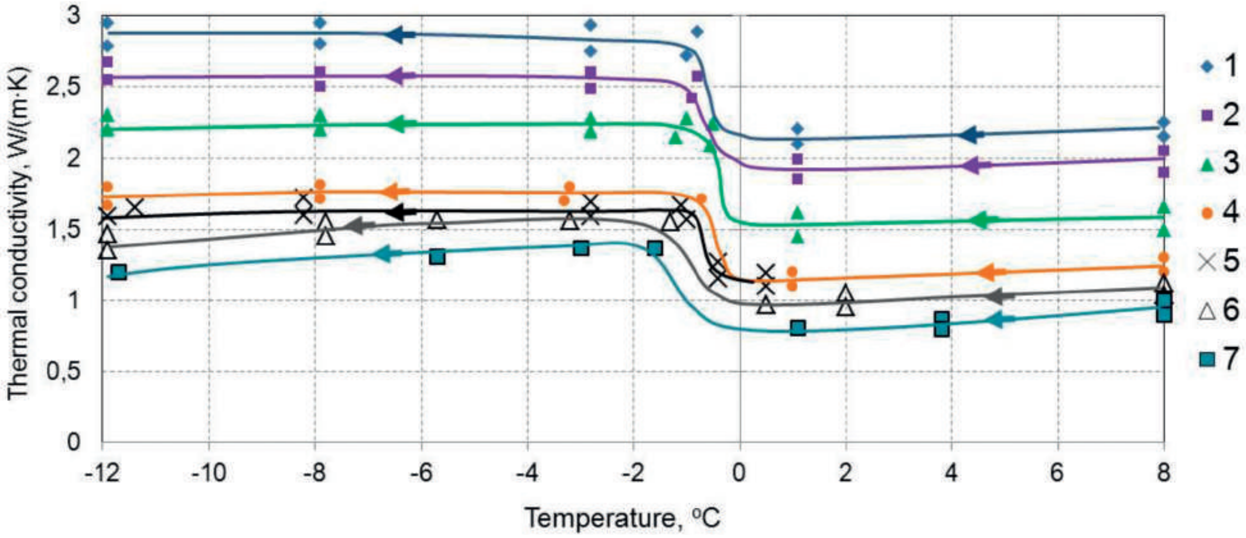

Figure 1. Effect of temperature on thermal conductivity in different types of sediments: 1—coarse crushed stone filled with silt, 2—fine sand, 3—silty sand, 4—loess-like silty clay, 5—silty clay, 6—clay, and 7—degraded peat [15, 19]. Data points are experimental measurements; lines are approximation trends. The arrows show the direction of temperature change.

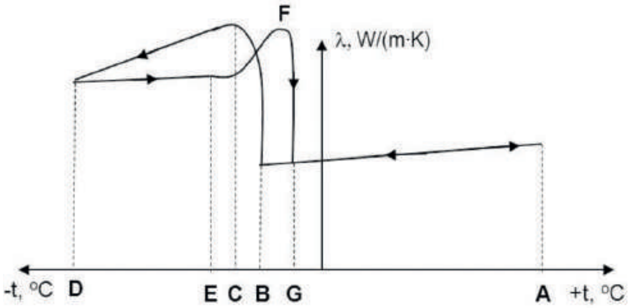

Figure 2. Variations of thermal conductivity in frozen sediments subject to freezing and subsequent thawing. The arrows show the direction of temperature change.

peat-bearing fine-grained porous soil contains much unfrozen water even at low negative temperatures, till –15°C [16, 19, 34]. The thermal conductivity reduction is especially large in ice-rich peat subject to further cooling and related brittle deformation when internal stress in soil releases through microcracks.

Subsequent warming (segment E-F) leads to notable increase in thermal conductivity as the cracks heal up because ice, and soil as a whole, become more plastic. The highest thermal conductivity values in the warming-thawing cycle of frozen soil approach those in the freezing-cooling cycle, but correspond to higher negative temperatures because of hysteretic behavior of moisture phases. Thermal conductivity decreases dramatically till the thawing temperature within the segment F-G, as pore ice melting increases the contents of liquid water.

The thermal conductivity decreases with grain sizes in the series 'coarse sand – fine sand – silty sand – silt – silty clay – clay' was observed in both frozen and unfrozen sediments with different degrees of water or ice saturation [15, 17–21], over the range of temperatures from +20 to -20 °C, including the region of rapid water-ice phase transitions. Finer sediments have more thermal resistance contacts and are more hydrophilic and ultraporous, which increases relative contents of low-conductive liquid unfrozen water.

Thermal conductivity of frozen sediments increases systematically with ice saturation as low-conductivity gas gives way to high-conductivity ice. Sediments with high contents of ice, which swells out the mineral skeleton, have thermal conductivity about that of ice.

Salinity, or the presence of soluble salts in pore water, is another important control of thermal conductivity in frozen sediments. Namely, Na+ and Cl- ions lead to changes in the phase state of pore moisture in permafrost. Frozen soils with higher salinity (Z, %), that is, salt-to-dry sediment weight ratio, contain more unfrozen pore water and, correspondingly, have lower thermal conductivity (**Figure 3**). Thermal conductivity of saline sand and silty sand containing liquid pore water is much lower than that in non-saline sediments: only 1% increase of salinity in frozen sand may cause twofold thermal conductivity decrease. Unlike sand, more or less water-saturated low saline (0 to 0.5-0.7%) clay silt and clay have thermal conductivity slightly (within 10%) higher than in their non-saline counterparts, but more saline varieties are less conductive. Namely, at Z > 1%, thermal conductivity shows a weak decreasing trend traceable until the system reaches the eutectic point. This behavior is related primarily with changes in relative contents of water phases (ratio of unfrozen water content to total moisture content) as salinity increases. The amount of liquid water depends on concentration as well as on chemistry of salts: it increases progressively in the series Na_2SO_4-Na_2CO_3-$NaNO_3$-NaCl, while thermal conductivity decreases correspondingly. Note that further cooling of frozen soils reduces the amount of unfrozen pore water [34]. As the pore fluid reaches eutectic concentration and temperature, salts form cryohydrates, whereby the content of unfrozen water decreases dramatically. The formation of thermally conductive cryohydrates in the pore space and the respective reduction of the liquid water content leads to thermal conductivity increase in frozen soils. Experiments show that thermal conductivity of saline soils tends to that of non-saline soils at temperatures below eutectics [35].

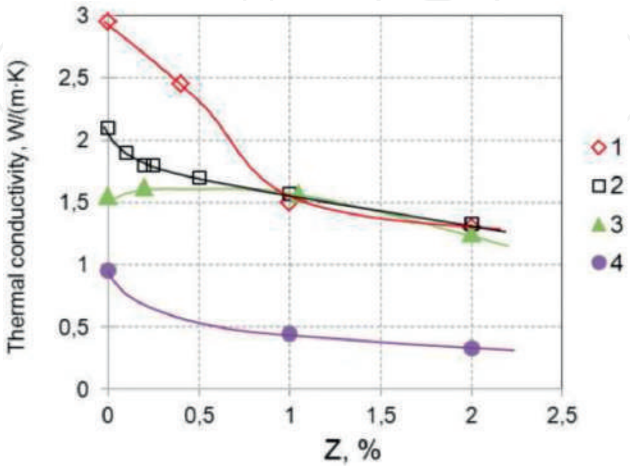

Figure 3. Salinity (Z,%) dependence of thermal conductivity for different types of NaCl-bearing soil: 1—fine sand, 2—silty sand, 3—sandy clay, and 4—kaolin clay (W = 15–30% for 1–3 and W = 50–70% for 4) [18]. Data points are experimental measurements; lines are approximation trends.

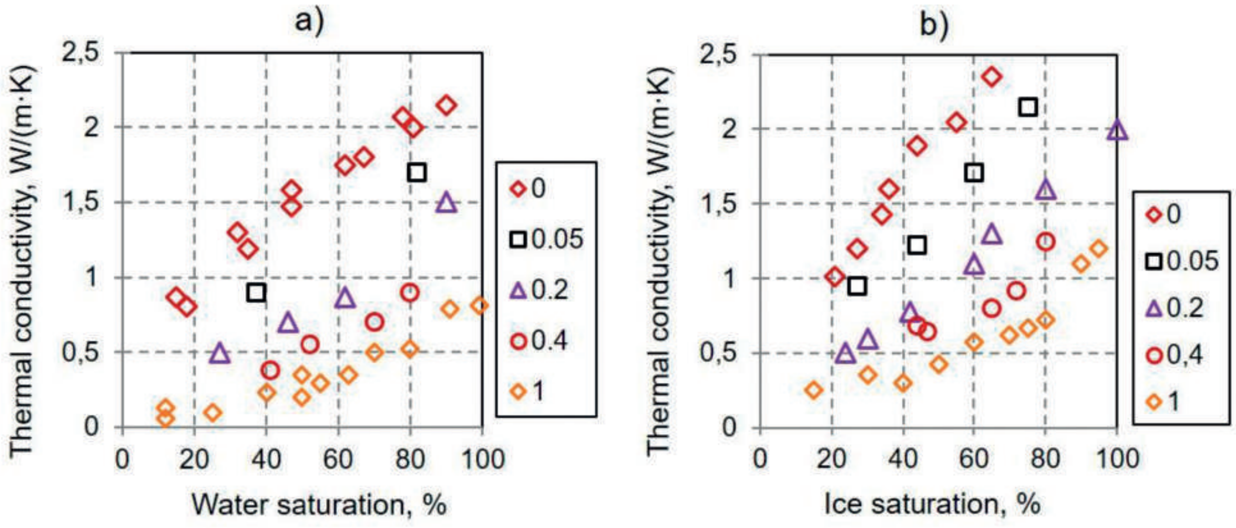

Figure 4. Water (a) and ice (b) saturation dependence of thermal conductivity in unfrozen and frozen peat-bearing sandy soils with different peat contents [36] (found as organic component to total sediment dry weight ratio).

Thermal conductivity is lower in frozen sediments containing organic matter (especially, peat) (**Figure 4**). This is because the presence of peat increases specific surface activity and the contents of unfrozen pore water, and the organic component itself (peat, oil, etc.) most often has lower thermal conductivity than mineral particles and ice. Therefore, unfrozen water-saturated soils with organic-filled porosity likewise have low thermal conductivity.

Unlike heat capacity, thermal conductivity is not an additive value but depends on sediment structure and texture. As shown by experiments, massive frozen clay is more conductive than that with ice lenses at similar water contents and density. Note that thermal conductivity of sediments with lenticular cryostructure is anisotropic: it is 20–30% higher at heat flux along than across ice lenses. The reason is in higher thermal conductivity of ice and lower thermal resistance at contacts between mineral layers and ice lenses.

3. Thermal conductivity of gas hydrate-bearing sediments and hydrate-accumulation effect

Thermal conductivity has been worse studied in hydrate-bearing sediments than in frozen (ice-bearing) sediments: the available data are limited to sporadic estimates for manmade hydrate-bearing materials [37–41]. The first experimental evidence on thermal conductivity of sediments containing natural gas hydrates was obtained from well Malik 5L-38 (Mackenzie Delta, Canada). Ice-bearing soils were found to have thermal conductivity generally higher than their hydrate-bearing counterparts [42]. On the other hand, frozen hydrate-saturated sediments are often more thermally conductive than those in the unfrozen state. New experimental data on thermal conductivity of natural gas hydrate-bearing sediments from the Nankai Trough published a few years ago were used to predict thermal conductivity from the known particle size distribution, porosity, and hydrate saturation [43]. The most successful prediction for natural sediments with hydrate saturation within 14% was achieved with a model of complex distribution (geometric mean), but the proposed equations were poorly applicable to sediment samples containing greater percentages of hydrates (up to 30%) [44]. This is because hydrate-bearing sediments are actually complex systems and their thermal conductivity is not a sum of values for the system constituents but rather depends on the pore space structure.

According to experimental evidence, hydrate formation conditions influence largely the thermal conductivity of hydrate-bearing sediments [45]. Its variations were studied at different conditions of hydrate formation: (1) low positive temperatures (t ≈ +2 ± 1°C), (2) negative temperatures (t ≈−5 ± 1°C), (3) cooling from +2 ± 1 to −5 and −8°C, where residual pore water (not converted to hydrate at positive temperatures) froze and induced additional hydrate formation, and (4) warming from −5 ± 1 to +2 ± 1°C, where residual pore ice (not converted to hydrate at negative temperatures) thawed and induced additional hydrate formation.

3.1. Hydrate formation at t > 0°C

First, the effect of gas hydrate formation at t > 0°C on thermal conductivity of hydrate-bearing sediments was studied at low positive temperatures (t = +2 ± 1°C). The typical pattern of pore hydrate formation, under favorable conditions, is evident in time-dependent variations in the fraction of pore space occupied by hydrates or hydrate saturation (S_h, %) (**Figure 5**). This fraction decreases with time as a result of changes in the hydrate formation mechanism. Hydrate formation is rapid early during the process, and most of hydrate forms within the first 45–50 h, while S_h (**Figure 5**) reaches 67%. Then hydrate formation decelerates, while S_h remains almost invariable (about 67%). The observed kinetics of hydrate formation at low positive temperatures can be explained as follows. Rapid formation of hydrates in the beginning is due to direct gas-water contacts. Later, a gas hydrate film forms at the pore water-gas interface and impedes gas access to pore water, whereby the hydrate formation rate slows down, being limited by the permeability of the gas hydrate film. The thickening of the hydrate film makes it much less permeable, and hydrate formation almost stops at a certain film thickness, despite the fact that the residual pore water content exceeds its equilibrium content at the given temperatures and pressures.

The time-dependent behavior of thermal conductivity during hydrate accumulation in gas-saturated silty sand (W = 18%) at positive temperatures is irregular (**Figure 6**). The curve

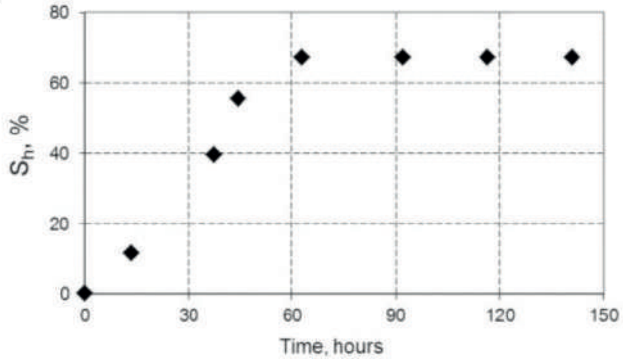

Figure 5. Pore hydrate formation in gas-saturated silty sand (W = 18%; n = 0.40), at t = +2 ± 1°C: time-dependent hydrate saturation (S_h, %) [45].

comprises three characteristic segments: (1) thermal conductivity (λ) changes little (1.77–1.78 W/(m·K) or within a measurement accuracy of 3%) for the first 40 h, but (2) becomes 13% higher (1.78–2.01 W/(m·K)) for the following 20 h, and (3) remains almost invariable about 2.01 W/(m·K), with 3–4% variations (within a measurement accuracy) till 60 h after the run start. While thermal conductivity almost does not change for the first 40 h, saturation (S_h) becomes 40% higher than at the run onset; then both parameters increase for the following 20 h, peak concurrently, and remain invariable within 100 h afterward.

At gas saturation S_h within 45%, thermal conductivity does not change (**Figure 7**), as reported previously [42–44]. The variations become notable when hydrates occupy more than 45% of the pore space. For instance, thermal conductivity became 14% higher, while Sh reached 61% in silty sand (W = 18%) and 9% higher as S_h increased to 57% in fine sand.

3.2. Hydrate formation at t < 0°C

Hydrate formation at t < 0°C was studied in frozen methane-bearing samples in a pressure cell, at temperatures of −5 ± 1°C (**Figure 8**). Unlike the tests at low positive temperatures, methane hydrates form more slowly at negative temperatures. As a result, the rate of hydrate formation in frozen samples is commensurate with that at positive temperatures for quite a long time. The reason is that, at negative temperatures, gas hydrates form directly on the surface of ice particles, as demonstrated by special studies of interaction between ice particles and CO_2 and CH_4 gases [46, 47]. Hydrate that forms during this interaction has a low density, and, hence, a high permeability and does not impede much the conversion of ice particles to hydrate. The same mechanism apparently works during transition of pore ice into hydrate, judging by the dynamics of gas hydrate formation in frozen sediments. Unlike the case of t > 0°C, the thermal conductivity of frozen samples decreases nonuniformly with time during hydrate formation (**Figure 9**). The decrease is to 1.81 W/(m·K) (8%) for the first 50 h of hydrate growth and then as small as 3% for the subsequent 125 h. In general, this decrease is observed in the S_h range from 0 to 50–60% (**Figure 10**). The thermal conductivity decrease most likely results from reduction in the amount of ice, with its thermal conductivity as high as 2.23 W/(m·K), and the related growth in the share of the less conductive hydrate (0.6 W/(m·K)).

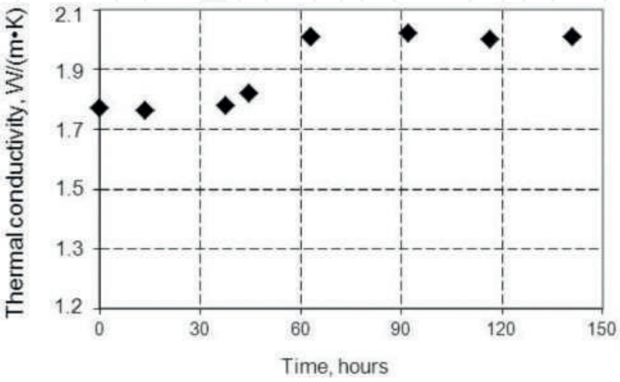

Figure 6. Time-dependent thermal conductivity of gas-saturated silty sand (W = 18%; n = 0.40) during hydrate formation at t = +2 ± 1°C [45].

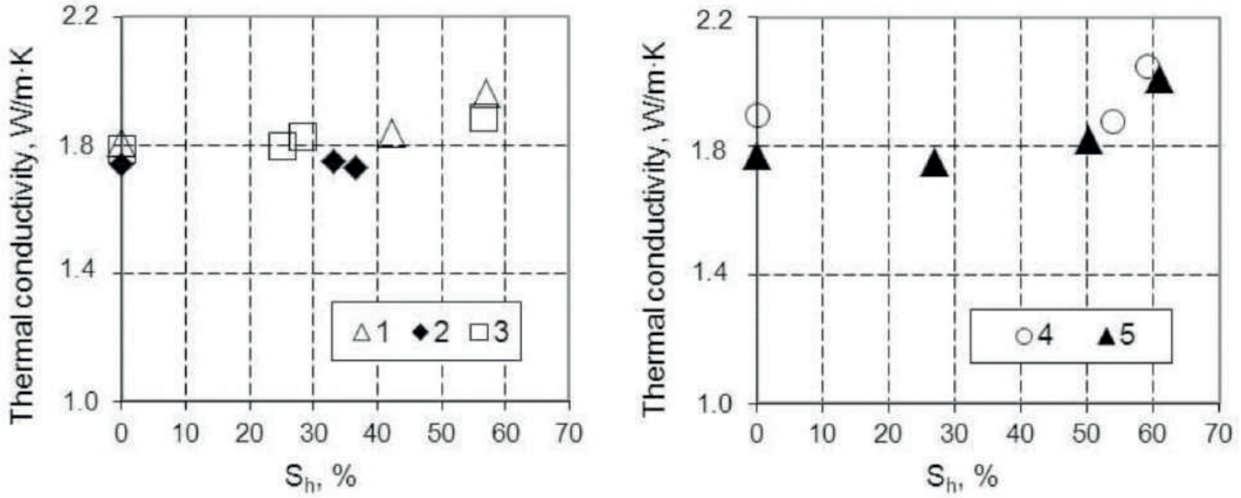

Figure 7. Thermal conductivity of sediments as a function of hydrate saturation (S_h, %) at t = +2 ± 1°C: (1) fine sand, W = 16%; (2) fine sand, W = 10%; (3) fine sand, W = 15%; (4) fine sand +14% kaolin clay, W = 15%; and (5) silty sand, W = 18% [45].

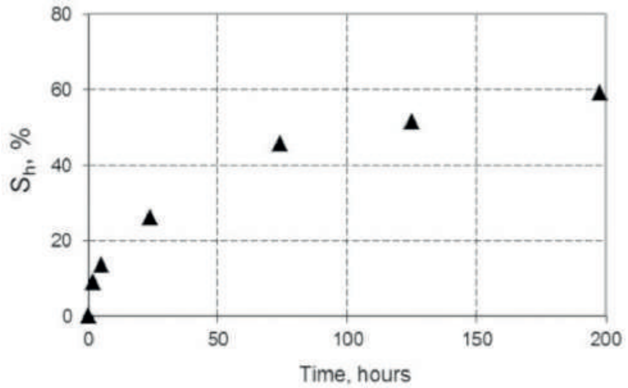

Figure 8. Pore methane hydrate formation in frozen fine sand (W = 22%; n = 0.60) at t = −5 ± 1°C: time-dependent hydrate saturation (S_h, %) [45].

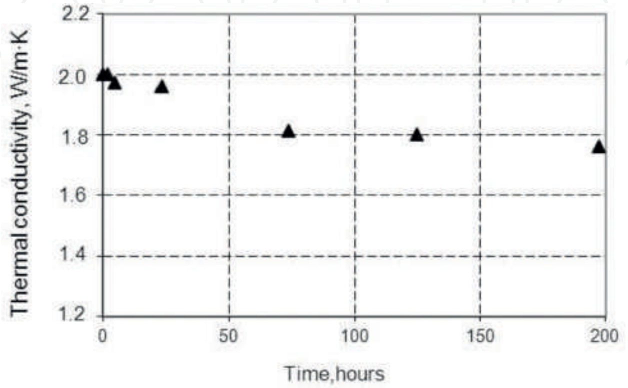

Figure 9. Time-dependent thermal conductivity of gas-saturated fine sand (W = 22%; n = 0.60) during hydrate formation at t = −5 ± 1°C [45].

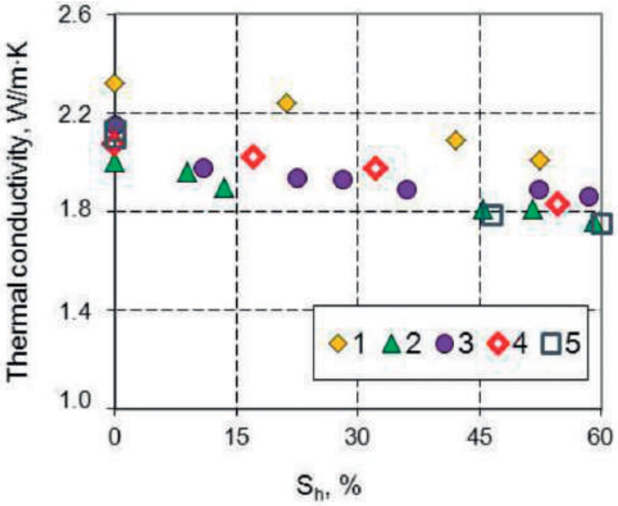

Figure 10. Thermal conductivity of sediments as a function of hydrate saturation (S_h, %), at t = −5 ± 1°C: (1) fine sand, W = 19% and n = 0.40; (2) fine sand, W = 22% and n = 0.60; (3) fine sand, W = 15% and n = 0.38; (4) silty sand, W = 24% and n = 0.60; and (5) silty sand, W = 16% and n = 0.38 [45].

3.3. Effect of freezing

To study the effects of freezing on thermal conductivity, the samples saturated with hydrate at t > 0°C were cooled from −5 to −8°C. Although hydrate had already saturated 50–60% of the pore space before freezing and the hydrate formation almost ceased, the samples produced additional pore hydrate upon further cooling, in all runs (**Table 2**), more in silty sand than in fine sand. Thus, a large portion of residual water that survived conversion to hydrate at positive temperatures became consumed during cooling and freezing. Hydrate formation became more active as the survived pore water froze up because cryogenic deformation of the soil skeleton and release of dissolved gas produced new water-gas interfaces. The amount of hydrate additionally formed as a result of freezing mainly depends upon soil mineralogy, clay content, and water saturation.

Thermal conductivity decreased dramatically in freezing hydrate-saturated sediments (**Figure 11** A) but became 15–20% higher in hydrate-barren samples (**Figure 11** B). The freezing-induced thermal conductivity reduction was 10% in fine sand (from 1.96 to 1.77 W/(m·K)) but reached 50% in silty sand with W = 16% (2.01–0.96 W/(m·K)) [45].

Type of soil	W (%)	S_h (%)	
		Before freezing	After freezing
Fine sand	16	58	71
Fine sand +14% kaolin	15	62	79
Silty sand	18	61	85
Silty sand	16	52	79

Table 2. Methane hydrate formation upon freezing of residual pore water [45].

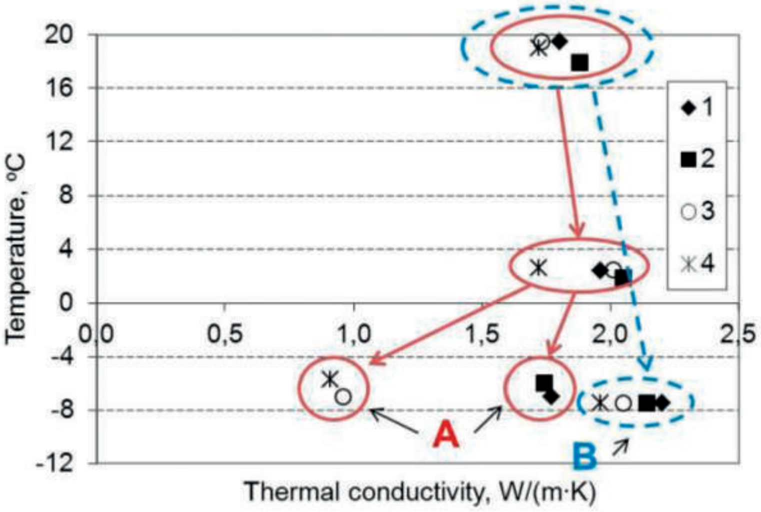

Figure 11. Variations in thermal conductivity of gas-saturated sediments upon cooling (to +2°C) and freezing: (A) hydrate-bearing samples after freezing and (B) frozen hydrate-barren samples. Solid (red) and dash (blue) lines correspond to samples saturated with gases that can and cannot form hydrates (methane and nitrogen, respectively): (1) fine sand, W = 16%; (2) fine sand +14% kaolin, W = 15%; (3) silty sand, W = 18%; and (4) silty sand, W = 16%.

Thus, thermal conductivity may decrease dramatically in hydrate-saturated sediments exposed to further freezing, whereby the survived pore water freezes up, as a result of additional hydrate formation. This behavior may be due to structure and texture changes in freezing gas- and hydrate-bearing sediments. These are especially the effects of heaving or cracking of hydrate-saturated soil or the formation of highly porous hydrate at grain boundaries, with thermal conductivity as low as ~0.35 W/(m·K).

3.4. Effect of thawing

To study the effect of thawing on the behavior of thermal conductivity, the frozen sand samples that were saturated with hydrate at t < 0°C were heated to +2 ± 1°C. The tests showed additional hydrate formation in fine sand (**Table 3**), as in the case of freezing, but unlike the latter case, it did not exceed 10% [45]. Faster hydrate generation upon thawing was attributed to deformation of soil skeleton and formation of new water-gas interfaces. Additional hydrate formation upon thawing of hydrate-saturated sand was more intense in the initially water-saturated samples: 10 and 7% of additional hydrate formed in sandy samples with W = 19 and 15%, respectively. As the frozen hydrate-bearing samples thawed, their thermal conductivity

Type of sediment	W (%)	S_h (%)		Thermal conductivity (W/(m·K))	
		Before thawing	After thawing	Before thawing	After thawing
Fine sand	19	0.64	0.71	1.80	1.70
Fine sand	15	0.57	0.61	1.86	1.76

Table 3. Thermal conductivity and hydrate saturation of frozen hydrate-bearing sand upon thawing (to +2 ± 1°C) at above-equilibrium methane pressure [45].

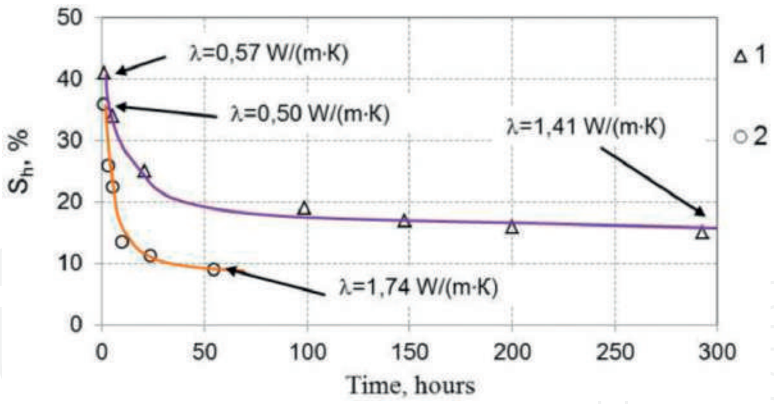

Figure 12. Thermal conductivity variations of frozen hydrate-contain sands during methane hydrate dissociations at t = −5 to −6°C and pressure 0.1 MPa: Data points (triangles and circles) are experimental measurements; lines are approximation trends: (1) fine sand, W = 17% and n = 0.40; (2) silty sand, W = 17% and n = 0.40.

decreased (from 1.86 to 1.72 W/(m·K) or for 8%). Two main reasons of such reduction are (1) thermal conductivity difference between pore ice and water and (2) hydrate saturation increase.

Thus, both freezing and thawing cause thermal conductivity reduction in frozen soils saturated with methane hydrate at above-equilibrium pressures.

The observed thermal conductivity variations associated with hydrate formation at different conditions (low positive and negative temperatures, freezing and thawing) indicate that this behavior is mostly controlled by phase transitions in pore fluids and by structure and texture changes in main sample constituents, which were explained by Chuvilin and Bukhanov [45] in two models of structure and texture changes in gas-saturated sediment during hydrate formation. These models can be used for reference in geomechanical and thermal simulations of gas hydrate reservoirs, taking into account the conditions of pore hydrate formation, with implications for methane recovery.

3.5. Effect of hydrate dissociation

The effect of hydrate dissociation on thermal conductivity of frozen hydrate-bearing soils at below-equilibrium pressure was investigated in manmade sand samples at temperatures about −5 to −6°C and atmospheric pressure [48]. Pore hydrates in the frozen sand samples failed to reach complete decomposition in the experiments due to their self-preservation [49–52], with residual hydrate saturation (S_h, %) up to 10% or more (**Figure 12**). The hydrate dissociation was attendant with notable increase in thermal conductivity; it became 2.5 times higher (from 0.57 W/(m·K) to 1.41 W/(m·K) as S_h reduced from 40 to 15%) in fine sand and more than three times higher as S_h became 10% in silty sand. Thermal conductivity increase in the end of the experiment was due to decrease in the amount of pore hydrate and increase in pore ice, with residual hydrate saturation (Sh, %) of 10% (**Figure 11**). Low thermal conductivity of frozen hydrate-bearing samples (0.5–0.6 W/(m·K)) for first few minutes after the equilibrium pressure drop to the atmospheric value (0.1 MPa) may result from both high contents of pore hydrate and formation of microcracks in this hydrate which heal up afterward during its dissociation [53].

4. Conclusions

Thermal conductivity of wet porous fine-grained soils depends on particle size, mineralogy, pore space structure, and moisture contents, as well as on the phase state and phase change of pore fluids. The effects of water→ice, water→gas hydrate, and ice→gas hydrate transitions were studied in experiments, which show the phase change direction and relative contents of water phases in the pore space to be principal controls of thermal conductivity. It increases in wet porous sediments subject to freezing and subsequent cooling, primarily, due to pore water-to-ice conversion at a wide range of negative temperatures. However, the process may induce microcracking, which may reduce thermal conductivity.

Thermal conductivity of frozen sediments mainly depends on lithology, salinity, organic matter content, and absolute negative temperature, which affect the amount of residual liquid phase (unfrozen water) in frozen soils. Namely, thermal conductivity commonly decreases as soil contains more unfrozen water, in the series 'fine sand – silty sand – sandy clay – clay', as well as at increasing salinity or organic (e.g., peat) contents.

As demonstrated by our experiments, thermal conductivity can either increase or decrease depending on hydrate formation conditions. Namely, it increases if gas hydrates form at positive temperatures ($t > 0^{o}C$) but decreases during hydrate formation in frozen samples. Freezing and thawing of hydrate-bearing sediments above the equilibrium pressure reduces their thermal conductivity due to additional hydrate formation. On the other hand, thermal conductivity of hydrate-bearing frozen sediments may increase during dissociation of pore hydrates due to their self-preservation. It increases as the pore space contains smaller amounts of hydrates but more ice which is four times more thermally conductive.

Acknowledgements

This research is supported by the Russian Science Foundation (grant no. 16-17-00051).

Author details

Evgeny Chuvilin[1,2]*, Boris Bukhanov[1], Viktor Cheverev[2], Rimma Motenko[2] and
Erika Grechishcheva[3]

*Address all correspondence to: chuviline@msn.com

1 Skolkovo Institute of Science and Technology (Skoltech), Skolkovo Innovation Center, Moscow, Russia

2 Geology Faculty, Moscow State University (MSU), Moscow, Russia

3 OJSC Fundamentproekt, Moscow, Russia

References

[1] Von-Herzen RP, Maxwell AE. The measurement of thermal conductivity of deep-sea sediments by a needle probe method. Journal of Geophysical Research. 1959;**84**:1629-1634

[2] Ivanov NS, Gavriliev RI. Thermal Properties of Frozen Rocks. Nauka: Moscow; 1965. 74 pp. (in Russian)

[3] Ivanov NS. Heat and Mass Transfers in Frozen Rocks. Novosibirsk: Nauka; 1969. 240 p. (in Russian)

[4] Sass JH, Lachenbruch AH, Munroe RJ. Thermal conductivity of rocks from measurements on fragments and its application to heat-flow determinations. Journal of Geophysical Research. 1971;**76**(14):3391-3401

[5] Farouki OT. Thermal Properties of Soils. CRREL: Hanover; 1981. 151 p

[6] Balobaev VT, Pavlov AV, Perl'shtein GZ. Thermal Study of Permafrost in Siberia. Novosibirsk: Nauka; 1983. 214 p. (in Russian)

[7] Blackwell DD, Steele JL. Thermal conductivity of sedimentary rocks: Measurement and significance. In: Naeser ND, McCulloch TH, editors. Thermal History of Sedimentary Basins. New York: Springer-Verlag; 1989. pp. 45-96

[8] Clauser C, Huenges E. Thermal conductivity of rocks and minerals. In: Ahrens TJ, editor. Rock Physics and Phase Relations: A handbook of physical constants. Washington: American Geophysical Union; 1995. pp. 105-126

[9] Beck AE. Methods for determining thermal conductivity and thermal diffusivity. In: Haenel R, Rybach L, Stegena L, editors. Handbook of Terrestrial Heat-Flow Density Determination. Dordrecht: Kluwer Academic Publisher; 1998. pp. 87-124

[10] Gavriliev RI. Thermal Properties of Rocks and Soils in Permafrost Regions. Novosibirsk: SO RAN; 1998. 208 p. (in Russian)

[11] Côté J, Konrad J-M. Thermal conductivity of base-course materials. Canadian Geotechnical Journal. 2005;**42**:61-78. DOI: 10.1139/T04-081

[12] Côté J, Konrad J-M. A generalized thermal conductivity model for soils and construction materials. Canadian Geotechnical Journal. 2005;**42**:443-458. DOI: 10.1139/T04-106

[13] Côté J, Grosjean V, Konrad J-M. Thermal conductivity of bitumen concrete. Canadian Journal of Civil Engineering. 2013;**40**:172-180. DOI: 10.1139/cjce-2012-0159

[14] Penner E. Thermal conductivity of frozen soils. Canadian Journal of Earth Sciences. 1970;**7**:982-987

[15] Ershov ED, Danilov ID, Cheverev VG. Petrography of Frozen Soils. Moscow: MSU; 1987. 311 p. (in Russian)

[16] Williams PJ, Smith MW. The Frozen Earth: Fundamentals of Geocryology. Cambridge: Cambridge University Press; 1989. 306 p

[17] Ershov ED, Komarov IA, Cheverev VG, Barkovskaya EN, Shesternev DM. Heat and mass transfer properties. In: Ershov ED, editor. Fundamentals of Geocryology. Part 2. Lithogenetic Geocryology. Moscow: MSU; 1996. pp. 118-133. (in Russian)

[18] Motenko RG. Thermal properties and phase composition of frozen saline soils [PhD thesis] Moscow: MSU; 1997. 195 p. (in Russian)

[19] Yershov ED. General Geocryology. Cambridge: Cambridge University Press; 1998. 580 p

[20] Komarov IA. Thermodynamics and Mass Transfer in Frozen Sediments. Moscow: Nauchniy Mir; 2003. 608 p. (in Russian)

[21] Cheverev VG. The Nature of Cryogenic Properties of Soils. Moscow: Nauchniy Mir; 2004. 234 p. (in Russian)

[22] Sloan ED. Clathrate Hydrates of Natural Gases. 2nd ed. New York: Marcel Dekker; 1998. 757 p

[23] Max MD, editor. Natural Gas Hydrate in Oceanic and Permafrost Environments. Boston: Kluwer Academic Publishers; 2000. 414 p

[24] Cherskiy NV, Tsarev VP, Nikitin SP. Investigation and prediction of conditions of accumulation of gas resources in gas-hydrate pools. Petroleum Geology. 1985;**21**:65-89

[25] Stoll RD, Bryan GM. Physical properties of sediments containing gas hydrates. Journal of Geophysical Research. 1979;**84**:1629-1634

[26] Rosenbaum EJ, English NJ, Johnson JK, Shaw DW, Warzinski RP. Thermal conductivity of methane hydrate from experiment and molecular simulation. The Journal of Physical Chemistry. B. 2007;**111**:13193-13205

[27] Waite WF, Stern LA, Kirby SH, Winters WJ, Mason DH. Simultaneous determination of thermal conductivity, thermal diffusivity and specific heat in sI methane hydrate. Geophysical Journal International. 2007;**169**:767-774

[28] Andersland OB, Ladanyi B. An Introduction to Frozen Ground Engineering. Dordrecht: Springer-Science + Business Media; 1994. DOI: 10.1007/978-1-4757-2290-1

[29] Muller SW. Frozen in Time: Permafrost and Engineering Problems. Virginia: ASCE; 2008. 280 p

[30] Ye Y, Liu C. Natural Gas Hydrates. Experimental Techniques and their Applications. New York: Springer; 2013. 402 p

[31] Warzinski RP, Gamwo IK, Rosenbaum EJ, Myshakin EM, Jiang H, Jordan KD, English NJ, Shaw DW. Thermal properties of methane hydrate by experiment and modeling and impacts upon technology. In: Proceeding of the 6th International Conference on Gas Hydrates; 6-10 July 2008; Vancouver; 2008

[32] Popov Y, Beardsmore G, Clauser C, Roy S. ISRM suggested methods for determining thermal properties of rocks from laboratory tests at atmospheric pressure. Rock Mechanics and Rock Engineering. 2016;**49**:4179-4207. DOI: 10.1007/s00603-016-1070-5

[33] Das BM. Advanced Soil Mechanics. 3rd ed. New York: Taylor & Francis; 2008. 567 p

[34] Istomin V, Chuvilin E, Bukhanov B, Uchida T. Pore water content in equilibrium with ice or gas hydrate in sediments. Cold Regions Science and Technology. 2017;**137**:60-67. DOI: 10.1016/j.coldregions.2017.02.005

[35] Grechishcheva E, Motenko R. Experimental study of freezing point and water phase composition of saline soils contaminated with hydrocarbons. In: Proceedings of the 7th Canadian Permafrost Conference; 21-23 September 2015; Quebec City; 2015: ABS_ 316

[36] Roman LT. Frozen Peat Soils as Foundations of Constructions. Novosibirsk: Nauka; 1987. 222 p. (in Russian)

[37] Groysman AG. Thermal Properties of Gas Hydrates. Novosibirsk: Nauka; 1985. 94 p. (in Russian)

[38] Asher GB. Development of computerized thermal conductivity measurement system utilizing the transient needle probe technique: An application to hydrates in porous media [PhD thesis]. Colorado: Colorado School of Mines, Golden; 1987. 179 p

[39] Huang D, Fan S. Measuring and modeling thermal conductivity of gas hydrate-bearing sand. Journal of Geophysical Research. 2005;**110**:B01311. DOI: 10.1029/2004JB003314

[40] Duchkov AD, Manakov AY, Kazantsev SA, Permyakov ME, Ogienko AG. Thermal conductivity measurement of the synthetic samples of bottom sediments containing methane hydrates. Izvestiya, Physics of the Solid Earth. 2009;**45**:661-669. DOI: 10.1134/S1069351309080060

[41] Yang L, Zhao J, Wang B, Liu W, Yang M, Song Y. Effective thermal conductivity of methane hydrate-bearing sediments: Experiments and correlations. Fuel. 2016;**179**:87-96. DOI: 10.1016/j.fuel.2016.03.075

[42] Wright JF, Nixon FM, Dallimore SR, Henninges J, Cote MM. Thermal conductivity of sediments within the gas-hydrate-bearing interval at the JAPEX/JNOC/GSC et al. In: Dallimore SR, Collett TS, editors. Mallik 5L-38 Gas Hydrate Production Research Well. Bulletin 585. Ottawa: Geological Survey of Canada; 2005. pp. 1-5

[43] Muraoka M, Ohtake M, Susuki N, Yamamoto Y, Suzuki K, Tsuji T. Thermal properties of methane hydrate-bearing sediments and surrounding mud recovered from Nankai trough wells. Journal of Geophysical Research - Solid Earth. 2014;**119**:8021-8033. DOI: 10.1002/2014JB011324

[44] Muraoka M, Susuki N, Yamaguchi H, Tsuji T, Yamamoto Y. Thermal properties of a supercooled synthetic sand−water−gas−methane hydrate sample. Energy & Fuels. 2015; **29**(3):1345-1351. DOI: 10.1021/ef502350n

[45] Chuvilin E, Bukhanov B. Effect of hydrate formation conditions on thermal conductivity of gas-saturated sediments. Energy & Fuels. 2017;**31**(5):5246-5254. DOI: 10.1021/acs.energyfuels.6b02726

[46] Kuhs WF, Klapproth A, Gotthardt F, Techmer K, Heinrichs T. The formation of meso- and macroporous gas hydrates. Geophysical Research Letters. 2000;**27**(18):2929-2932

[47] Staykova DK, Kuhs WF, Salamatin A, Hansen T. Formation of porous gas hydrates from ice powder: Diffraction experiments and multi-stage model. Journal of Physical Chemistry B. 2003;**107**:10299-10311

[48] Bukhanov BA, Chuvilin EM, Guryeva OM, Kotov PI. Experimental study of the thermal conductivity of the frozen sediments containing gas hydrate. In: Proceedings of the 9th International Conference on Permafrost (9-ICOP); 23 June-03 July 2008; Fairbanks; 2008. pp. 205-209

[49] Chuvilin EM, Kozlova EV. Experimental estimation of hydrate-containing sediments stability. In: Proceedings of the 5th International Conference on Gas Hydrate (ICGH-5); 12-16 June 2005; Trondheim; 2005. pp. 1540-1547

[50] Chuvilin EM, Guryggeva OM. Experimental study of self-preservation effect of gas hydrates in frozen sediments. In: Proceedings of the 9th International Conference on Permafrost (9-ICOP); 23 June-03 July 2008; Fairbanks; 2008. pp. 263-267

[51] Hachikubo A, Takeya S, Chuvilin E, Istomin V. Preservation phenomena of methane hydrate in pore spaces. Physical Chemistry Chemical Physics. 2011;**13**:17449-17452. DOI: 10.1039/c1cp22353d

[52] Takeya S, Fujihisa H, Gotoh Y, Istomin V, Chuvilin E, Sakagami H, Hachikubo A. Methane clathrate hydrates formed within hydrophilic and hydrophobic porous media: Kinetics of dissociation and distortion of host structure. Journal of Physical Chemistry C. 2013;**117**:7081-7085. DOI: 10.1021/jp312297h

[53] Ershov ED, Lebedenko YP, Chuvilin EM, Yakushev VS. Experimental investigations of microstructure of ice—Methane hydrate agglomerate. Engineering Geology. 1990;**3**: 38-44 (in Russian)

Thermal Conductivity Measurement of Vacuum Tight Dual-Edge Seal for the Thermal Performance Analysis of Triple Vacuum Glazing

Saim Memon

Additional information is available at the end of the chapter

http://dx.doi.org/10.5772/intechopen.74255

Abstract

A vacuum tight glass edge seal's thermal conductivity is one of the principal factor in determining the heat distribution towards the centre of pane, ultimately influences the thermal transmittance (U-value) of a triple vacuum glazing. So far indium and solder glass have proven to be vacuum tight edge sealing materials but both have certain limitations. In this chapter, a new low-temperature vacuum tight glass edge seal composite's thermal conductivity, Cerasolzer CS186 alloy and J-B Weld epoxy-steel resin, were measured and validated with the mild-steel and indium using transient plane source method with a sensor element of double spiral and resistance thermometer in a hot disk thermal constants analyser TPS2500s are reported. The thermal conductivity data of Cerasolzer CS186 alloy and J-B Weld epoxy steel resin were measured to be 46.49 and 7.47 $Wm^{-1} K^{-1}$, with the deviations (using analytical method) of ±4 and ±7% respectively. These values were utilised to predict the thermal transmittance value of triple vacuum glazing using 3D finite element model. The simulated results show the centre-of-glass and total U-value of 300×300 mm triple vacuum glazing to be 0.33 and 1.05 $Wm^{-2} K^{-1}$, respectively. The influence of such a wide edge seal on the temperature loss spreading from the edge to the central glazing area is analysed, in which the predictions show wider edge seal has affected the centre-of-glass U-value to 0.043 $Wm^{-2} K^{-1}$ due to the temperature gradient loss spread to 54 and 84 mm on the cold and warm side respectively.

Keywords: thermal conductivity, transient plane source, triple vacuum glazing, thermal performance, vacuum seal

1. Introduction

Carbon reduction and energy efficiency of domestic buildings have been one of the major global concerns due to limits with climate change [1]. Energy efficiency can be improved by high performance smart windows, high levels of wall insulation, efficient appliances and effectiveness of renewable energy results in saving financial cost to consumers and carbon dioxide emissions [2, 3]. One of the main functions of a smart triple vacuum glazed windows is to reduce heat flow between indoors and outdoors, i.e. to provide preeminent thermal insulation so called thermal transmittance (U-value) [4]. It depends on the number of glass panes, the space between glass panes, emissivity of the coatings on glass pane, frame in which the glass is installed, the type of spacers that separate the panes of glass and the type of window frame. The total U-value includes the effect of the frame and the glazing edge area. An influence of the glazing edge area is dependent on the width and the type of edge sealing material.

The hermetic edge seal of a triple vacuum glazing must be capable of maintaining vacuum pressure of less than 0.1 Pa in order to suppress gaseous conduction for long term duration [5]. Sealing of two glass panes edges using high power laser through quartz window in vacuum chamber was developed by Benson et al. [6]. This achieves hermetic seal but the level of vacuum was not less than 0.1 Pa, due to gases and vapour particles caused by lasering remain in the cavity [7]. High temperature edge sealing technique developed by the Collins group at the University of Sydney is based on material solder glass sealed at high temperature around 450°C [8–10]. This technique achieved significant centre of pane U value of 0.8 $Wm^{-2}\ K^{-1}$ and considered at commercial level. The problems with high temperature method of sealing is degradation of low emittance coatings only hard coatings can be used, if using toughened glass then loss of toughness, and require more amount of heat energy for fabrication due to heat require for several hours. Low temperature solder glass material was investigated to form a hermetic edge seal, but durability was a problem due to the absorption of moisture. Polymers have problems of gas permeability and out gassing [7]. Low temperature edge sealing technique developed at the University of Ulster is based on Indium alloy sealed at low temperature process about 160°C. It requires secondary adhesive seal to prevent access from moisture [11, 12]. A low temperature sealing process allows the use of low emittance soft coatings reduces radiative heat transfer between glass panes and toughened glass allows to increase support pillar spacing reduces conductive heat transfer. The problem with low temperature edge sealing material is indium alloy is high-priced and for long term cost effective vacuum glazing, this method is not encouraged at commercial level [13, 14].

A new low-temperature composite materials and methods of fabrication was reported in Memon et al. [15]. In which CS-186 type of Cerasolzer and steel reinforced epoxy by J-B resin were used for the development of triple vacuum glazing as shown in **Figure 1**. In this chapter, the experimental measurements of thermal conductivity of this composite material are reported. The significance of this study is to analyse the influence of edge area on the thermal transmittance of the composite edge seal for the fabrication of triple vacuum glazing. This value of the thermal conductivity was then used to develop model using finite element method to predict the influence of its wider edge seal and due to its thermal conductivity on the thermal performance.

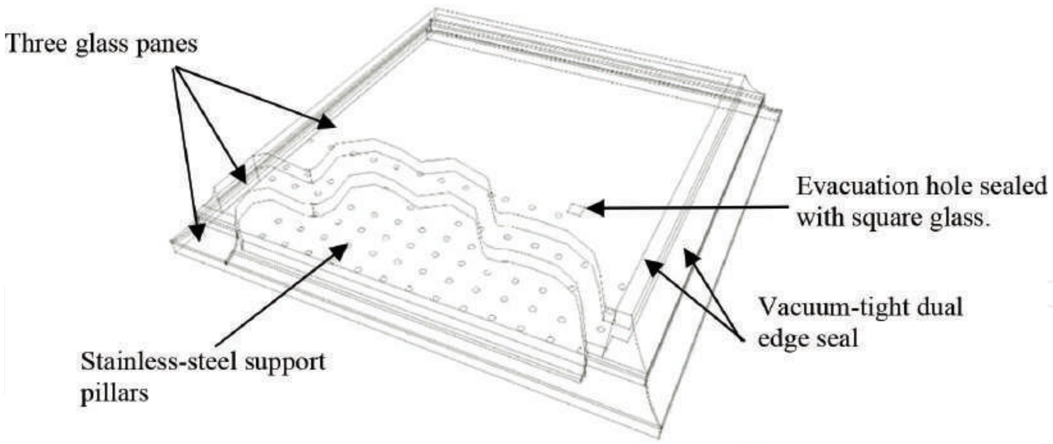

Figure 1. A schematic diagram of vacuum tight dual edge sealed triple vacuum glazing.

2. Methodology

A number of different instruments are available for the measurement of the thermal properties of materials [16]. There are two main methods, steady state method and transient. The steady state approach is further divided into one dimensional heat flow and radial heat flow techniques. One dimensional heat flow technique include the guarded hot plate method which is the ASTM standard based measurement system used for highly insulating materials. The radial heat flow technique includes cylindrical, spherical and ellipsoidal methods. There are a number of transient methods, which can be used for the measurement of thermal conductivity such as hot wire, transient hot strip and transient plane source methods. The experimental measurements of thermal conductivity performed in this study were undertaken using a Hot Disk thermal constants analyser TPS 2500 s. This system is based on the transient plane source (TPS) method. The TPS method consists of a sensor element in the shape of a double spiral which acts both as a heat source to increase the temperature of the sample and a resistance thermometer to record the time dependent temperature increase [17]. In the current experiments, a sensor of design 7577 was used which is made of a 10 μm thick Nickel-metal double spiral. The radius of the sensor was chosen to be 2.001 mm in order to reduce the size of the sample. It is advised [18] that the diameter of the sample should not be less than twice that of the sensor diameter and the thickness of the sample should not be less than the radius of the sensor. The sensor element is usually insulated with a material to provide electrical insulation. The material used is dependent on the operating temperatures. A thin polyamide (Kapton) insulating material was chosen for the sensor insulation which is suitable from cryogenic temperatures to about 500 K [19].

A sensor is placed between two flat cylindrical samples, as shown in **Figure 2**. Passage of a constant electric power through the spiral produces heat, increases the temperature and therefore the resistance of the spiral sensor as a function of time which can be expressed according to Gustavsson et al. [16] as,

$$R(t) = R_o\{1 + \varphi[\Delta T_i + \Delta T_{ave}(\tau)]\} \tag{1}$$

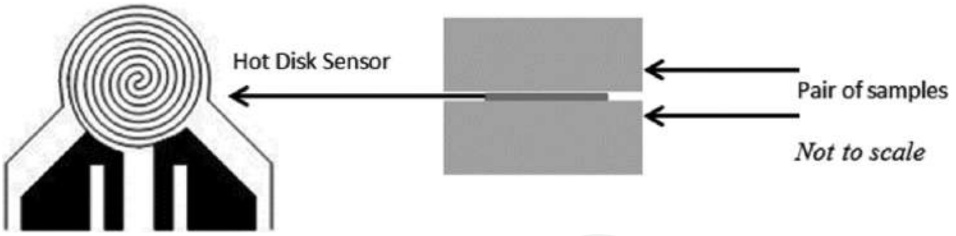

Figure 2. A schematic diagram of the pair of samples and the hot disk sensor placed in between two flat cylindrical samples.

where R_o is the resistance in ohms before the sensor is heated or at time t = 0 s, φ is the temperature coefficient of the resistivity (TCR) of the sensor 7577 i.e. 46.93 × 10^{-4} K^{-1}, ΔT_i is the initial temperature difference that develops momentarily over the thin insulating layers which cover the two sides of the sensor. The thermal conductivity of the sample can be expressed according to Bohac et al. [19] as,

$$k = \frac{P_o}{\pi^{\frac{3}{2}}.a.\Delta T_{ave}(\tau)}.D(\tau) \tag{2}$$

$$\tau = \sqrt{\frac{t}{t_c}} \tag{3}$$

$$t_c = \frac{a^2}{\alpha} \tag{4}$$

Where α is the thermal diffusivity of the sample in $mm^2\ s^{-1}$. From the experimentally recorded temperature increase over $D(\tau)$ a straight line can be plotted which intercepts ΔT_i, and slope of $\frac{P_o}{\pi^{\frac{3}{2}}.a.\Delta T_{ave}(\tau)}$ which allows the thermal conductivity to be determined. The final straight line from which the thermal conductivity measured is obtained through a process of iteration [17]. During a pre-set time, 200 resistance recordings are taken and from these a relation between temperature and time is established.

3. Results and discussions

3.1. Experimental measurements of the thermal conductivity of the hermetic edge seal

In order to validate the measurements of Cerasolzer allow and J-B Weld epoxy the results were compared with several measurements of the samples of Mild Steel (MSteel) and Indium in four repetitive experiments, combined the cut faces flatten to reduce the experimental errors. The experimental data are plotted in **Figure 3**. As can be seen this work is verified by the reported data of Mild steel and Indium. An increase of temperature with respect to reporting time interval have similar deviations and the highest increase of temperature was recorded for JB-Weld which gives a good agreement with the experimental data. The average temperature increase measured by the TPS sensor type 7577 of the mild steel, indium, J-B Weld epoxy steel resin and Cerasolzer CS186 samples are shown in **Figure 4**. It can be seen that the increase in temperature in the epoxy J-B Weld is greater than the mild steel. This is due to the fact that heat flow in semi-polymeric materials is low compared to metallic materials. The temperature increase in the sample made from Cerasolzer alloy was higher than the indium sample [20, 21].

An average thermal conductivity of a mild steel type SIS2343 sample was measured to be 13.76 $Wm^{-1} K^{-1}$. The reliability of the measured thermal conductivity is compared with the standard measurement value given in the standard data sheet i.e.13.62 $Wm^{-1} K^{-1}$. An average thermal conductivity of the indium sample was measured to be 77.84 $Wm^{-1} K^{-1}$ with a repeatability of four times. The thermal conductivity measurement for Cerasolzer alloy and J-B Weld epoxy steel resin, as detailed in **Table 1**, with the deviations were calculated to be ±4 and ±7% in the experimental measurements as compared with the analytical methods as detailed in the Section 2.

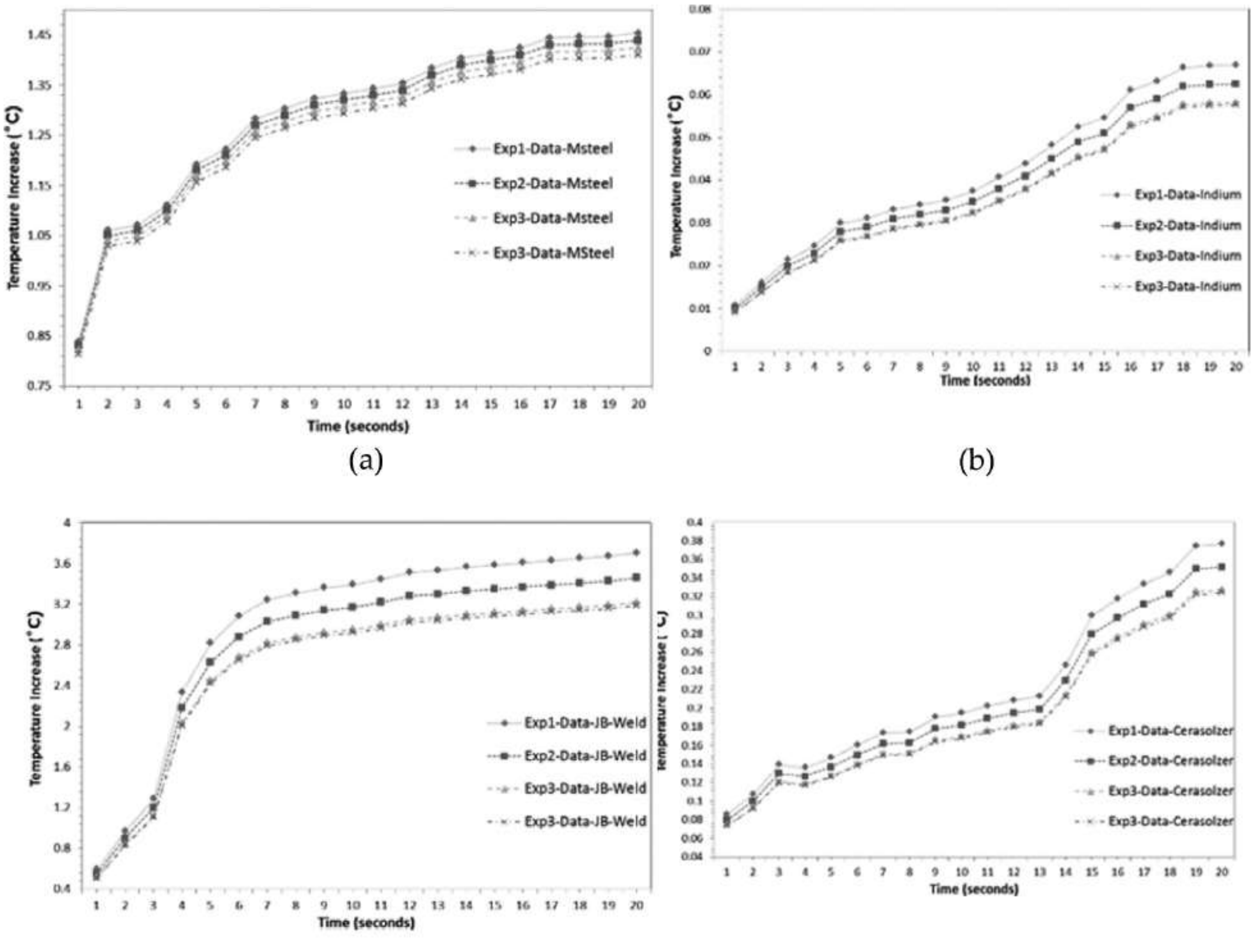

(a) (b)

(c) (d)

Figure 3. Experimental results as function of temperature increase for JB-weld and Cerasolzer in comparison to the verified mild steel and indium.

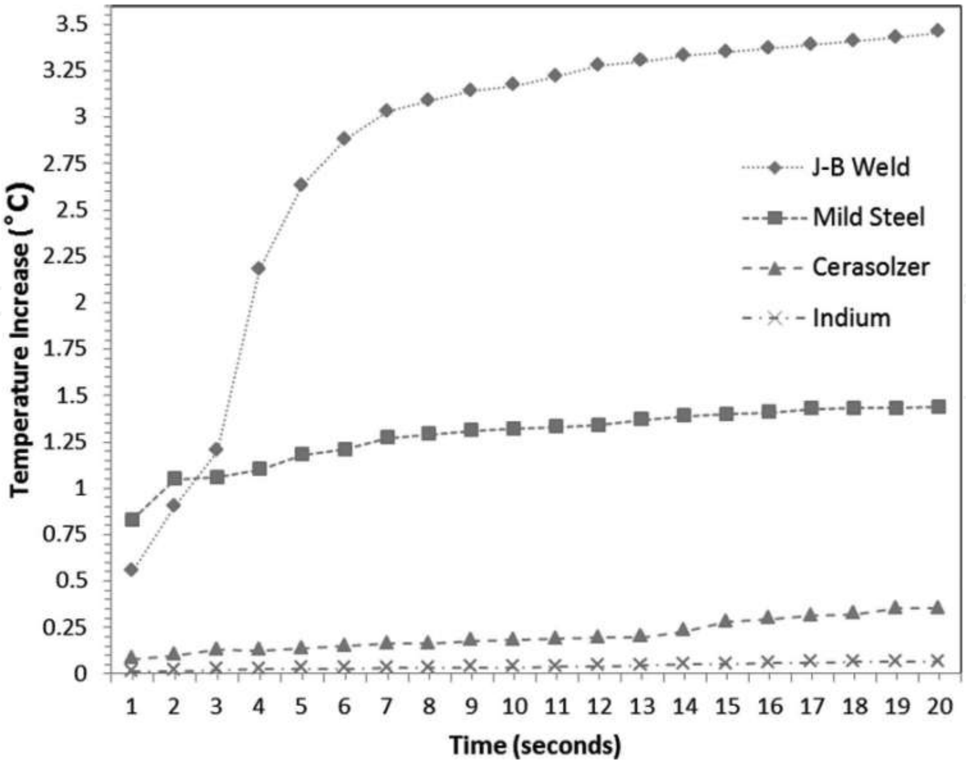

Figure 4. The average recorded temperature increase using the TPS sensor type 7577 for the samples made from mild steel, indium, J-B weld epoxy steel resin and Cerasolzer CS186.

Sample	Thermal conductivity at 21°C ($Wm^{-1}K^{-1}$) (Deviation)	Measuring time (second)	Power output from sensor (watts)
Mild Steel	13.76 (1%)	20	1
Indium	77.84 (7%)	20	1
Cerasolzer CS186	46.49 (±4%)	20	1
J-B Weld	7.47 (±7%)	20	1

Table 1. Measured thermal conductivities of Cerasolzer alloy CS186 and J-B weld epoxy steel resin and measurements of mild steel and indium.

3.2. Thermal performance analysis of hermetic edge sealed triple vacuum glazing

By utilising the measured thermal conductivities of Cerasolzer alloy as primary seal and JB-Weld as secondary seal, as detailed in **Table 1**, a 3D FE (finite element) model based on a commercial software package MSC Marc was employed to analyse the heat transfer and predict the thermal performance of the triple vacuum glazing. The symmetry of the model was exploited to simulate the heat transfer process in computationally efficient way; only one quarter (150 × 150 mm) of the triple vacuum glazing of dimensions 300 × 300 mm was modelled and simulated using ASTM boundary conditions [22]. Three k glass sheets having thermal conductivity of 1 $Wm^{-1}K^{-1}$ with SnO_2 coatings on inner surfaces with the emissivity of 0.15 were used. The support pillars were incorporated into the model explicitly [23]. This is based on the actual stainless steel pillar array having 16.2 $\mathrm{Wm^{-1}\,K^{-1}}$ of thermal conductivity. The number of support pillars was employed in the triple vacuum glazing that represented by the same number of pillars in the developed finite-element model. Since modelling the pillars with circular cross-section would lead to non-uniform mesh with distorted elements around the pillar, they were modelled using square cross-section (considered the diameter of 0.3 mm, height of 0.15 mm and pillar separation of 24 mm). Additionally, it is already established in the literature that the heat transfer through the pillar does not depend upon its shape but its cross-sectional area under certain boundary conditions [24, 25]. In order to keep the cross-sectional area similar to circular pillar with radius r, the side length of each square used is 1.78 r. The FE model implemented eight-node iso-parametric elements, with a total of 170,455 elements and 201,660 nodes to represent a quarter of the fabricated triple vacuum glazing. In FE model, the evacuated gap between glasses was represented with as a material with almost zero thermal conductivity to represent triple vacuum glazing. For sake of simplicity, the influence of residual gas among glasses was neglected in the model. In order to achieve realistic results from the simulation, a graded mesh with large number of elements was employed in the pillar. In addition to this, a convergence study was performed on the pillar to ensure the accuracy of the thermal performance predicted using the model. The material properties of the glass sheets applied to the models are those found in [22] and summarised in **Table 2**. The ASTM weather indoor/outdoor boundary conditions were employed in which the indoor and outdoor surface air temperatures were set to be at 21.1°C and −17.8°C respectively in winter conditions [23].

Type	Details	Value
TVG size	Top	284 by 284 by 4 mm
	Middle	292 by 292 by 4 mm
	Bottom	300 by 300 by 4 mm
Glass sheet	Thermal conductivity	1 $\mathrm{Wm^{-1}\,K^{-1}}$
Surface coating	Three low-e coatings	ε of 0.15 (SnO_2)
Glass sheet support-pillar	Thermal conductivity	16.2 $\mathrm{Wm^{-1}\,K^{-1}}$
	Material	Stainless steel 304
	Diameter	0.3 mm
	Height	0.15 mm
	Spacing	24 mm
Hermetic edge seal (Primary)	Measured thermal conductivity	46.49 $\mathrm{Wm^{-1}\,K^{-1}}$
	Material	Cerasolzer CS-186
	Width (wideness)	10 mm
Support seal (Secondary)	Measured thermal conductivity	7.47 $\mathrm{Wm^{-1}\,K^{-1}}$
	Epoxy steel resin	J-B Weld
	Width (wideness)	4 mm

Table 2. Parameters employed in FEM of the fabricated sample of triple vacuum glazing.

The internal and external surface heat transfer coefficients were set to 8.3 and 30 $Wm^{-2} K^{-1}$ respectively [26].

The finite element 3D modelling results show a centre of glass and overall U-value of 0.33 and 1.05 $Wm^{-2} K^{-1}$, respectively, this is compared to the predictions of [26] i.e. 0.2 $Wm^{-2} K^{-1}$ and [27] i.e. 0.26 $Wm^{-2} K^{-1}$ as follows.

The U value (centre of glass) 0.2 $Wm^{-2} K^{-1}$ [13] was based on the parametric model of triple vacuum glazing without frame focused on the central glazing area. This value was achieved with 6 mm (top), 4 mm (middle) and 6 mm (bottom) thick untampered soda lime glass sheets having four layers (1-top, 2-middle and 1-bottom) of low-e coatings (ε of 0.03). It is compared with the results of this paper, it is found that an increase of U value (centre-of-glass) 0.13 $Wm^{-2} K^{-1}$. Such deviation is due to the design of the fabricated sample reported in this paper which is made of 4 mm(top), 4 mm (middle) and 4 mm(bottom) untampered soda lime glass sheets having three layers of low-e SnO_2 coatings (ε = 0.15). The reason, to use such dimensions and SnO_2 coatings, is the conventional availability of glass sheets from Pilkington Glass and its use in the UK dwelling.

The influence of edge effects is well-detailed in Fang et al. [27, 28] and reported predicted the U values (centre-of-glass and overall) to be 0.26 and 0.65 $Wm^{-2} K^{-1}$, respectively. These values were reported for a TVG sample size of 500 × 500 mm with 4 mm (top), 4 mm(middle) and 4 mm (bottom) un-tempered soda lime glass sheets having four layers (1-top, 2-middle and 1-bottom) of low-e coatings (ε of 0.03) with a frame rebate depth of 10 mm and the width of indium-alloy edge seal 6 mm (k of 83.7 $Wm^{-1} K^{-1}$). It can be compared, considering all factors, with the results of this paper. It is found that an increase of 0.07 $Wm^{-2} K^{-1}$ (deviation of 26.9%) and 0.4 $Wm^{-2} K^{-1}$ (deviation of 61.54%) of centre of glass and overall U value, respectively. Such deviations, as per FEM calculations, are due to: the sample size influences to a small extent as the TVG fabricated sample size was of the size 300 × 300 mm, the width of the edge seal influences to a large extent because the TVG fabricated sample width of edge seal used was total 14 mm (10 mm wide Cerasolzer seal and 4 mm wide J-B Weld supportive seal), the use of three SnO_2 low-e coatings (ε of 0.15) in the fabricated sample instead of four Ag low-e coatings (ε of 0.03), and there is no frame rebate depth utilised in the fabricated sample of TVG that has an influence to a small extent on the overall U value of the TVG because the purpose of this paper is focused on the hermetic sealing materials thermal conductivities and triple vacuum glazing area thermal performance only. By accounting all these factors and including the thermal conductivity of the sealing materials, the FEM model predictions are in good agreement.

The simulated isotherms of the triple vacuum glazing for the outdoor and indoor surfaces are shown in **Figure 5**. The mean glass surface temperatures were simulated to be −12.55 and 6.71°C for the outdoor and indoor surfaces of the total glazing area. The mean surface temperatures for the centre of glass area were simulated to be 16.43 and −16.60°C for the outdoor and indoor surfaces respectively. It can be seen the temperature discrepancies on the outdoor side are smaller than the indoor side. This is, however, due to the use of 14 mm composite edge seal as compared to the edge seal thickness of 6 mm [28]. Thus, the edge effects need to be reduced by narrowing the width of edge-seal to 9 mm (6 mm and 3 mm for primary and secondary respectively) which reduces the centre-of-glass U-value of 0.043 $Wm^{-2} K^{-1}$.

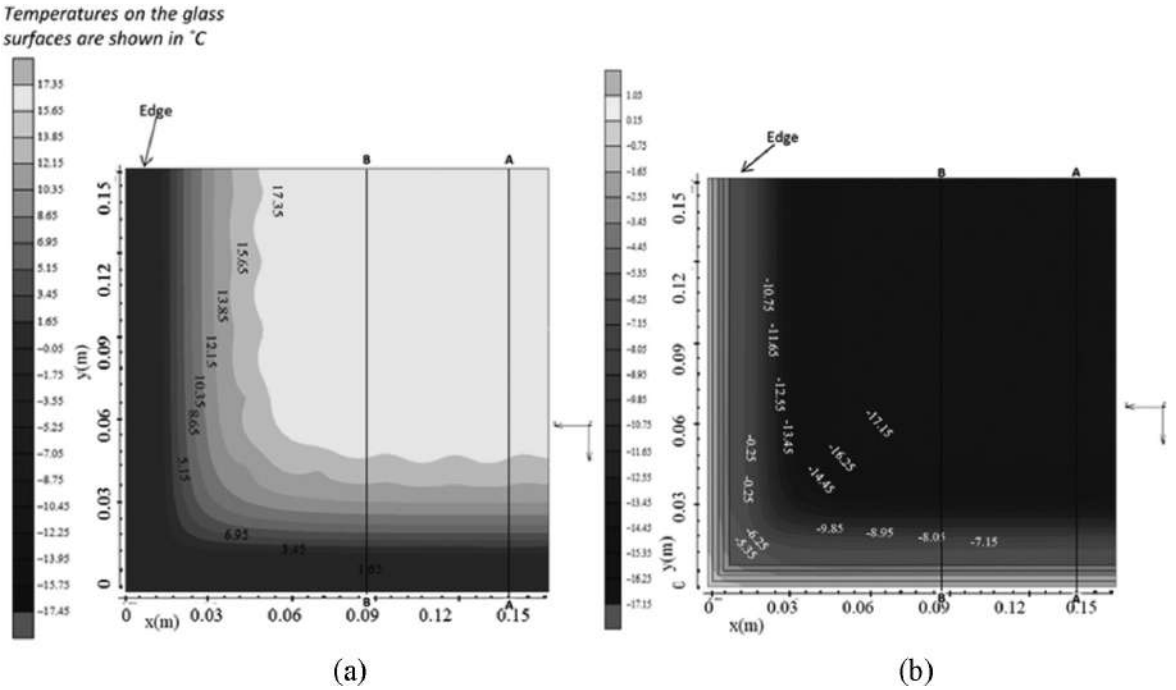

Figure 5. The FEM based isotherms on (a) the indoor (b) the outdoor glass surface showing the temperature variations from the edge area towards the central glazing area.

A finite element calculations of the temperature loss due to a wider edge seal are analysed, along the outer surface lines AA and BB (as shown in **Figure 5**), showing the temperature gradient from the glazing edge to the central area of the glazing as illustrated in **Figure 6**. An

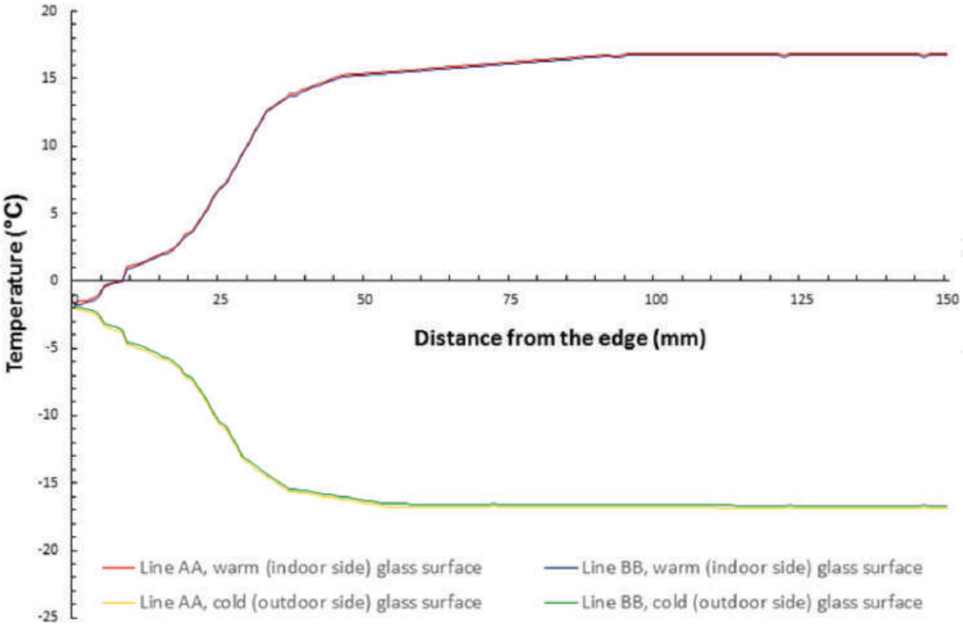

Figure 6. The temperature loss, due to a wider edge seal, along the glazing surface lines AA and BB showing the temperature gradient from the glazing edge to the central area of the glazing of the one quarter of total sample of 300 × 300 mm using ASTM boundary conditions.

influence of wider edge seal on temperature loss around the edge area has affected the centre-of-pane U value. **Figure 6** shows there are smaller temperature gradients on the cold surface as compared to the warm surface of the glazing which is due to the periodic shape of the edge sealing area of triple vacuum glazing as shown in **Figure 1(b)**. It can be seen the influence of temperature gradient loss spread to 54 and 84 mm on the cold and warm side respectively. When comparing with the temperature gradient profiles of [26, 27] the results are in good agreement with the results presented in this paper.

4. Conclusions

In this study, a hot disk thermal constants analyser TPS 2500s using transient plane source technique with a sensor element in the shape of double spiral and resistance thermometer is proved to be an adequate in measuring and analysing the thermal conductivity of hermetic edge sealing materials (i.e. Cersolzer CS186 and J-B Weld). The technique was validated by measuring the thermal conductivity for Mild Steel and Indium and comparing these results with those available in literature. This validated technique based on hot disk thermal constants analyser was then used to measure thermal conductivity of Cerasolzer CS186 alloy and J-B Weld epoxy steel resin and found to be 46.49 and 7.47 $Wm^{-1} K^{-1}$, respectively. It has been shown that an increase in temperature has direct relation with respect to reporting time with highest increase in temperature was recorded for JB-Weld for a given time period, which is in agreement with the experimental data. It has also been shown that the increase in temperature in the epoxy J-B Weld is greater than that of mild steel. This observation is linked to the fact that the heat flow in semi-polymeric materials is less as compared to that of metallic materials. The temperature increase in the sample made from Cerasolzer alloy was higher than that of indium sample. These values were utilised for the numerical prediction of thermal performance of triple vacuum glazing using 3D FE model. The simulated resulted showed that the centre-of-glass and total U-value of 300 × 300 mm triple vacuum glazing are 0.33 and 1.05 $Wm^{-2} K^{-1}$, respectively. The thermal transmittance values can be reduced by using soft low emittance coatings and by reducing the width of the hermetic edge seal to 9 mm. An influence of wider edge seal on temperature loss spreading from the edge to the central glazing area was further analysed with the FEM model calculations. In which it is concluded that the wider edge seal has affected the U-value to 0.043 $Wm^{-2} K^{-1}$ because of the temperature gradient loss spread to 54 and 84 mm on the cold and warm side respectively.

Acknowledgements

The author acknowledge the valuable advice and guidance received from Prof P. C. Eames during the course of this research work. This work was supported by the EPSRC funded project CALEBRE (Consumer Appealing Low energy Technologies for Building Retrofitting) [EP/G000387/1].

Nomenclature

a	overall radius of the sensor [m]
d	thickness of the glass sheet [mm]
D	dimensionless time dependent variable
k	thermal conductivity [Wm^{-1} K^{-1}]
P_o	total output power from the sensor [W]
R	resistance [ohms]
t	time [s]
ΔT_i	initial temperature difference [K]
$\Delta T_{ave}(\tau)$	average temperature increase of the sample surface on the other side of the sensor [K]
T	temperature [°C]
U	thermal transmittance [Wm^{-2} K^{-1}]

Abbreviations

ASTM	American Society for Testing and Materials
CALEBRE	consumer appealing low energy technologies for building retrofitting
CIBSE	chartered institution of building services engineers
FEM	finite element model
TPS	transient plane source
TVG	triple vacuum glazing

Subscripts

ave.	average
o	before the sensor is heated at
c	t = 0 s characteristic

Greek letters

ρ	density [kgm^{-3}]
α	thermal diffusivity of the sample [mm^2 s^{-1}]

τ	dimensionless time dependent function
φ	temperature coefficient of the resistivity [K^{-1}]
ϕ	heat loss [W]
ε	emittance

Author details

Saim Memon

Address all correspondence to: s.memon@lsbu.ac.uk

Centre for Advanced Materials, Division of Electrical and Electronic Engineering, School of Engineering, London South Bank University, London, UK

References

[1] Memon S, Eames PC. Heat load and solar gain prediction for solid wall dwellings retrofitted with triple vacuum glazing for selected window to wall area ratios, World Renewable Energy Forum, WREF 2012, Including World Renewable Energy Congress XII and Colorado Renewable Energy Society (CRES) Annual Conference, Colorado, USA. 6, 2012. pp. 4636-4643. ISBN: 9781622760923

[2] Memon S, Eames PC. Predicting the solar energy and space-heating energy performance for solid-wall detached house retrofitted with the composite edge-sealed triple vacuum glazing. Energy Procedia. 2017;**122**:565-570. DOI: 10.1016/j.egypro.2017.07.419

[3] Memon S. Analysing the potential of retrofitting ultra-low heat loss triple vacuum glazed windows to an existing UK solid wall dwelling. International Journal of Renewable Energy Development. 2014;**3**(3):161. DOI: 10.14710/ijred.3.3.161-174

[4] Memon S. Design, fabrication and performance analysis of vacuum glazing units fabricated with low and high temperature hermetic glass edge sealing materials. [PhD Thesis]. UK: Loughborough University Institutional Repository; 2013. DOI: https://dspace.lboro.ac.uk/2134/14562

[5] Fang F, Eames PC, Norton B, Hyde TJ. Experimental validation of a numerical model for heat transfer in vacuum glazing. Solar Energy. 2006;**80**:564-577. DOI: 10.1016/j.solener.2005.04.002

[6] Benson DK, Tracy CE. Evacuated window glazings for energy efficient buildings. Proceedings of SPIE 0562, Optical Materials Technology for Energy Efficiency and Solar Energy Conversion IV. San Diego, CA; 1985. p. 250

[7] Eames PC. Vacuum glazing: Current performance and future prospects. Vacuum. 2008; **82**:717-722. DOI: https://doi.org/10.1016/j.vacuum.2007.10.017

[8] Robinson SJ, Collins RE. Evacuated windows—theory and practice. ISES Solar World Congress, International Solar Energy Society, Kobe, Japan; 1989

[9] Collins RE, Simko TM. Current status of the science and technology of vacuum glazing. Solar Energy. 1998;**62**:189-213. DOI: 10.1016/S0038-092X(98)00007-3

[10] Collins RE, Tang JZ, Merrylands. Design improvements to vacuum glazing. 1999. US Patent No. 5891536

[11] Griffiths PW, Di Leo M, Cartwright P, Eames PC, Yianoulis P, Leftheriotis G, Norton B. Fabrication of evacuated glazing at low temperature. Solar Energy. 1998;**63**:243-249. DOI: 10.1016/S0038-092X(98)00019-X

[12] Zhao JF, Eames PC, Hyde TJ, Fang Y, Wang J. A modified pump-out technique used for fabrication of low temperature metal sealed vacuum glazing. Solar Energy. 2007;**81**:1072-1077. DOI: 10.1016/j.solener.2007.03.006

[13] Manz H, Brunner S, Wullschleger L. Triple vacuum glazing: Heat transfer and basic mechanical design constraints. Solar Energy. 2006 Dec 31;**80**(12):1632-1642. DOI: https://doi.org/10.1016/j.solener.2005.11.003

[14] Memon, S. Investigating energy saving performance interdependencies with retrofit triple vacuum glazing for use in UK dwelling with solid walls, Sustainable Development on Building and Environment: Proceedings of the 7th International Conference, Reading, UK; 2015. ISBN-13: 978–0993120701

[15] Memon S, Farukh F, Eames PC, Silberschmidt VV. A new low-temperature hermetic composite edge seal for the fabrication of triple vacuum glazing. Vacuum. 2015;**120**:73-82. DOI: 10.1016/j.vacuum.2015.06.024

[16] Gustavsson M, Karawacki E, Gustafsson SE. Thermal conductivity, thermal diffusivity, and specific heat of thin samples from transient measurements with hot disk sensors. Review of Scientific Instruments. 1994 Dec;**65**(12):3856-3859. DOI: https://doi.org/10.1063/1.1145178

[17] Gustafsson SE. Transient plane source techniques for thermal conductivity and thermal diffusivity measurements of solid materials. The Review of Scientific Instruments. 1991 Mar;**62**(3):797-804. DOI: 10.1063/1.1142087

[18] Hot Disk Thermal Constants Analyzer. 2013. TPS 2500s Instruction Manual, Mathis Instruments. [Accessed: 05–07-2013]

[19] Bohac V, Gustavsson MK, Kubicar L, Gustafsson SE. Parameter estimations for measurements of thermal transport properties with the hot disk thermal constants analyzer. The Review of Scientific Instruments. 2000 Jun;**71**(6):2452-2455. DOI: 10.1063/1.1150635

[20] Memon S, Eames PC. An investigation on edge sealing materials for the fabrication of vacuum glazing, 3rd School of Electrical, Electronic and Systems Engineering (EESE) Research conference, 2013 Mar 21–22, Loughborough University, UK

[21] Memon S. Experimental measurement of hermetic edge seal's thermal conductivity for the thermal transmittance prediction of triple vacuum glazing. Case Studies in Thermal Engineering. 2017;**10**:169-178. ISSN 2214-157X. DOI: 10.1016/j.csite.2017.06.002

[22] ASTM, Standard procedures for determining the steady state thermal transmittance of fenestration systems, ASTM Standard E 1423-91, in: 1994 Annual Book of ASTM Standard 04.07, American Society of Testing and Materials; 1991. pp. 1160-1165

[23] Memon S, Farukh F, Eames PC, Silberschmidt VV. A new low-temperature hermetic composite edge seal for the fabrication of triple vacuum glazing. Vacuum. 2015;**120**:73-82. DOI: 10.1016/j.vacuum.2015.06.024

[24] Collins RE, Robinson SJ. Evacuated glazing. Solar Energy. 1991 Jan;**47**(1):27-38. DOI: 10.1016/0038-092X(91)90060-A

[25] Wang J, Eames PC, Zhao JF, Hyde T, Fang Y. Stresses in vacuum glazing fabricated at low temperature. Solar Energy Materials & Solar Cells. 2007;**91**(4):290-303. DOI: 10.1016/j.solmat.2006.10.007

[26] Fang Y, Hyde T, Hewitt N, Eames PC, Norton B. Comparison of vacuum glazing thermal performance predicted using two-and three-dimensional models and their experimental validation. Solar Energy Materials & Solar Cells. 2009;**93**(9):1492-1498. DOI: https://doi.org/10.1016/j.solmat.2009.03.025

[27] Fang Y, Hyde TJ, Hewitt N. Predicted thermal performance of triple vacuum glazing. Solar Energy. 2010;**84**(12):2132-2139. DOI: 10.1016/j.solener.2010.09.002

[28] Fang Y, Hyde TJ, Arya F, Hewitt N, Wang R, Dai Y. Enhancing the thermal performance of triple vacuum glazing with low-emittance coatings. Energy and Buildings. 2015;**97**:186-195. DOI: 10.1016/j.enbuild.2015.04.006

Structural and Thermoelectric Properties Characterization of Individual Single-Crystalline Nanowire

Dedi, Indah Primadona, Ping-Chung Lee,
Chi-Hua Chien and Yang-Yuan Chen

Additional information is available at the end of the chapter

http://dx.doi.org/10.5772/intechopen.76635

Abstract

Herein, we report a method for structural characterization as well as TE properties measurements of individual single-crystalline Lead telluride (PbTe) NWs by employing a new microchip design. In this work, the single PbTe NW was characterized in four different types of measurement: structural characterization, Seebeck coefficient *S*, electrical conductivity σ, and thermal conductivity κ. The structural characterization by transmission electron microscope (TEM) revealed that the PbTe NWs were high-quality single crystals with a growth along the [100] direction. The TE properties *S*, σ, and κ measurement results of individual 75 nm PbTe NW at room temperature were −54.76 μV K^{-1}, 1526.19 S m^{-1}, and 0.96 W m^{-1} K^{-1}, respectively. Refer to the result of *S*, σ and κ; the figure of merit *ZT* values of a 75 nm PbTe NW at the temperature range of 300–350 K were 1.4–4.3 x 10^{-3}. Furthermore, it was observed that the κ value is size-dependent compared to previous reported, which indicates that thermal transport through the individual PbTe NWs is limited by boundary scattering of both electrons and phonons. The results show that this new technique measurement provided a reliable *ZT* value of individual NW yielded high accuracy for size-dependent studies.

Keywords: lead telluride, nanowires, thermal conductivity, size-dependent, figure of merit

1. Introduction

Recently, nano-engineered thermoelectric (TE) materials used for converting waste heat into electricity have become an interesting research topic. TE energy converters are devices that can harvest renewable energy for power generation and thermal sensing application [1–3]. The efficiency of TE materials is evaluated based on the dimensionless figure of merit ZT, which is written as $S^2\sigma T/(\kappa_e + \kappa_l)$, where S, σ, κ_e, and κ_l denotes the thermal power or Seebeck coefficient, the electrical conductivity, the electronic thermal conductivity, and the lattice thermal conductivity, respectively. The quantity of $S^2\sigma$ is defined as the power factor (PF). Theoretically, a reduction in dimensionality from three dimensions to one dimension yields a dramatically increased electronic density of states (DOS) at the energy band edges and a decreased thermal conductivity. As a result, the thermoelectric PF and assuredly ZT value enhances [4, 5]. Numerous studies have reported that the enhancement of ZT value in nanomaterials is the result of quantum confinement effects and increased surface phonon scattering [3, 6, 7].

Due to the nanometer scale effect, it is believed that in NWs comprising TE materials, such as PbTe, the value of S is higher than its bulk counterpart [8, 9]. According to the certain carrier-scattering assumptions, the enhancement of S value occurs because of the sharp increase in the local DOS around the Fermi level, which also can be interpreted as an increased local DOS effective mass (m_d^*). However, with the overall benefit of such an improvement in S, nanosize will cause a declining in carrier mobility (μ) and thus affect to the decreasing the ZT value. This is occurs because the increased local DOS usually leads to a heavier transport-effective mass of carriers. In the most well-known high-temperature TE, the carriers are predominantly scattered by phonons. [10] Increasing the S is an obvious goal for obtaining a high efficiency TE materials. Nevertheless, other changes in transport properties often sacrifice the σ correlated with an increase in the S and thus do not ultimately lead to an improvement in ZT.

In order to unveil the size effect on the intrinsic physical properties of TE materials, the measurement of nanowire without interference from either the matrix or external contacts is imperative. Furthermore, the TE properties measurement as well as structural characterization on single nanowire is also crucial in terms of the accuracy and reliability of the resulting ZT value. The low accuracy may occur because every single nanowire, although in the same batch synthesis process, may have a different structure or TE properties. However, measuring all properties on single nanowire is still challenging due to the unavailability of NW microchip which is compatible for all type measurements.

In this chapter, the synthesis and structural characterization of PbTe NWs as well as the preparation of newly design NW's microchip to resolve the above mentioned problem will be described in the first section. For synthesizing the NW, an alternative free-catalyst technique, the stress-induced growth method will be introduced. In the second section, we will discuss about their TE properties (S, σ, and κ).

Type of TE NW used in this chapter was single-crystalline PbTe NW. PbTe is a semiconductor with an energy band gap of 0.31 eV at 300 K [11–14]. In recent years, it has been found that PbTe is one of the superior TE materials in the temperature range of 400–900 K. This material has a large Seebeck coefficient, a very low κ_l (2.2 W m^{-1} K^{-1} at 300 K) [15] and a good electrical conductivity when appropriately chemical doped [16]. The synthesis of low-dimensional PbTe NWs has been intensively explored in the past decades [17–27]. Besides that, there have also been some studies on the TE properties of PbTe-based nanostructures such as PbTe/PbSeTe quantum dot superlattice [28] and PbTe NWs [20] with room temperature *ZT* value 0.75 and 0.0054, respectively.

2. Synthesis and structural characterization of PbTe NWs

2.1. Synthesis of PbTe NWs

In this work, the synthesis of single-crystalline PbTe NWs via a stress-induced method is described elsewhere [27], in a way similar to the on-film formation (ON–OFF) growth of other semiconductor NWs. [29] Briefly, the PbTe was made by mixing elemental Pb (Alfa Aesar, −200 mesh, 99.9%) and Te (Alfa Aesar, −325 mesh, 99.999%) inside a carbon-coated silica tube. After that, the resulting mixtures inside the tube was vacuumed up to 10^{-6} Torr, sealed, and slowly heated to 1000°C over a period of 12 hours. On the top of the heating process, the temperature was held for 4 hours, and then cooled down to room temperature. The resulted ingot was then cut by a diamond saw into a disc shape with a diameter of 10 mm. Before fabricating the PbTe films, the disc target and substrates were both ultrasonically cleaned in acetone, isopropanol, and then rinsed with deionized water. The PbTe films were prepared by depositing the synthesized PbTe ingot on single-crystal SiO_2/Si (100) substrates in a pulsed laser deposition (PLD) system (LPX Pro 210). The base pressure of the vacuum system was 5.0×10^{-7} Torr. The excimer laser was applied for 15 min at room temperature with energy and frequency of 140 mJ and 10 Hz, respectively. The substrate rotation speed was approximately 10 rpm. With the all mentioned set up, the total thickness of the PbTe films was about 20 nm. To synthesis PbTe NWs, the PbTe films were sealed in a vacuumed quartz tube below 5×10^{-6} Torr, annealed at 450°C for 5 days, and then cooled slowly to room temperature. During the annealing process, the NWs grew from the film to release the compressive stress caused by the difference in thermal expansion coefficients between the PbTe film (19.8×10^{-6}/°C) and the SiO_2/Si substrate (0.5×10^{-6}/°C)/(2.4×10^{-6}/°C).

2.2. Microchip preparation

As mentioned above, the challenge in working with TE NW was the measurement of thermoelectric properties as well as structural analysis on specific single-crystalline nanowire, to get a high accuracy of *ZT* value. Here, in order to solve that problem, a novel design of microchip was discussed. The preparation processes of the measurement platform are shown in **Figure 1**. First, the silicon (Si) wafer with Si_3N_4 layer (**Figure 1a**) on both sides was covered with the photoresist by using spin coating method (**Figure 1b**), followed by standard photolithography processes. After that the exposure soluble photoresist can be developed by the developer. The Si wafer was then put into the reactive ion etching system (RIE, Model: ANELA DEM-451T) for dry etching. The unprotected Si_3N_4 will be etched by the reactive ion. Then, the wafer is immersed into potassium hydroxide (KOH) solution for wet etching. The silicon which is exposed to KOH will be etched and leaving a thin Si_3N_4 membrane for further processes.

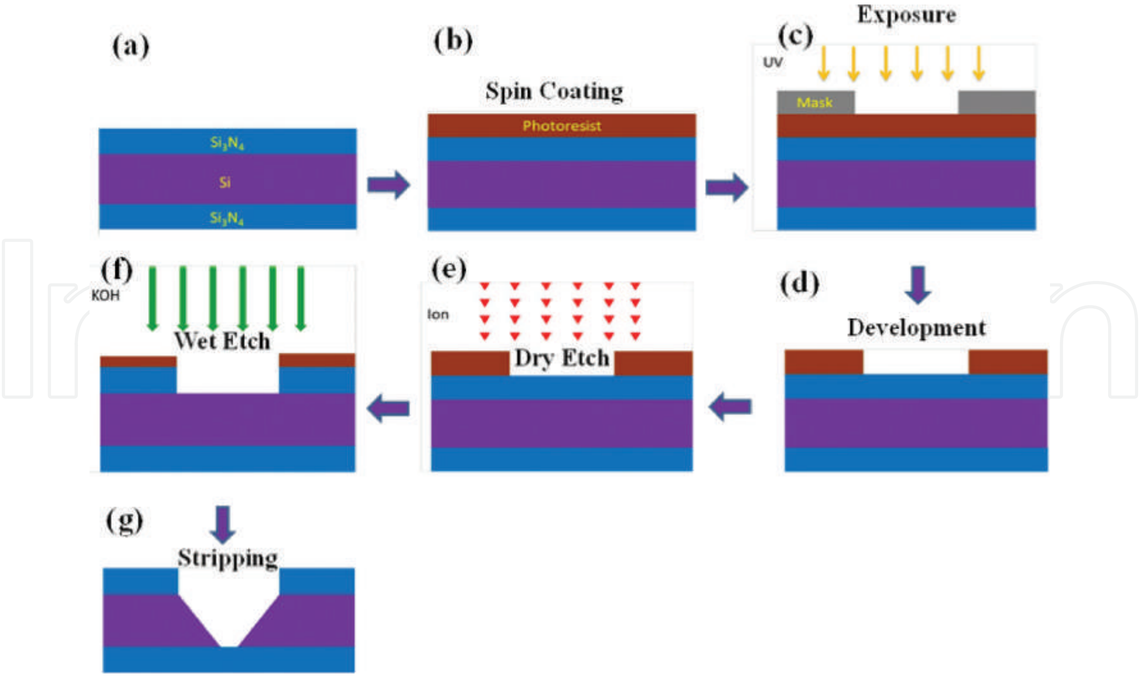

Figure 1. Schematic Si_3N_4 membrane template preparation: (a) the silicon wafer with Si_3N_4 on the both sides, (b) substrate is spin coated with photoresist, (c) Photoresist is exposed to a rectangular pattern with ultraviolet light, (d) soluble photoresist can be developed by the developer, (e) removing Si_3N_4 layer by reactive ion etching system (RIE), (f) dip the wafer into a bath of KOH for wet etching to create a cavity and leave a suspended Si_3N_4 membrane, and (g) strip the photoresist.

The standard photolithography processes were used to define the contact pads of the measurement platform. As shown in **Figure 2**, first, Si wafer with Si_3N_4 membrane is covered with photoresist material by spin coating, followed by exposure, evaporation, and lift-off process. The developed primary measurement platform is then ready to be used.

The flow chart of the suspending process of a nanowire on the measurement platform (microchip) was shown in **Figure 3**. Resistance temperature detectors (RTDs) and current leads were fabricated on the primary measurement platform by electron beam lithography [E-Beam Writer System, Model: Elionix ELS-7000 (100 keV)]. The Si_3N_4 membrane was removed by inductively coupled plasma etching system (ICP, Model: Elionix EIS-700) to open the window. After that, the single nanowire from the PbTe thin film was picked up by a tungsten needle (dw = 100 nm) under a binocular optical microscope and placed across on two RTDs of a Si_3N_4 microchip, where both ends of the nanowire attached to the current leads. In order to improve thermal and electrical contacts between the nanowire and the contact pads, the contacts of the nanowire on thermometers and current leads were covered with a thin layer of Platinum (Pt) using a focused ion beam (FIB) [DBFIB-SEM, FEI NOVA-600].

To examine how good the prepared contact, the contact resistance of all four points (point 1, 2, 3, and 4) as depicted in **Figure 4** were measured. First, the known direct current (DC) was applied between contacts 1 and 4 (4 probes) and then the voltage drop across contact 2 and 3 (2 probes, see **Figure 4**) was measured. The total resistance of two-point probe configuration is expressed as $R_{2point} = R_{lead} + 2R_{contact} + R_{nw}$. Wherein, R_{2point}, R_{lead}, $R_{contact}$, and

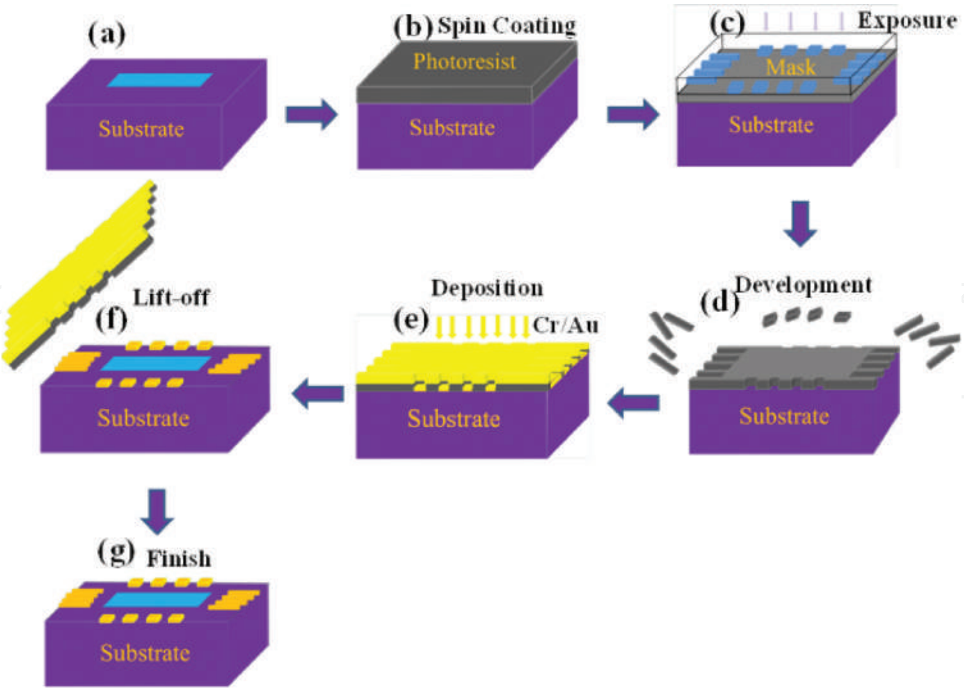

Figure 2. Schematic of depositing outer electrodes of the template: (a) silicon wafer with Si_3N_4 membrane, (b) substrate is spin coated with photoresist, (c) photoresist can be exposed to a pattern by ultraviolet light, (d) soluble photoresist will be developed by the developer, (e) the Cr/Au electrodes are deposited by thermal evaporator, (f) lift-off the photoresist by acetone, and (g) measurement platform is ready to be used.

R_{nw} represents resistance between point 2 and 3, resistance of Cr/Au electrodes, resistance of contacted NW to electrode, and NW resistance, respectively. The resistance of R_{2point} and R_{nw} were measured by two and four-point probes. Whilst, in order to obtain the contact resistance as $R_{cont} = (R_{2point} - R_{nw})/2$, R_{lead} (~10 Ω) was neglected. The measurement result of R_{2point} was about 6–7% from R_{nw} value. Since the power dissipation at the contacts is much smaller than the minimum power for 3ω signal, the resultant contact resistance supposedly does not affect the third harmonic signal. Furthermore, the contact metal pads act as large thermal reservoirs where the temperature is kept constant at the initial temperature during the experiment.

In addition, the prepared nanowire exhibited a linear current–voltage (I-V) curve wherein indicated the Ohmic contact response; the current range within 0 to 100 μA indicating the resistivity of NW follows the Ohm's law. An Ohmic contact is an electrical junction between two conductors which has a linear current–voltage (I-V) curve following the Ohm's law. Low resistance Ohmic contacts are applied to facilitate the flow of charge in both directions between the two conductors, without blocking from the excess power dissipation due to voltage thresholds. The contact quality has a contribution to both an electrical and a thermal effect, such as, if the electrical contact resistance is too high, the third harmonics measurement will be influenced by the heat dissipation occurred at the contacts due to Joule heating. Furthermore, incorrect selection of a working frequency will develop an error experiment results. Therefore, the AC impedance measurements with no electrical artifacts involved were utilized to choose a correct working frequency.

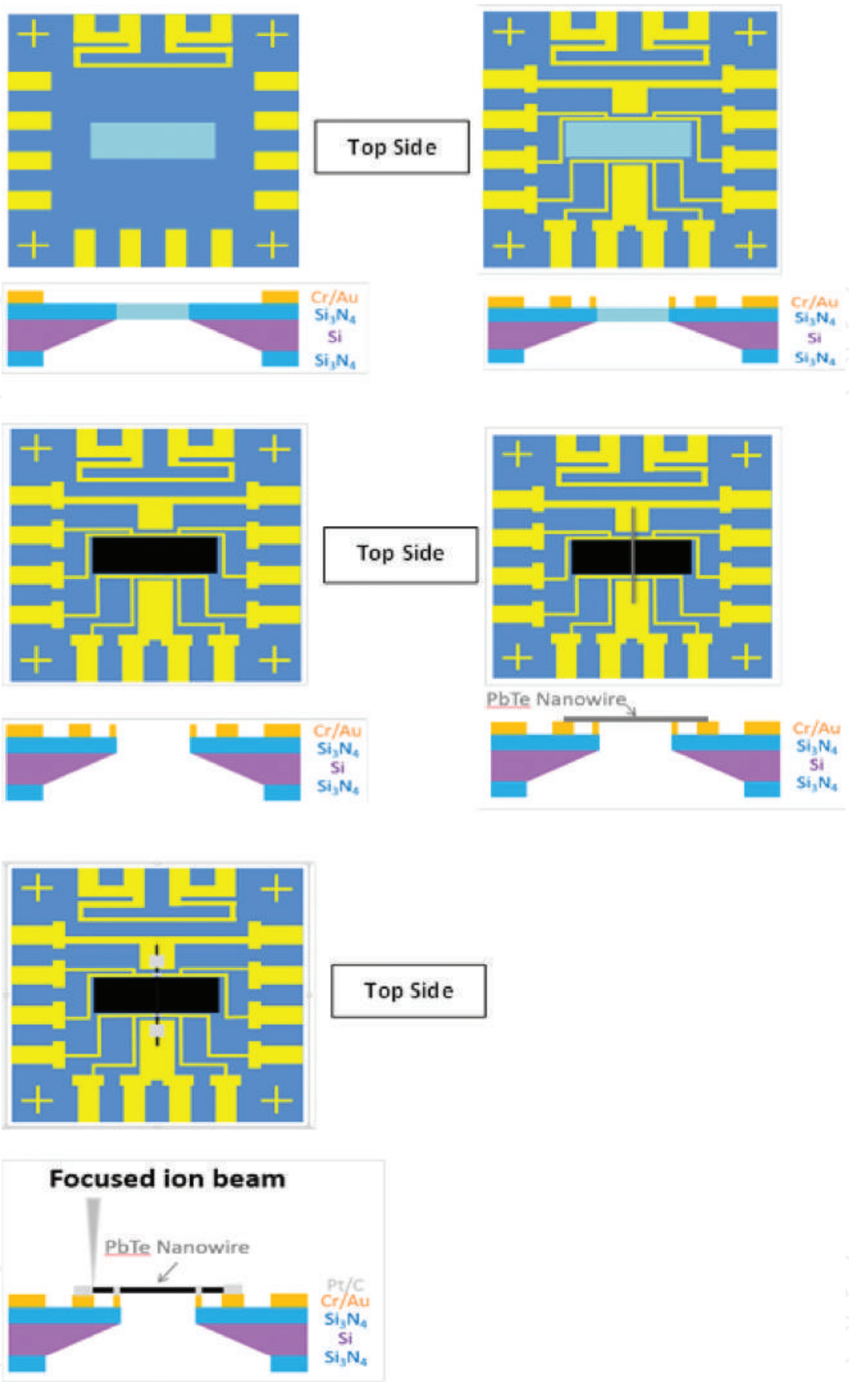

Figure 3. Flow charts of the suspending process of a nanowire on the measurement platform.

2.3. Structural characterization of PbTe NWs

The size and crystalline structure of PbTe NWs were characterized by scanning electron microscope (SEM) and transmission electron microscope (TEM). The SEM image of grew PbTe NWs on the substrate (**Figure 5a**) reveals that the length and the diameter of NWs were ranging from 5 to 70 μm and 50 to 300 nm, respectively. The NWs with length about 70 μm was picked up, placed, and contacted on the microchip as shown in **Figure 5b**. The prepared contacts have a

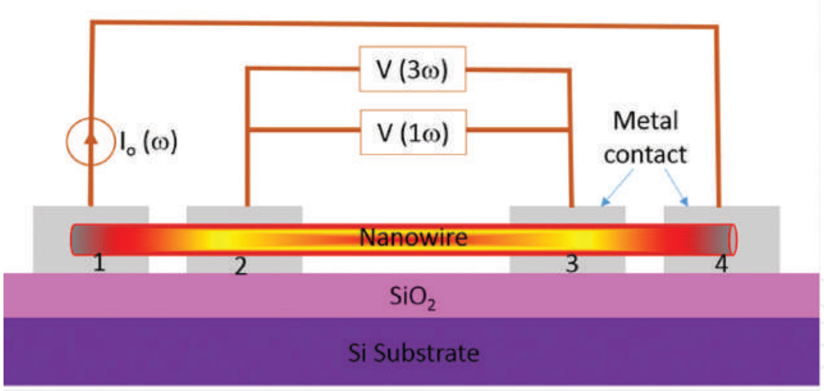

Figure 4. A schematic setup of four-point probe for measurement of electrical resistance (R), Seebeck coefficient (S) and the thermal conductivity (κ) by 3ω method.

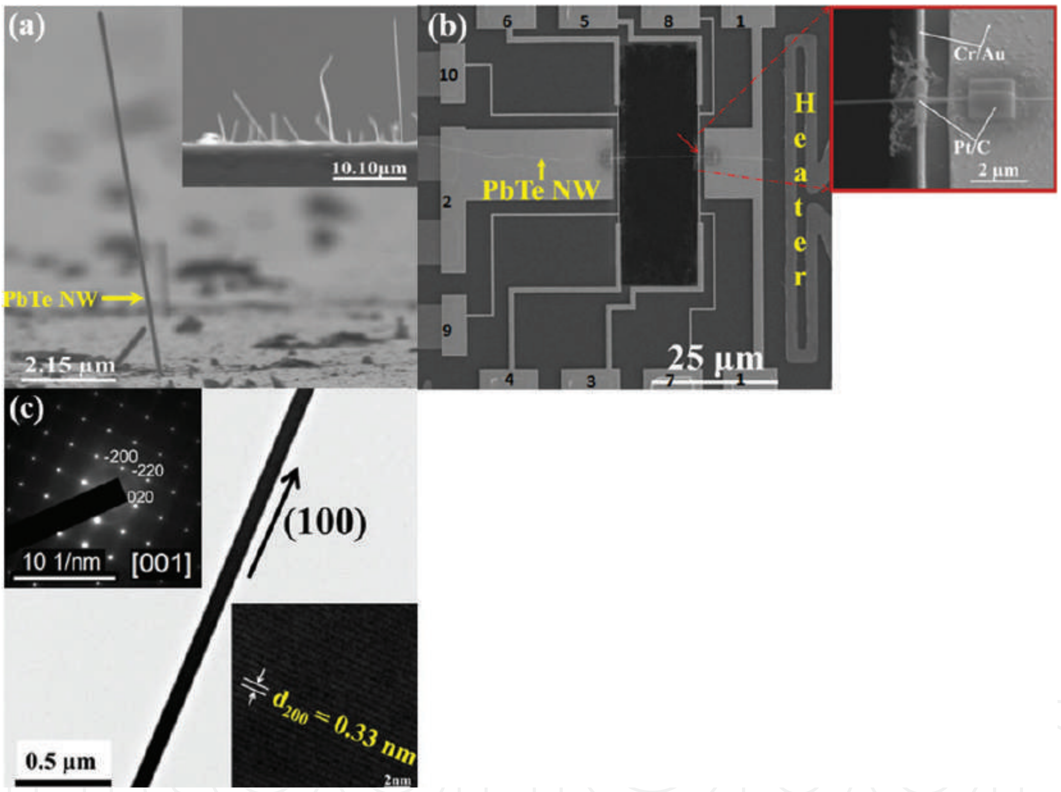

Figure 5. (a) SEM image of PbTe NWs grew on the surface of the PbTe thin film, (b) SEM images of a PbTe NW suspended on a Si_3N_4 template, inset: the Pt/C thermal contact between the PbTe NW and 10-nm Cr/50-nm Au electrodes on a Si_3N_4 microchip, (c) low-magnification TEM images of a PbTe NW, inset of the top left of figure: the SAED pattern (at the [001] zone axis), inset of the bottom right of figure: a high-resolution TEM image of a PbTe NW.

resistance about 425–430 Ω, wherein showed nearly Ohmic contacts. The microchip consisting of PbTe NW displayed in **Figure 5b** was used for complete structural analysis and TE properties measurements. The representative TEM image showed that the employed PbTe NWs has a diameter of 75 nm (**Figure 5c**) and this size was further convinced by the scanning transmission electron microscope (STEM) result (**Figure 6a**). In addition, the TEM image and a corresponding selected-area electron diffraction (SAED) pattern (inset of the top left of **Figure 5c**) revealed

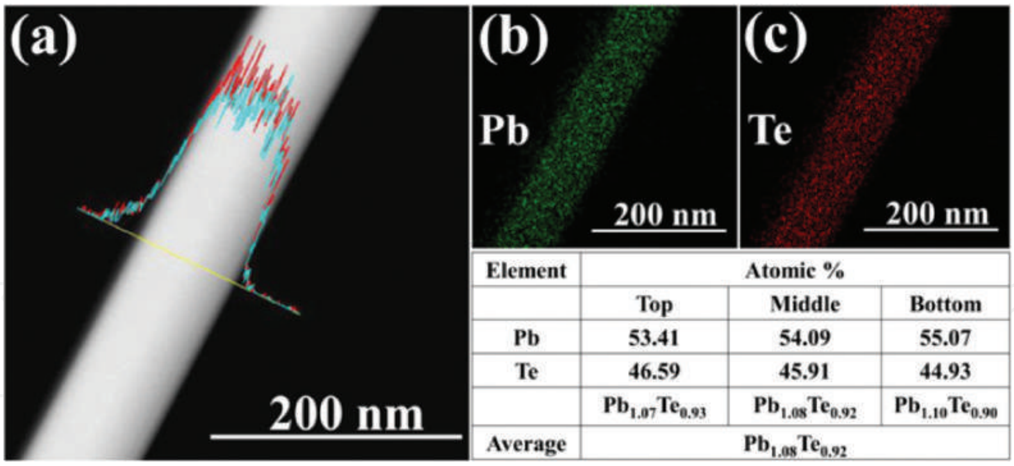

Element	Atomic %		
	Top	Middle	Bottom
Pb	53.41	54.09	55.07
Te	46.59	45.91	44.93
	$Pb_{1.07}Te_{0.93}$	$Pb_{1.08}Te_{0.92}$	$Pb_{1.10}Te_{0.90}$
Average	$Pb_{1.08}Te_{0.92}$		

Figure 6. (a) STEM images of a PbTe NW. The line profiles show that the Pb (blue line) and Te (red line) are homogeneously distributed throughout the NW, (b) and (c) elemental mapping showing the uniform distribution of Pb and Te along the NW, respectively.

that the PbTe NWs were high-quality single crystals with a growth along the [100] direction. While, the lattice fringes of the smooth PbTe were separated by 0.33 nm (inset of the bottom right of **Figure 5c**). This is consistent with a periodicity along the [200] direction with lattice constants of approximately 6.549 Å, which are approximately 1.2% higher than the bulk counterpart (a = 6.47 Å).

The chemical composition of the PbTe NWs was studied by using energy dispersive X-ray spectroscopy (EDS). The EDS line scan profile, shown in **Figure 6a**, revealed the uniform spatial distribution of the Pb and Te elements throughout the NW. This was further confirmed by using a STEM to map elements across the NW [**Figure 6b** and **c**]. The EDS point scanning experiments of the NWs quantitatively confirmed that Pb and Te are present in an average atomic ratio of 54.19 and 45.81% (Table in **Figure 6**), respectively. In addition, the EDS data also revealed that the atomic ratio of Pb/Te ≈ 1.18, with no impurities. As a result, the stoichiometric composition of the individual NW was $Pb_{1.08}Te_{0.92}$.

3. Thermoelectric properties

As mentioned before that the microchip with a rectangular window which shown in **Figure 5b** was employed to measure the TE properties of NW, i.e. electrical resistivity (ρ) and Seebeck coefficient (S). In this experiment, the PbTe NW was placed across two resistance thermometers, hot side thermometer Th (a gold wire parallel line to the heater between contact electrodes 7 and 8 which is marked as red arrows in **Figure 5b**) and cold side thermometer Tc (a gold wire between the contact electrode 9 and 10, **Figure 5b**) with both ends of the NW attach to the current leads (electrode 1 and 2, **Figure 5b**). To measure the V1ω and V3ω signal, electrodes 3 and 4 (voltage leads) were connected to lock-in amplifier. The thermal conduction

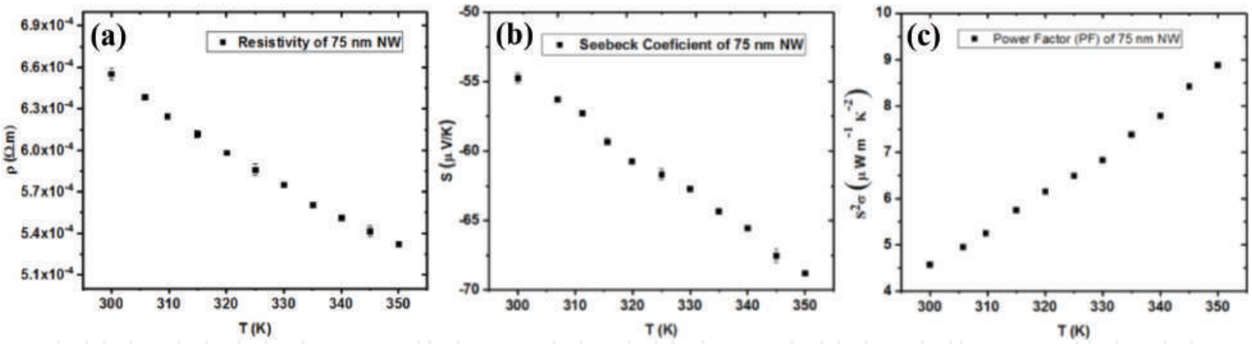

Figure 7. Temperature dependence of (a) electrical resistivity, (b) Seebeck coefficient, and (c) power factor of a 75 nm PbTe NW.

from NW to the microchip substrate that affects the S and ρ measurement was assured zero. Furthermore, in order to eliminate convectional heat loss, all measurements were carried out in a high vacuum of at least lower than 2×10^{-6} Torr.

Four-point probe method was applied for ρ measurement. In this work, an AC current flowed to the NW via electrode 1. The voltage (V) and current (I) difference between electrode 1 and 2 was measured through the voltage leads. A pair of current leads into the NW to determine the root mean square of the voltage difference of a pair of voltage leads. By substituting the obtained V and I value to the $V = I\bullet R$ formula, the resistance (R) value is obtained. We get the R of NW, the ρ value could be attained by applying the formula of $\rho = R\bullet A / L$ where A and L are cross-section area of the wire and length between a pair of voltage leads, respectively. **Figure 7a** showed the measurement results of NW resistivity ρ at temperatures range 300–350 K. This figure demonstrated that the resistivity ρ of a 75-nm PbTe NW was temperature dependence which indicated a semiconducting behavior. The resistivity of a PbTe NW at near room temperature was 6.55×10^{-4} Ω m, which 43 times greater than the bulk counterpart (1.52×10^{-5} Ω m) [14]. This is probably due to the surface scattering of charge carriers [30].

For the Seebeck effect measurement, the characterization was based on the voltage and temperature difference generated between electrodes 3 and 4 (**Figure 5b**). To generate the temperature gradient between those two electrodes, the heater with frequency 1ω and magnitude equals to $I\bullet Sin(\omega t)$ was applied at one end of the NW. In this experiment, the sample was employed as the sensor of the thermometer as well, thus, temperature coefficient of electrical resistance of them are needed to be calibrated at first. By applying a DC current to the sensor and measuring the change of the voltage difference at frequency 2ω between the two ends of the sensor, the resistance change of the sensor would be known. After obtaining the temperature coefficient of electrical resistance, the temperature gradient created between two ends of the NW would be gained, because the observed heat is proportional to the square of the current multiplied by the electrical resistance of the NW, $Q \propto I^2\bullet\sin^2(\omega t)\bullet R$, where Q and R denote the observed heat and the electrical resistance of the NW, respectively. Mathematically, $\sin^2\alpha = [(1\text{-}\cos2\alpha)/2]$, it means that the frequency of 2ω was applied to heat the heater. As the heater is heated at frequency 2ω, the sample temperature and sensor resistance would fluctuated at frequency 2ω as well. By knowing the temperature gradient and also measuring the thermoelectric voltage of two ends of the sample, S can be calculated by implementing the formula: S = (△V) / (△T).

The experiment results of Seebeck effect of a 75-nm PbTe NW shown in **Figure 7b** revealed that the S value was temperature dependence. The S value increased with increasing the temperature. In addition, as depicted in **Figure 7b** that the S of PbTe NWs at various temperature measurements has a negative sign which indicated for n-type semiconductor material. Those negative sign appears because their electrons have a much higher μ than holes and dominate the electronic transport properties [31, 32]. At temperature of 300 K, the S value for the 75-nm NW was −54.76 μV K^{-1}, which is about 69% lower compare to the bulk counterpart [14]. This result may due to the consequences of structural imperfections, such as antisite defects inside PbTe NW (i.e., the creation of one vacancy at the tellurium site) [14, 33].

Theoretically, for almost all materials, the trend of ρ was closely correlated with the S. It was consistent with our experimental resultts (**Figure 7a** and **b**) which showed that the smaller ρ had a higher S value. Conversely, due to s = 1/ρ, thus s value increases when S is increased. The PF ($S^2σ$) calculation results of PbTe NWs as a function of temperature are plotted in **Figure 7c**. The PF increased gradually when the temperature increased, and this result was mainly due to the influence of ρ trends. At the temperature about 300 K the $S^2σ$ values were 4.58 μW m^{-1} K^{-2}.

Comparing the S value as a function of carrier density of various PbTe bulk obtained by Harman et al., **Figure 8** show that the S was closely correlated with the carrier concentration (n), Our results was consistent with the other previous experiments [14, 34] in which a smaller n had a higher S value.

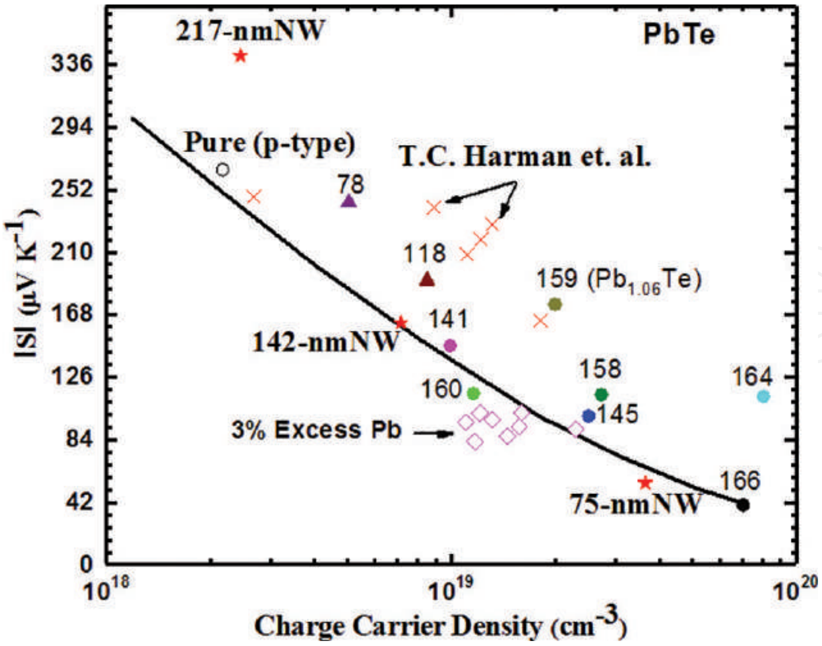

Figure 8. Absolute value of the thermoelectric power or Seebeck coefficient (S) of various PbTe samples [14] as a function of carrier density; electrons (n) or holes (h) at room temperature. The solid red stars denote the $Pb_{1.08}Te_{0.92}$ samples with 75, 142, and 217 nm diameter wires [27, 34].

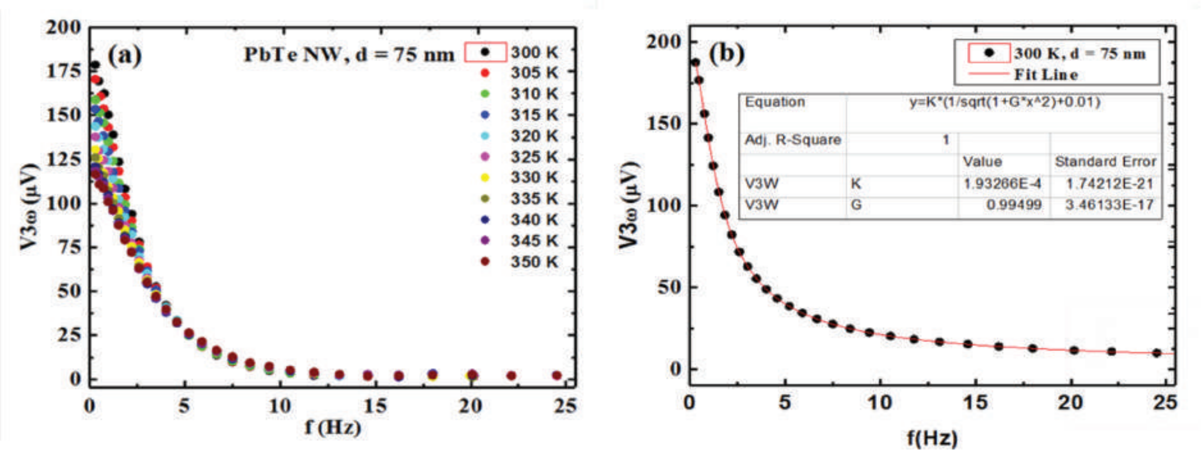

Figure 9. (a) Frequency dependence of $V_{3\omega}$ at 300–350 K for 75 nm PbTe NW and (b) the solid line is predicted relation $V_{3\omega} \propto 1/\sqrt{(1 + (2\omega\gamma)^2)}$ at 300 K for a 75 nm PbTe NW.

The thermal conductivity of the 75 nm PbTe nanowire was measured by the self-heating 3ω method [35] in the temperature range of 300–350 K. In the experiment, the $V_{3\omega}$ as a function of frequency will be attained. As shown in **Figure 9a**, the $V_{3\omega}$ was dependent on the frequency. The $V_{3\omega}$ reduce significantly by increasing the frequency, however, the reduction become slightly at a frequency above 10 Hz. The relation between thermal conductivity, $V_{3\omega}$ and frequency is described in the Eq. (1).

$$V_{3\omega} = \frac{4 I_0^3 R R' L}{\pi^4 \kappa S \sqrt{1 + (2\omega\gamma)^2}} \tag{1}$$

which simplified as:

$$y = \frac{K}{\sqrt{1 + Gx^2}} \tag{2}$$

where *I* and *ω* denote the amplitude and frequency of the alternating current applied on nanowire, R and R′ are the resistance and derivative of resistance at corresponding temperature, κ is the thermal conductivity, *S* is the cross section, and γ is the characteristic thermal time constant.

Figure 9b shows the fitting result of $V_{3\omega}$ to frequency of a 75 nm PbTe NW at 300 K. The thermal conductivity κ of the nanowire can be derived from the intercept of the fitting value at a certain temperature $V_{3\omega} = (4I_0^3 LRR')/(\pi^4 \kappa S)$ ($\omega\gamma \to 0$). To further validate the extraction of thermal conductivity by 3ω method, the variation of 3ω signals toward the input current amplitude I_0 and frequency was studied. The result shows that $V_3\omega$ versus I_0 follows the I_0^3, as exhibited in the equation of **Figure 10**, which mean it agree with the Eq. (1).

By substituting all acquired data from self-heating 3ω experiment to Eq. (1), the thermal conductivity, κ of a 75 nm PbTe NW at range temperature of 300–350 K were 0.96–0.72 $W m^{-1} K^{-1}$ (**Figure 11a** and **b**), which is approximately 2.40–3.19 times lower than the bulk counterpart (κ = 2.3 $W\ m^{-1}\ K^{-1}$). Likewise, the κ value at room temperature was 0.96 $W\ m^{-1}\ K^{-1}$, which is

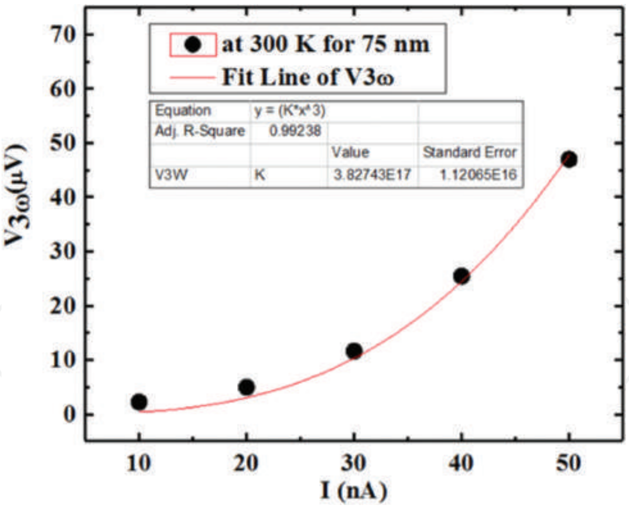

Figure 10. The 3rd harmonic voltage signal $V_{3\omega}$ as function of the extraction current amplitude I_0 for a 75 nm PbTe NW at 300 K. Red solid line represents the cubic relationship of $V_{3\omega}$ and I_0.

approximately 58% lower than the typical reported value of $\kappa = 2.3$ W m^{-1} K^{-1} for bulk PbTe. This decline mainly due to the carrier concentration difference or size effect. [36]

For the purpose of calculating the κ_l value, the electron thermal conductivity κ_e need to be determined. The κ_e value is calculated by using Eq. (3) (Wiederman-Franz law, where the Lorenz number $L = 2.44 \times 10^{-8}$ W.Ω.K^{-2}), while the κ_l is gained from subtracting the κ with κ_e value. The values of κ_l of a 75 nm PbTe NW at 300 K was 0.95 W m^{-1} K^{-1}, which is 57% lower than the PbTe bulk ($\kappa_l = 2.2$ W m^{-1} K^{-1}). [16] As reference, the lattice contribution (κ_l) of superlattice thin films $PbSe_{0.98}Te_{0.02}/PbTe$ at room temperature was 0.35 W m^{-1} K^{-1} [28].

$$\kappa_e = L.\sigma.T \tag{3}$$

The lattice thermal conductivity has a lower limit wherein the phonon mean free path becomes comparable to the lattice spacing of the atoms [37]. Alternatively, the lattice thermal conductivity of a material can be determined by using Eq. (4), where C, ν, andι represent the heat capacity per unit volume, the speed of sound in the material, and the mean free path of the phonons, respectively. By applying the atom spacing of PbTe as the minimum ι and substituting the values of the ν and C to Eq. (4), the κ_l of PbTe is around 0.2 W m^{-1} K^{-1}. Repeating this calculation for a variety of compounds, the lowest possible value of κ_l are in the range of 0.1–0.2 W m^{-1} K^{-1} [38].

$$\kappa_l = 1/3.C.\nu.\iota \tag{4}$$

As the size of the nanowire approaches the ι (the median phonon free path in PbTe is about 42 nm) [39], the κ value will drop due to the increased phonon scattering. According to the reported κ of individual PbTe NW with various diameters (d = 182, 277, and

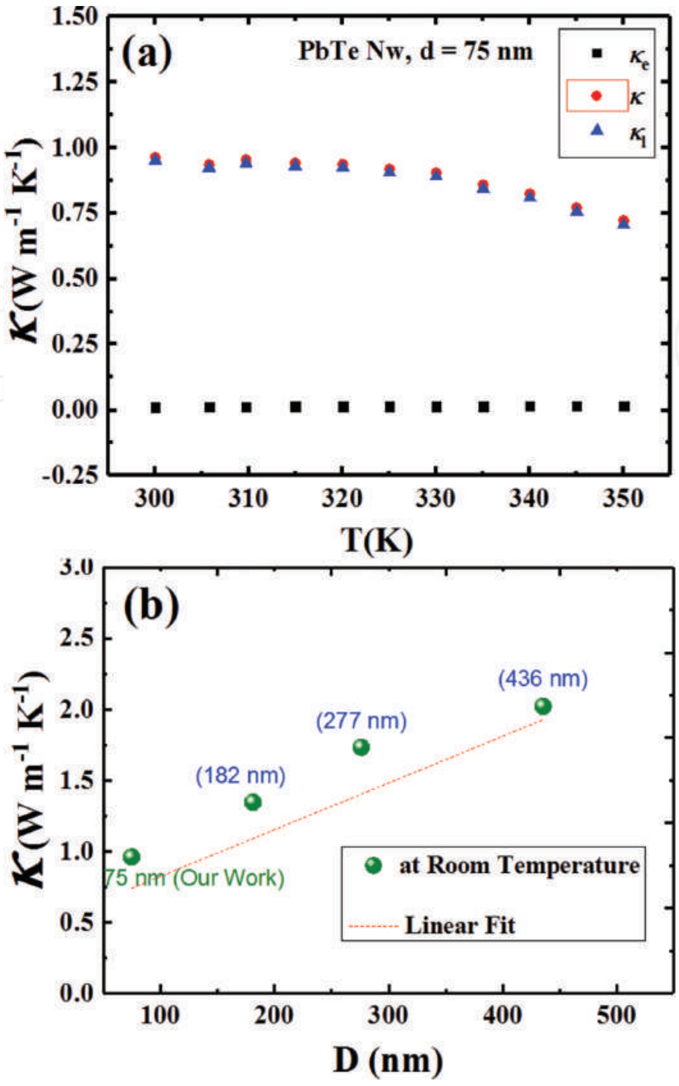

Figure 11. (a) Measured thermal conductivity κ(●), electron thermal conductivity κ_e (■) and lattice thermal conductivity κ_l (▲) of a 75 nm PbTe NW and (b) size-dependent κ properties of individual 75 nm PbTe NW (compared to the reported 182 nm, 277 nm and 436 nm [19].

436 nm) [19] including our recent work (d = 75 nm) which were plotted in **Figure 11b**, the κ value decreases gradually as its diameter shrinks. The enhanced phonon boundary scattering has a considerable effect in reducing the κ value of NW. Hence, it is suggested to have an effect on suppressing the phonon transport through the NWs as well [40, 41]. Theoretically, those phenomena would cause the *ZT* value of NW higher than the bulk counterpart, provided that the electronic properties were not degraded by the nanostructure. However, based upon all the above measurement results, i.e. S (−54.76 – −68.80 μV K^{-1}) [27], σ (1526.19–1878.68 S m^{-1}) [27] and κ (0.96–0.72 W m^{-1} K^{-1}), the obtained *ZT* value of a 75 nm PbTe NW at 300–350 K are in the range of ~1.4–4.3 x 10^{-3} (**Figure 12**) and it is still much lower than the ZT of PbTe bulk which is approximately ~ 0.25 at 300 K and maximal ~ 0.8 at 700 K [42].

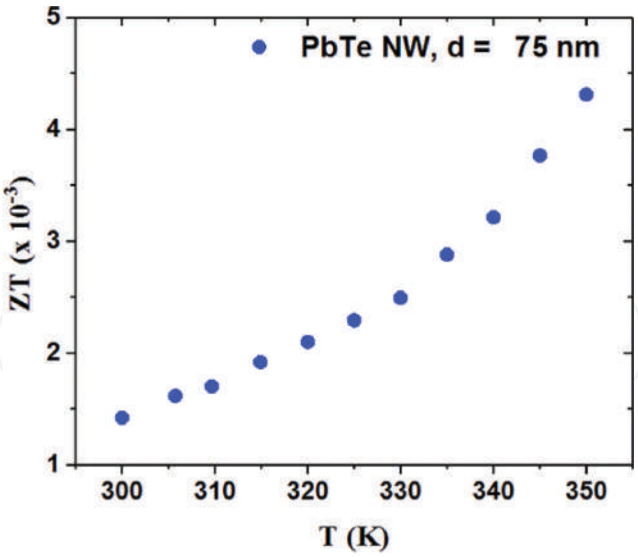

Figure 12. Figure of merit *ZT* for a n-type 75 nm PbTe NW.

4. Conclusions

In summary, we have demonstrated a new technique for structural characterization and TE properties measurement of individual single-crystalline PbTe NW by using a novel design of microchip. In this work, the single PbTe NW grown by the stress-induced method was employed for four different type of characterization simultaneously: structural characterization, Seebeck coefficient, electrical conductivity, and thermal conductivity. The structural characterization revealed that the synthesized PbTe NWs were single crystals with a growth along the [100] direction. While the TE properties (S, σ, and κ) of a 75 nm single-crystalline PbTe NW at room temperature are −54.76 μV K^{-1}, 1526.19 S m^{-1}, and 0.96 W m^{-1} K^{-1}, respectively. Based on those results, the experimental calculation of *ZT* value of its NW was ~1.4–4.3 x 10^{-3} at 300–350 K range. This technique provided high accuracy and reliable ZT value of individual single-crystalline TE NW. Thus, the size-dependent study of TE properties is very feasible. In this study, the κ value in growth [100] direction PbTe NW is size-dependent, wherein indicates that thermal transport through the individual PbTe nanowires is limited by boundary scattering of both electrons and phonons.

Acknowledgements

Technical support was provided by the Core Facilities for Nanoscience and Nanotechnology at the Institute of Physics of the Academia Sinica in Taiwan. This study was funded by the National Science Council of Taiwan (grant NSC 100-2112-M-001-019-MY3).

Conflict of interest

The authors declare no competing conflict of interests.

Author details

Dedi[1,3]*, Indah Primadona[2], Ping-Chung Lee[3], Chi-Hua Chien[3] and Yang-Yuan Chen[3]

*Address all correspondence to: dediamada@yahoo.com

1 Research Center for Electronics and Telecommunication, Indonesian Institute of Sciences, Bandung, Indonesia

2 Research Unit for Clean Technology, Indonesian Institute of Sciences, Bandung, Indonesia

3 Institute of Physics, Academia Sinica, Taipei, Taiwan

References

[1] DiSalvo FJ. Thermoelectric cooling and power generation. Science. 1999;**285**:703-706. DOI: 10.1126/science.285.5428.703

[2] Tritt TM. Thermoelectric materials: Holey and unholey semiconductors. Science. 1999;**283**:804-805. DOI: 10.1126/science.283.5403.804

[3] Dresselhaus MS, Chen G, Tang MY, Yang RG, Lee H, Wang DZ, Ren ZF, Fleurial JP, Gogna P. New directions for low-dimensional thermoelectric materials. Advanced Materials. 2007;**19**:1043-1053. DOI: 10.1002/adma.200600527

[4] Mahan GD. Good thermoelectrics solid state physics. Advances in Research and Applications. 1998;**51**:81-157. DOI: 10.1016/S0081-1947(08)60190-3

[5] Lin YM, Sun X, Dresselhaus MS. Theoretical investigation of thermoelectric transport properties of cylindrical bi nanowires. Physical Review B. 2000;**62**:4610-4623. DOI: 10.1103/PhysRevB.62.4610

[6] Bassi AL, Bailini A, Casari CS, Donati F, Mantegazza A, Passoni M, Russo V, Bottani CE. Thermoelectric properties of Bi–Te films with controlled structure and morphology. Journal of Applied Physics. 2009;**105**:124307(1-9). DOI: 10.1063/1.3147870

[7] Szczech JR, Higgins JM, Jin S. Enhancement of the thermoelectric properties in nanoscale and nanostructured materials. Journal of Materials Chemistry. 2011;**21**:4037-4055. DOI: 10.1039/C0JM02755C

[8] Hicks LD, Dresselhaus MS. Effect of quantum-well structures on the thermoelectric figure of merit. Physical Review B. 1993;**47**:12727-12731. DOI: 10.1103/PhysRevB.47.12727

[9] Hicks LD, Dresselhaus MS. Thermoelectric figure of merit of a one-dimensional conductor. Physical Review B. 1993;**47**:16631-16634. DOI: 10.1103/PhysRevB.47.16631

[10] Pei Y, Wang H, Gibbs ZM, LaLonde AD, Snyder GJ. Thermopower enhancement in Pb1−xMnxTe alloys and its effect on thermoelectric efficiency. NPG Asia Materials. 2012;**4**:e28. DOI: 10.1038/am.2012.52

[11] Rowe DM. CRC Handbook of Thermoelectrics. Boca Raton, FL, USA: CRC Press; 1995. p. 441

[12] Dughaish ZH. Lead telluride as a thermoelectric material for thermoelectric power generation. Physica B: Condensed Matter. 2002;**322**:205-223. DOI: 10.1016/S0921-4526(02)01187-0

[13] Heremans JP, Thrush CM, Morelli DT. Thermopower enhancement in lead telluride nanostructures. Physical Review B. 2004;**70**:115334(1-5). DOI: 10.1103/PhysRevB.70.115334

[14] Heremans JP, Thrush CM, Morelli DT. Thermopower enhancement in PbTe with Pb precipitates. Journal of Applied Physics. 2005;**98**:063703(1-6). DOI: 10.1063/1.2037209

[15] Orihashi M, Noda Y, Chen LD, Goto T, Hirai T. Effect of tin content on thermoelectric properties of p-type lead tin telluride. Journal of Physics and Chemistry of Solids. 2000;**61**:919-923. DOI: 10.1016/S0022-3697(99)00384-4

[16] LaLonde AD, Pei Y, Wang H, Snyder GJ. Lead telluride alloy thermoelectrics. Materials Today. 2011;**14**:526-532. DOI: 10.1016/S1369-7021(11)70278-4

[17] Wei Q, Lieber CM. Synthesis of single crystal bismuth-telluride and lead-telluride nanowires for new thermoelectric materials. Materials Research Society Symposium Proceedings. 2000;**581**:219-223. DOI: 10.1557/PROC-581-219

[18] Fardy M, Hochbaum AI, Goldberger J, Zhang MM, Yang P. Synthesis and thermoelectrical characterization of lead chalcogenide nanowires. Advanced Materials. 2007;**19**:3047-3051. DOI: 10.1002/adma.200602674

[19] Roh JW, Jang SY, Kang J, Lee S, Noh JS, Kim W, Park J, Lee W. Size-dependent thermal conductivity of individual single-crystalline PbTe nanowires. Applied Physics Letters. 2010;**96**:103101(1-3). DOI: 10.1063/1.3352049

[20] Lee SH, Shim W, Jang SY, Roh JW, Kim P, Park J, Lee W. Thermoelectric properties of individual single-crystalline PbTe nanowires grown by a vapor transport method. Nanotech. 2011;**22**:295707(1-6). DOI: https://doi.org/10.1088/0957-4484/22/29/295707

[21] Yang Y, Taggart DK, Cheng MH, Hemminger JC, Penner RM. High-throughput measurement of the seebeck coefficient and the electrical conductivity of lithographically patterned polycrystalline PbTe nanowires. Journal of Physical Chemistry Letters. 2010;**1**:3004-3011. DOI: 10.1021/jz101128d

[22] Yang Y, Kung SC, Taggart DK, Xiang C, Yang F, Brown MA, Guell AG, Kruse TJ, Hemminger JC, Penner RM. Synthesis of PbTe nanowire arrays using lithographically

patterned nanowire electrodeposition. Nano Letters. 2008;**8**:2447-2451. DOI: 10.1021/nl801442c

[23] Jung H, Park DY, Xiao F, Lee KH, Choa LH, Yoo B, Myung NV. Electrodeposited single crystalline PbTe nanowires and their transport properties. Journal of Physical Chemistry C. 2011;**115**:2993-2998. DOI: 10.1021/jp110739v

[24] Tai G, Zhou B, Guo W. Structural characterization and thermoelectric transport properties of uniform single-crystalline lead telluride nanowires. Journal of Physical Chemistry C. 2008;**112**:11314-11318. DOI: 10.1021/jp8041318

[25] Tai G, Guo W, Zhang Z. Hydrothermal synthesis and thermoelectric transport properties of uniform single-crystalline pearl-necklace-shaped PbTe nanowires. Crystal Growth & Design. 2008;**8**:2906-2911. DOI: 10.1021/cg701262x

[26] Yan Q, Chen H, Zhou W, Hng HH, Boey FYC, Ma J. A simple chemical approach for PbTe nanowires with enhanced thermoelectric properties. Chemistry of Materials. 2008;**20**:6298-6300. DOI: 10.1021/cm802104u

[27] Dedi, Lee PC, Chien CH, Dong GP, Huang WC, Chen CL, Tseng CM, Harutyunyan SR, Lee CH, Chen YY. Stress-induced growth of single-crystalline lead telluride nanowires and their thermoelectric transport properties. Applied Physics Letters. 2013;**103**:023115(1-5). DOI: 10.1063/1.4813606

[28] Caylor JC, Coonley K, Stuart J, Colpitts T, Venkatasubramanian R. Enhanced thermoelectric performance in PbTe-based superlattice structures from reduction of lattice thermal conductivity. Applied Physics Letters. 2005;**87**:023105(1-3). DOI: 10.1063/1.1992662

[29] Shim W, Ham J, Lee KI, Jeung WY, Johnson M, Lee W. On-film formation of bi nanowires with extraordinary electron mobility. Nano Letters. 2009;**9**:18-22. DOI: 10.1021/nl8016829

[30] Wang D, Sheriff BA, Heath JR. Complementary symmetry silicon nanowire logic: Power-efficient inverters with gain. Small. 2006;**2**:1153-1158. DOI: 10.1002/smll.200600249

[31] Partin DL, Heremans J, Morelli DT, Thrush CM, Olk CH, Perry TA. Growth and characterization of epitaxial bismuth films. Physical Review B: Condensed Matter. 1988;**38**:3818-3824. DOI: 10.1103/PhysRevB.38.3818

[32] Dekuijper AH, Bisschop J. Temperature dependence of concentrations and mobilities in thin bismuth films. Thin Solid Films. 1983;**110**:99-106. DOI: 10.1016/0040-6090(83)90214-6

[33] Horak J, Navratil J, Stary Z. Lattice point defects and free-carrier concentration in $Bi_{2+x}Te_3$ and $Bi_{2+x}Se_3$ crystals. Journal of Physics and Chemistry of Solids. 1992;**53**:1067-1072. DOI: 10.1016/0022-3697(92)90079-S

[34] Dedi, Idayanti N, Lee PC, Lee CH, Chen YY. Thermoelectric power of single crystalline lead telluride nanowire. Journal of Physics Conference Series. 2016;**776**:012046. DOI: 10.1088/1742-6596/776/1/012046

[35] Lu L, Yi W, Zhang D.L. 3ω method for specific heat and thermal conductivity measurements. The Review of Scientific Instruments. 2001;**72**:2996-3003. DOI: 10.1063/1.1378340

[36] Ioffe AF. Semiconductor Thermoelements and Thermoelectric Cooling. London: Infosearch; 1957

[37] Slack GA. The thermal conductivity of nonmetallic crystals. In: Ehreneich H, Seitz F, Turnbull D, editors. Solid State Physics. Vol. 34. New York: Academic Press; 1979. pp. 1-71. DOI: 10.1016/S0081-1947(08)60359-8

[38] Goldsmid HJ. A New Upper Limit to the Thermoelectric Figure-of-Merit. In: Rowe DM, editor. Thermoelectrics Handbook: Macro to Nano. CRC Taylor & Francis; 2006. p. 10.1-10.8

[39] Dames C, Chen G. Thermal Conductivity of Nanostructured Thermoelectric Material. In: Rowe DM, editor. Thermoelectrics Handbook: Macro to Nano. CRC Taylor & Francis; 2006. p. 42.1-42.11

[40] Li D, Wu Y, Kim P, Yang P, Majumdar A. Thermal conductivity of individual silicon nanowires. Applied Physics Letters. 2003;**83**:2934-2936. DOI: 10.1063/1.1616981

[41] Abouelaoualim D. Size effects on nanowire phonon thermal conductivity: A numerical investigation using the Boltzmann equation. Acta Physica Polonica A. 2007;**112**:49-54

[42] Tritt TM, Subramanian MA. Thermoelectric materials, phenomena, and applications: A bird’s eye view. MRS Bulletin. 2006;**31**:188-198. DOI: 10.1557/mrs2006.44

Chapter 10

Nonlinear Radiative Heat Transfer of Cu-Water Nanoparticles over an Unsteady Rotating Flow under the Influence of Particle Shape

K. Ganesh Kumar, B.J. Gireesha and S. Manjunatha

Additional information is available at the end of the chapter

http://dx.doi.org/10.5772/intechopen.74807

Abstract

A 3D study on Cu-water-rotating nanofluid over a permeable surface in the presence of nonlinear radiation is presented. Particle shape and thermophysical properties are considered in this study. The governing equations in partial forms are reduced to a system of nonlinear ordinary differential equations using suitable similarity transformations. An effective Runge-Kutta-Fehlberg fourth-fifth order method along with shooting technique is applied to attain the solution. The effects of flow parameters on the flow field and heat transfer characteristics were obtained and are tabulated. Useful discussions were carried out with the help of plotted graphs and tables. It is found that the rate of heat transfer is more enhanced in column-shaped nanoparticles when compared to tetrahedron- and sphere-shaped nanoparticles. Higher values of rotating parameter enhance the velocity profile and corresponding boundary layer thickness. It has quite the opposite behavior in angular velocity profile. Further, unsteady parameter increases the velocity profile and corresponding boundary layer thickness.

Keywords: particle shape effect, nonlinear radiation, Cu-water nanoparticles, unsteady rotating flow

1. Introduction

The interaction of thermal radiation has increased greatly during the last decade due to its importance in many practical applications. We know that the radiation effect is important under many isothermal and nonisothermal situations. If the entire system involving the polymer extrusion process is placed in a thermally controlled environment, then radiation could become important. The knowledge of radiation heat transfer in the system can, perhaps, lead to a desired product with a sought characteristic. Magnetohydrodynamic 3D flow of viscoelastic nanofluid in the presence of nonlinear thermal radiation has been examined by Hayat et al. [1]. Shehzad et al. [2] proposed the nonlinear thermal radiation in 3D flow of Jeffrey nanofluid. Refs. [3–11] are some of the works associated with stretching sheet problem of thermal radiation.

Nanotechnology has been widely utilized in the industries since materials with the size of nanometers possess distinctive physical and chemical properties. Nanofluids are literally a homogeneous mixture of base fluid and the nanoparticles. Common base fluids embody water, organic liquids, oil and lubricants, biofluids, polymeric solution and other common liquids. Nanoparticles are created from totally different materials, like oxides, nitrides, carbide, ceramics metals, carbons in varied (e.g., diamond, graphite, carbon nanotubes, fullerene) and functionalized nanoparticles. Nanofluids have novel properties that are potentially helpful in several applications in heat transfer, as well as microelectronics, pharmaceutical processes, heat exchanger, hybrid-powered engines, domestic refrigerator, fuel cells, cooling/vehicle thermal management, nuclear reactor agent, in grinding, in space technology, ships and in boiler flue gas temperature reduction. Choi [12] was the first who composed the analysis on nanoparticles in 1995. Later, Maiga et al. [13] initiated the heat transfer enhancement by using nanofluids in forced convective flows. The laminar fluid flow which results from the stretching of a flat surface in a nanofluid has been investigated by Khan and Pop [14]. Recently, a number of researchers are concentrating on nanofluid with different geometries; see [15–19].

Experimental studies have shown that the thermal conductivity of nanofluids is determined by the parameters related to: nanoparticles, concentration, size, spherical and nonspherical shapes, agglomeration (fractal-like shapes), surface charge and thermal conductivity, base fluids (e.g., thermal conductivity and viscosity), nanofluids (e.g., temperature), the interfacial chemical/physical effect or interaction between the particles and base fluid and others. For more details, readers are referred to the studies [20–25].

Impact of nonlinear thermal radiation on 3D flow and heat transfer of Cu-water nanoliquid over unsteady rotating flow have been considered. The heat transfer characteristics are studied in the presence of different particle shapes, thermophysical properties and nonlinear thermal radiation. The principal equations of continuity, momentum, energy and mass equations are transferred into a set of nonlinear similarity equalities by applying the appropriate transformations. The condensed equalities are solved numerically, and the impacts of relevant parameters are discussed through plotted graphs and tables.

2. Mathematical formulation

An unsteady laminar flow over a permeable surface in a rotating nanofluid is considered in this study. The copper-water motion is 3D due to Coriolis force in the present problem. The Cartesian coordinates are x, y and z where the rotation of the nanofluid is at an angular velocity $\overline{\Omega}(t)$ about the z-axis, and time is denoted as t. Let $u_w(x,t) = \frac{bx}{1-\delta t}$ and $v_w(x,t)$ represent the surface velocity in x and y directions, respectively, and $w_w(x, t)$ is the wall mass flux velocity in the z-direction as represented in **Figure 1**. Under these conditions, the governing equations can be written as:

$$\frac{\partial u}{\partial x} + \frac{\partial v}{\partial y} + \frac{\partial w}{\partial z} = 0, \tag{1}$$

$$\frac{\partial u}{\partial t} + u\frac{\partial u}{\partial x} + v\frac{\partial u}{\partial y} + w\frac{\partial u}{\partial z} - 2\overline{\Omega}v = -\frac{1}{\rho}\frac{\partial p}{\partial x} + \frac{\mu_{nf}}{\rho_{nf}}\frac{\partial^2 u}{\partial z^2}, \tag{2}$$

$$\frac{\partial v}{\partial t} + u\frac{\partial v}{\partial x} + v\frac{\partial v}{\partial y} + w\frac{\partial v}{\partial z} + 2\overline{\Omega}v = -\frac{1}{\rho}\frac{\partial p}{\partial y} + \frac{\mu_{nf}}{\rho_{nf}}\frac{\partial^2 v}{\partial z^2}, \tag{3}$$

$$\frac{\partial w}{\partial t} + u\frac{\partial w}{\partial x} + v\frac{\partial w}{\partial y} + w\frac{\partial w}{\partial z} = -\frac{1}{\rho}\frac{\partial p}{\partial z} + \frac{\mu_{nf}}{\rho_{nf}}\frac{\partial^2 v}{\partial z^2}, \tag{4}$$

$$\frac{\partial T}{\partial t} + u\frac{\partial T}{\partial x} + v\frac{\partial T}{\partial y} + w\frac{\partial T}{\partial z} = \alpha_{nf}\frac{\partial^2 T}{\partial z^2} + \frac{1}{(\rho c_p)_{nf}}\frac{\partial q_r}{\partial z}. \tag{5}$$

Boundary conditions for the problem are,

$$\begin{aligned} &u = u_w(x, t) = v = 0, w = 0, T = T_w \text{ at } z = 0, \\ &u \to 0, v \to 0, w = 0, T \to T_\infty \text{ as } z \to \infty \end{aligned} \tag{6}$$

where velocity components in x, y and z directions are u, v and w, constant angular velocity of the Nano fluid is Ω, dynamic viscosity of the Nano fluid is μ_{nf}, density of the nanofluid is ρ_{nf}, thermal diffusivity of the nanofluid is α_{nf}, T is temperature of nanofluid and wall temperature is T_w, T_∞ denotes temperature outside the surface (**Table 1**).

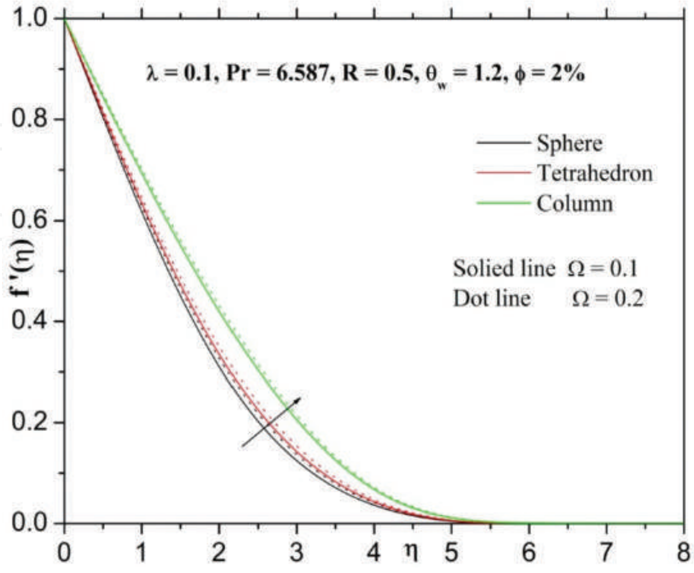

Figure 1. Influence of Ω on $f'(\eta)$.

The radiative heat flux expression in Eq. (5) is given by:

$$q_r = -\frac{16\sigma^*}{3k^*} T_\infty^3 \frac{\partial T}{\partial z} \tag{7}$$

where σ^* and k^* are the Stefan-Boltzmann constant and the mean absorption coefficient, respectively, and in view to Eq. (7), Eq. (4) reduces to:

$$\frac{\partial T}{\partial t} + u\frac{\partial T}{\partial x} + v\frac{\partial T}{\partial y} + w\frac{\partial T}{\partial z} = \frac{\partial}{\partial y}\left[\left(\alpha_{nf} + \frac{16\sigma^* T_\infty^3}{3(\rho c_p)_{nf} k^*}\frac{\partial T}{\partial Z}\right)\right]\frac{\partial T}{\partial y}. \tag{8}$$

Parameters μ_{nf}, ρ_{nf} and α_{nf} are interrelated with nanoparticle volume fraction; ϕ and can be defined as:

$$\begin{aligned} &\rho_{nf} = \rho_f\left(1 - \phi + \phi\left(\frac{\rho_s}{\rho_f}\right)\right), \mu_{nf} = \frac{\mu_f}{(1-\phi)^{2.5}}, \alpha_{nf} = \frac{k_{nf}}{(\rho c_p)_{nf}} \\ &(\rho c_p)_{nf} = (\rho c_p)_f\left(1 - \phi + \phi\left(\frac{(\rho c_p)_s}{(\rho c_p)_f}\right)\right), \frac{k_{nf}}{k_f} = \frac{[k_s + (m-1)k_f] - (m-1)\phi(k_f - k_s)}{[k_s + (m-1)k_f] + \phi(k_f - k_s)} \end{aligned} \tag{9}$$

where volumetric heat capacity of the solid nanoparticles is $(\rho c_p)_s$, volumetric heat capacity of the base fluid is $(\rho c_p)_f$, volumetric heat capacity of the nanofluid is $(\rho c_p)_{nf}$, thermal conductivity of the nanofluid is k_{nf}, thermal conductivity of the base fluid is k_f, thermal conductivity of the solid nanoparticles is k_s, nanoparticle volume fraction is ϕ, density viscosity of the base fluid is ρ_f and dynamic viscosity of the base fluid is μ_f (**Table 2**).

Now, we introduce similarity transformations:

$$u = \frac{bx}{1-\delta t}f'(\eta),\ v = \frac{bx}{1-\delta t}g(\eta),\ w = -\sqrt{\frac{bx}{1-\delta t}}f(\eta),\ \eta = \sqrt{\frac{bx}{v(1-\delta t)}}z,\ \theta(\eta) = \frac{T - T_\infty}{T_w - T_\infty} \tag{10}$$

with $T = T_\infty(1 + (\theta_w - 1)\theta)$ and $\theta_w = \frac{T_w}{T_\infty}$, $\theta_w > 1$ is the temperature ratio parameter.

	ρ	c_p	k
Copper (Cu)	385	8933	400
Water	997.1	4179	0.613

Table 1. Thermophysical properties of water and nanoparticles.

Particle shapes	**Sphere**	**Tetrahedron**	**Column**
m	3	4.0613	6.3698

Table 2. Values of the empirical shape factor for different particle shapes.

Using Eqs. (2)–(6) and (10), we can have

$$\frac{1}{(1-\phi)^{2.5}\left(1-\phi+\phi\left(\frac{\rho_s}{\rho_f}\right)\right)}f''' - \left[f'^2 - ff' - 2\Omega g + \lambda\left(\frac{\eta}{2}f'' + f'\right)\right] = 0, \tag{11}$$

$$\frac{1}{(1-\phi)^{2.5}\left(1-\phi+\phi\left(\frac{\rho_s}{\rho_f}\right)\right)}g'' - \left[f'g - fg' - 2\Omega f + \lambda\left(\frac{\eta}{2}g' + g\right)\right] = 0, \tag{12}$$

$$\frac{k_{nf}}{k_f\left(1-\phi+\phi\left(\frac{(\rho c_p)_s}{(\rho c_p)_f}\right)\right)}\left[1 + R(1+(\theta_w-1)\theta)^3\theta\right] - \Pr\left[\lambda\frac{\eta}{2}\theta' - f\theta'\right] = 0, \tag{13}$$

The transformed boundary conditions are as follows:

$$\begin{aligned} &f(0)=0, f'(0)=1, g(0)=0, \theta(0)=1 \ \text{ at } \ \eta=0 \\ &f'(\eta)\to 0, g(\eta)\to 0, \theta(\eta)\to 0 \ \text{ as } \ \eta\to\infty \end{aligned} \tag{14}$$

where $\Omega = \frac{\omega}{b}$ is rotation rate, $\lambda = \frac{\delta}{b}$ is unsteadiness parameter $R = \frac{16\sigma^* T_\infty^3}{3k_f k^*}$ is radiation parameter, $\Pr = \frac{\alpha_{nf}}{\upsilon_{nf}}$ is Prandtl number and primes denote the differentiation with respect to η.

Rosca et al. [11] mentioned that the pressure term (p) can be integrated from Eq. (4); thus, we obtain:

$$p = \upsilon\rho\frac{\partial w}{\partial z} - \frac{\rho w^2}{2} + c \tag{15}$$

The physical quantities of interest in this problem are the skin friction coefficients in x and y directions, C_{fx} and C_{fy} as well as the local Nusselt number Nu_x which are defined as:

$$C_{fx} = \frac{\tau_{wx}}{\rho u_w^2(xt)},\ C_{fy} = \frac{\tau_{wy}}{\rho u_w^2(yt)},\ Nu_x = \frac{xq_w}{k_f(T_w - T_\infty)}, \tag{16}$$

Surface shear stress τ_{wx}, τ_{wy} and surface heat flux q_w are defined as:

$$\tau_{wx} = \mu_{nf}\left(\frac{\partial u}{\partial z}\right)_{z=0},\ \tau_{wy} = \mu_{nf}\left(\frac{\partial v}{\partial z}\right)_{z=0} \text{ and } q_w = -k_{nf}\left(\frac{\partial T}{\partial z}\right) + qr_{z=0} \tag{17}$$

Using Eqs. (16) and (17), we obtain

$$\sqrt{\mathrm{Re}_x}C_{fx} = \frac{1}{(1-\phi)^{2.5}}f''(0),\ \sqrt{\mathrm{Re}_x}C_{fy} = \frac{1}{(1-\phi)^{2.5}}g'(0) \text{ and } \frac{Nu_x}{\sqrt{\mathrm{Re}_x}} = \frac{k_{nf}}{k_f}\left(-\left[1 + R\theta_w^3\right]\theta'(0)\right), \tag{18}$$

where $\mathrm{Re}_x = \frac{u_w x}{\upsilon}$ is local Reynolds number.

3. Numerical method

Numerical solutions of nonlinear coupled differential Eqs. (11)–(13) subject to the boundary conditions (14) constitute a two-point boundary value problem. Due to coupled and highly nonlinear nature, which are not amenable to closed-form solutions; therefore, we resorted to numerical solutions. In order to solve these equations numerically, we follow most efficient fourth-fifth order Runge-Kutta-Fehlberg integration scheme along with shooting technique. In this method, it is most important to choose the appropriate finite values of η_∞. The asymptotic boundary conditions at η_∞ were replaced by those at η_8 in accordance with standard practice in the boundary layer analysis.

4. Result and discussion

To get a clear insight into the physical situation of the present problem, numerical values for velocity and temperature profile are computed for different values of dimensionless parameters using the method described in the previous section. The numerical results for the local Nusselt number are presented for different values of the governing parameters in **Table 3**.

λ	Ω	**Pr**	R	θ_w	ϕ.	**Nusselt number**		
						$m = 3$	$m = \mathbf{4.0613}$	$m = \mathbf{6.3698}$
0.2						0.36722	0.35144	0.32983
0.3						0.29671	0.29256	0.28353
0.4						0.21897	0.22635	0.23028
	0.01					0.33069	0.32112	0.30611
	0.02					0.29005	0.28739	0.27973
	0.03					0.24936	0.25364	0.25333
		5.776				0.35865	0.34247	0.32053
		6.587				0.36722	0.35151	0.32990
		7.578				0.37598	0.36090	0.33978
			0.5			0.36722	0.35144	0.32983
			1			0.33266	0.31642	0.29491
			1.5			0.30957	0.29332	0.27217
				1.2		0.36722	0.35144	0.32983
				1.4		0.32565	0.31078	0.29076
				1.6		0.28807	0.27416	0.25572
					1%	0.43665	0.42492	0.40752
					2%	0.36722	0.35144	0.32983
					3%	0.30841	0.29212	0.27084

Table 3. Numerical values of Nusselt number for different physical parameters.

Figure 1 portrays the effect of Ω on velocity profile $f'(\eta)$. The velocity profile and corresponding thickness of the boundary layer enhance with larger values of Ω. This is because the larger value of Ω parameter leads to higher rotation rate as compared to stretching rate. Therefore, the larger rotation effect enhances velocity field. **Figure 2** shows the impact of Ω on angular profile $g(\eta)$. From this figure, one can see that $g(\eta)$ reduces for larger values of Ω. Further, it is noticed that rate of heat transfer is larger in column-shaped nanoparticles when compared to tetrahedron- and sphere-shaped nanoparticles.

Figures 3 and **4** depict the effect of λ on the $f'(\eta)$ and $g(\eta)$ profile. It is clear from both the figures that an increase in λ decreases the momentum boundary layer thickness resulting in velocity decrease. It is also noted that $g(\eta)$ decreases smoothly with the increase in the

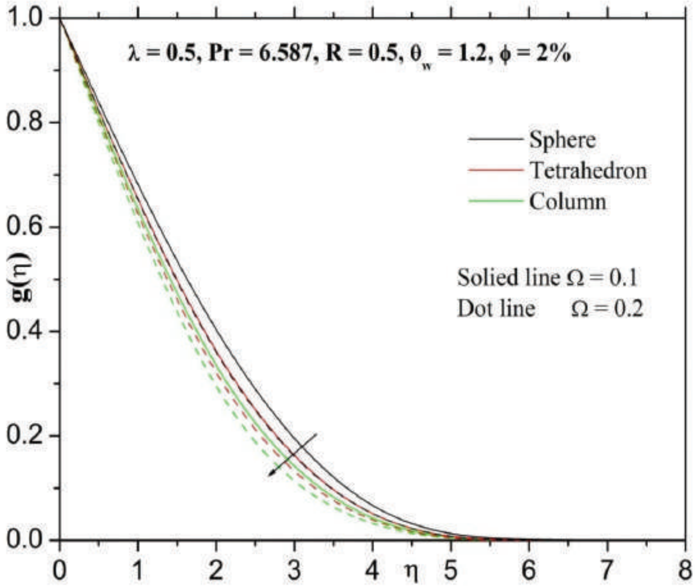

Figure 2. Influence of Ω on $g(\eta)$.

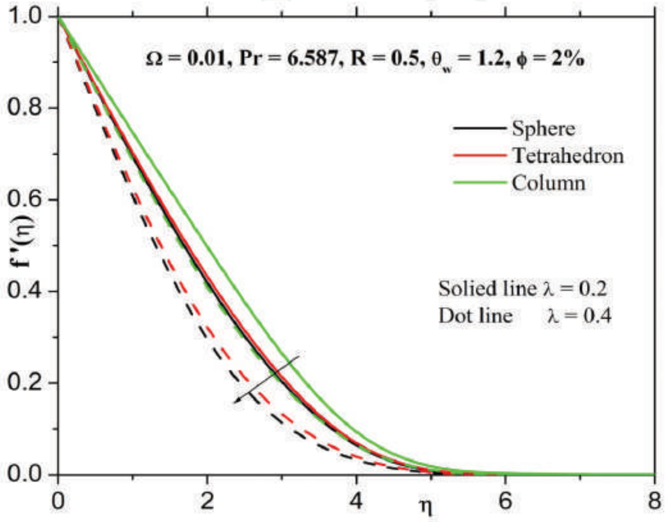

Figure 3. Influence of λ on $f'(\eta)$.

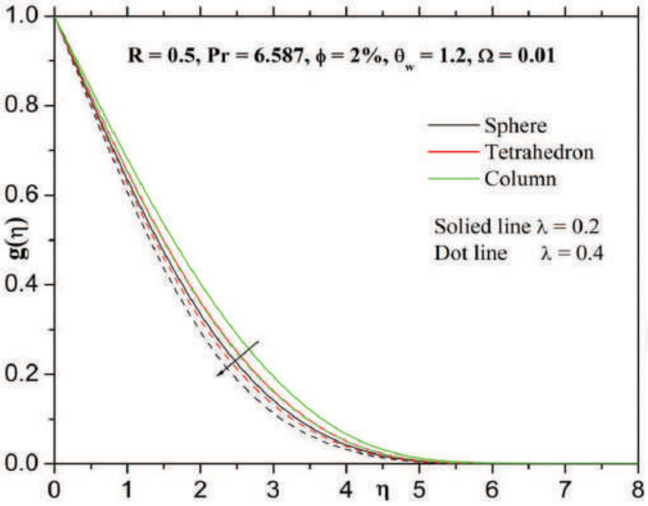

Figure 4. Influence of λ on $g(\eta)$.

unsteadiness parameter. This shows an important fact that the rate of cooling is much faster for higher values of λ, whereas it may take a longer time in steady flows.

Influence of the solid volume fraction parameter (ϕ) on temperature profiles $\theta(\eta)$ can be visualized in **Figure 5**. It is observed that the temperature profile increases by increasing values of the solid volume fraction parameter. This is due to the fact that the volume occupied by the dust particles per unit volume of mixture is higher so that it raises the rate of heat transfer. It was noticed that the development in the temperature profiles of column-shaped nanoparticles is high when compared to temperature profiles of sphere- and tetrahedron-shaped nanoparticles due to the increase in volume fraction of nanoparticles.

The effect of temperature ratio parameter (θ_w) on temperature profile is shown in **Figure 6**. The influence of temperature ratio parameter enriches the temperature profile and corresponding boundary layer thickness. This may happen due to the fact that the fluid temperature is much

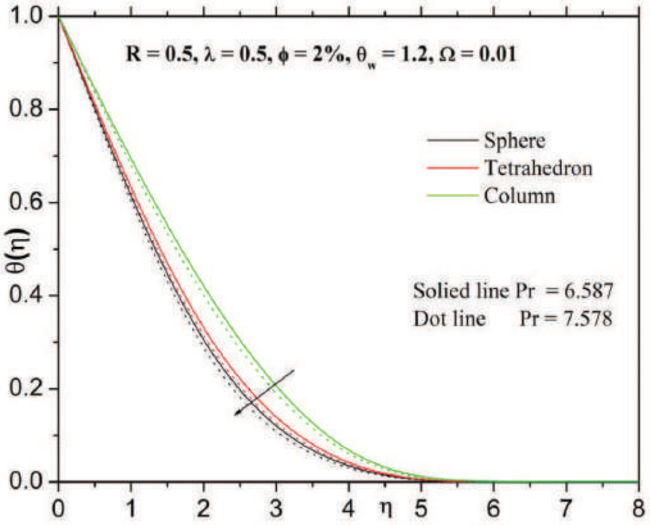

Figure 5. Influence of Pr on $\theta(\eta)$.

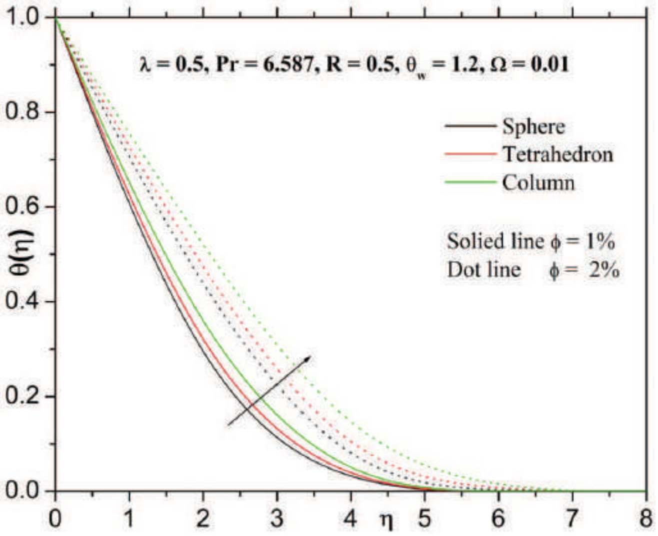

Figure 6. Influence of ϕ on $\theta(\eta)$.

higher than the ambient temperature for increasing values of θ_w, which increases the thermal state of the fluid. It is also observed that the rate of heat transfer is higher in the column-shaped nanoparticles than that of tetrahedron- and sphere-shaped nanoparticles.

Figure 7 demonstrates the effect of the Prandtl number (Pr) on temperature profiles of $\theta(\eta)$. The above mentioned graph elucidate that the temperature profile and corresponding thermal boundary layer thickness decrease rapidly with increasing values of Pr. Physically, the Prandtl number is the ratio of momentum diffusivity to thermal diffusivity. In fact, the larger Prandtl number means that the lower thermal diffusivity. A decrease in the thermal diffusivity leads to a decrease in the temperature and its associated boundary layer thickness.

The temperature distribution $\theta(\eta)$ for various values of radiation parameter (R) is shown in **Figure 8**. This figure reveals that the larger values of radiation parameter increase the temperature profile and thermal boundary layer thickness. Generally, higher values of

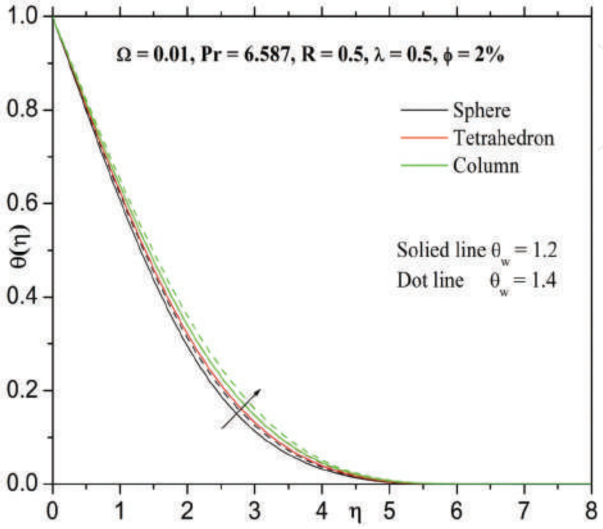

Figure 7. Influence of θ_w on $\theta(\eta)$.

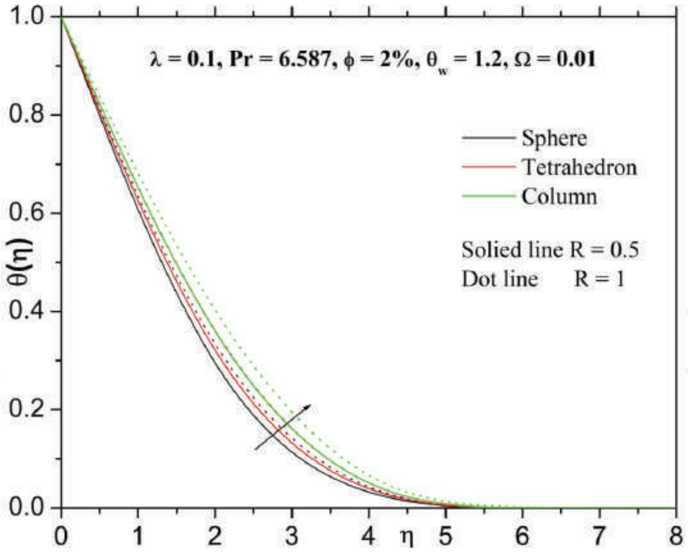

Figure 8. Influence of R on $\theta(\eta)$.

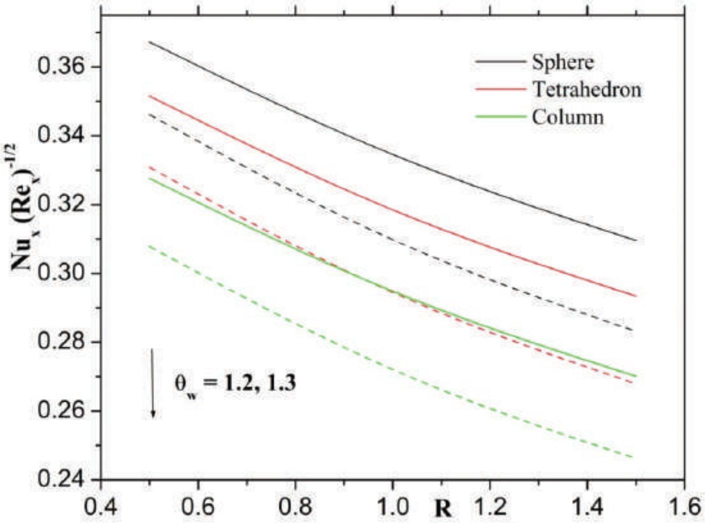

Figure 9. Influence of θ_w and R on Nusselt number.

radiation parameter produce additional heat to the operating fluid that shows associate enhancement within the temperature field. We have noticed an improvement within the temperature profile because of increase in the radiation parameter. Moreover, the rate of heat transfer at the wall is less in case of the sphere-shaped particles when compared to the tetrahedron- and column-shaped nanoparticles.

Figure 9 shows the effect of θ_w and R on the skin friction coefficient. Here, we observed that the skin friction coefficient decreases for larger values of θ_w and R. **Figure 10** delineates the influence of ϕ and Ec on Nusselt number. One can observe from the figure that Nusselt number decreases for larger values of ϕ and Ec. It is also perceived from these figures that the maximum decrease in the rate of heat transfer of nanofluid is motivated by the column-shaped, followed by

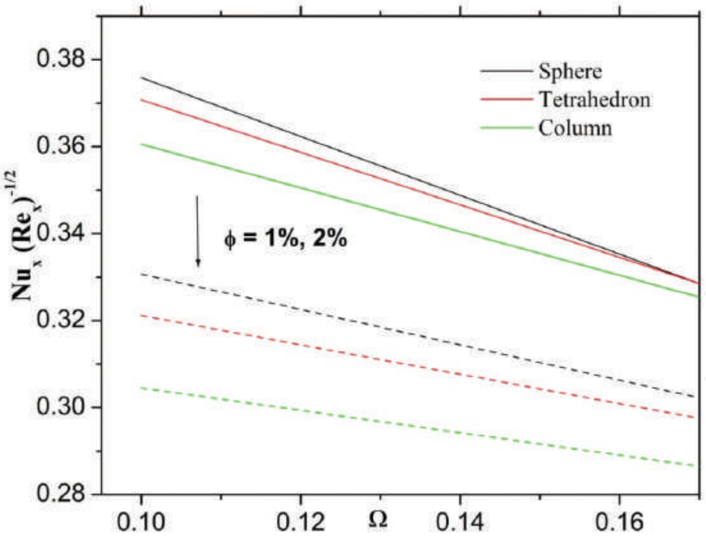

Figure 10. Influence of ϕ and Ω on Nusselt number.

tetrahedron- and sphere-shaped nanoparticles, respectively. It is just because of the nanofluid which contains column-shaped nanoparticles having maximum thermal conductivity than nanofluids containing tetrahedron- and sphere-shaped nanoparticles. **Table 3** presents the numerical values of Nusselt number for various values physical parameter values. It is observed that Nusselt number increases with increasing Pr. Further, from **Table 3**, we observe that Nusselt number decreases with increasing values of θ_w, R, ϕ and λ.

5. Conclusions

In the present analysis, impact nonlinear radiative heat transfer of Cu-water nanoparticles over an unsteady rotating flow under the influence of particle shape is considered. Effects of various parameters are studied graphically. The main points of the present simulations are listed as follows:

- The highlight of this study is that temperature profile is more enhanced in column-shaped nanoparticles when compared to tetrahedron- and sphere-shaped nanoparticles.
- Temperature profile and thermal boundary layer thickness increase with increasing values of R and θ_w.
- The thermal boundary layer thickness and temperature profile enhance with increasing values of ϕ.
- Higher values of rotating parameter enhance the velocity profile and corresponding boundary layer thickness. It has quite opposite behavior in angular velocity profile.
- Unsteady parameter increases the velocity profile and corresponding boundary layer thickness.

Author details

K. Ganesh Kumar[1], B.J. Gireesha[1] and S. Manjunatha[2]*

*Address all correspondence to: manjubhushana@gmail.com

1 Department of Studies and Research in Mathematics, Kuvempu University, Shimoga, Karnataka, India

2 Department of Engineering Mathematics, Faculty of Engineering, Christ University, Bengaluru, India

References

[1] Hayat T, Muhammad T, Alsaedi A, Alhuthali MS. Magnetohydrodynamic three-dimensional flow of viscoelastic nanofluid in the presence of nonlinear thermal radiation. Journal of Magnetism and Magnetic Materials. 2015;**385**:222-229

[2] Shehzad SA, Hayat T, Alsaedi A, Mustafa AO. Nonlinear thermal radiation in three-dimensional flow of Jeffrey nanofluid: A model for solar energy. Applied Mathematics and Computation. 2014;**248**:273-286

[3] Mustafa M, Mushtaq A, Hayat T, Alsaedi A. Radiation effects in three-dimensional flow over a bi-directional exponentially stretching sheet. Journal of the Taiwan Institute of Chemical Engineers. 2015;**47**:43-49

[4] Kafoussias NG, Williams EW. Thermal-diffusion and diffusion-thermo effects on mixed free-forced convective and mass transfer boundary layer flow with temperature dependent viscosity. International Journal of Engineering Science. 1995;**33**(9):1369-1384

[5] Srinivasacharya D, Kaladhar K. Mixed convection flow of couple stress fluid in a non-darcy porous medium with Soret and Dufour effects. Journal of Applied Science and Engineering. 2012;**15**:415-422

[6] Rudraswamy NG, Kumar KG, Gireesha BJ, Gorla RSR. Soret and Dufour effects in three-dimensional flow of Jeffery nanofluid in the presence of nonlinear thermal radiation. Journal of Nanoengineering and Nanomanufacturing. 2017;**6**(4):278-287

[7] Kumar KG, Rudraswamy NG, Gireesha BJ, Krishnamurthy MR. Influence of nonlinear thermal radiation and viscous dissipation on three-dimensional flow of Jeffrey nano fluid over a stretching sheet in the presence of joule heating. Nonlinear Engineering. 2017;**6**(3): 207-219

[8] Kumar KG, Gireesha BJ, Manjunatha S, Rudraswamy NG. Effect of nonlinear thermal radiation on double-diffusive mixed convection boundary layer flow of viscoelastic nanofluid over a stretching sheet. International Journal of Mechanical and Materials Engineering. 2017;**12**(1):18

[9] Kumar KG, Rudraswamy NG, Gireesha BJ, Manjunatha S. Nonlinear thermal radiation effect on Williamson fluid with particle-liquid suspension past a stretching surface. Results in Physics. 2017;**7**:3196-3202

[10] Makinde OD, Kumar KG, Manjunatha S, Gireesha BJ. Effect of nonlinear thermal radiation on MHD boundary layer flow and melting heat transfer of micro-polar fluid over a stretching surface with fluid particles suspension. Defect and Diffusion Forum. 2017;**378**: 125-136

[11] Rosca NC, Pop I. Mixed convection stagnation point flow past a vertical flat plate with a second order slip: Heat flux case. International Journal of Heat and Mass Transfer. 2013; **65**:102-109

[12] Choi CUS. Enhancing thermal conductivity of fluids with nanoparticles. Siginer DA, Wang HP, editors. Development and Applications of Non-Newtonian Flows. Vol. 231. MD: ASME; 1995. pp. 99-10

[13] Maiga SEB, Palm SJ, Nguyen CT, Roy G, Galanis N. Heat transfer enhancement by using nanofluids in forced convection flows. International Journal of Heat and Fluid Flow. 2005; **26**:530-546

[14] Khan W, Pop I. Boundary-layer flow of a nanofluid past a stretching sheet. International Journal of Heat and Fluid Flow. 2010;**53**(11–12):2477-2483

[15] Rudraswamy NG, Shehzad SA, Ganesh Kumar KG, Gireesha BJ. Numerical analysis of MHD three-dimensional Carreau nanoliquid flow over bidirectionally moving surface. Journal of the Brazilian Society of Mechanical Sciences and Engineering. 2017;**39**(12):5037-5047

[16] Kumar KG, Gireesha BJ, Prasannakumara BC, Ramesh GK, Makinde OD. Phenomenon of radiation and viscous dissipation on Casson nanoliquid flow past a moving melting surface. Diffusion Foundations. 2017;**11**:33-42

[17] Kumar KG, Ramesh GK, Gireesha BJ, Gorla RSR. Characteristics of Joule heating and viscous dissipation on three-dimensional flow of Oldroyd B nanofluid with thermal radiation. Alexandria Engineering Journal. 2017. DOI: 10.1016/j.aej.2017.06.006

[18] Prasannakumara BC, Gireesha BJ, Krishnamurthy MR, Kumar KG. MHD flow and nonlinear radiative heat transfer of Sisko nanofluid over a nonlinear stretching sheet. Informatics in Medicine Unlocked. 2017;**9**:123-132

[19] Kumar KG, Gireesha BJ, Prasannakumara BC, Makinde OD. Impact of chemical reaction on marangoni boundary layer flow of a Casson nano liquid in the presence of uniform heat source sink. Diffusion Foundations. 2017;**11**:22-32

[20] Ellahi R, Zeeshan A, Hassan M. Shape effects of nanosize particles in Cu-H_2O nanofluid on entropy generation. International Journal of Heat and Mass Transfer. 2015;**81**:449-456

[21] Ghosh MM, Ghosh S, Pabi SK. Effects of particle shape and fluid temperature on heat-transfer characteristics of nanofluids. Journal of Materials Engineering and Performance. 2013;**22**(6):1525-1529

[22] Jeong J, Li C, Kwon Y, Lee J, Kim SH, Yun R. Particle shape effect on the viscosity and thermal conductivity of ZnO nanofluids. International Journal of Refrigeration. 2013; **36**(8):2233-2241

[23] Timofeeva EV, Routbort JL, Singh D. Particle shape effects on thermophysical properties of alumina nanofluids. Journal of Applied Physics. 2009;**106**(1):014304-1-014304-10

[24] Ji Y, Wilson C, Chen H, Ma H. Particle shape effect on heat transfer performance in an oscillating heat pipe. Nanoscale Research Letters. 2011;**6**:296

[25] Sheikholeslami M, Gorji-Bandpay M, Ganji DD. Investigation of nanofluid flow and heat transfer in presence of magnetic field using KKL model. Arabian Journal for Science and Engineering. 2014;**39**(6):5007-5016

Thermal Conductivity of Graphite-Based Polymer Composites

Teboho Clement Mokhena,
Mokgaotsa Jonas Mochane, Jeremia Shale Sefadi,
Setumo Victor Motloung and
Dickson Mubera Andala

Additional information is available at the end of the chapter

http://dx.doi.org/10.5772/intechopen.75676

Abstract

It is well known that polymers are insulators, which limit their usage in other applications where thermal conductivity is essential for heat to be efficiently dissipated or stored. In the past, the improvement in the thermal conductivity of polym.rs with conductive fillers has been investigated by researchers. Carbon-based materials such as graphite, graphene and carbon nanotube, which feature excellent properties such as a high mechanical strength, a high thermal conductivity and a tailorable electronic configuration, have been added to different polymer matrices to enhance their thermal conductivity. Amongst others, graphite more especially expanded graphite merits special interest because of its abundant availability at a relatively low cost and lightweight when compared to other carbon allotropes. Herein, we describe the thermal conductivity of polymer/graphite composites and their applications.

Keywords: polymer, graphite composites, thermal conductivity, functionalization, applications

1. Introduction

Polymers can be moulded into various shapes and forms which afford their application in different fields [1–3]. This is owing to their unique properties such as lightweight, durability and low production cost. Polymers have substituted natural materials (e.g. steel and glass) in most of their former uses [1–3]. Besides these unique features, their success in certain applications is hindered by their poor electrical, thermal and mechanical properties. The incorporation of different fillers has been subject to researchers and scientists as a suitable solution to overcome these limitations. However, the resulting composite properties were found to be directly dependent on several aspects such as matrix-type, filler-type, interaction between the filler and polymer as well as the distribution of the filler within the polymeric matrix [4].

Research has escalated on the use of conductive fillers to improve not only the electrical and thermal conductivities but also the overall physical properties of the resulting composite product. Different conductive fillers such as metal powder, carbon black, carbon nanotubes (CNTs) and natural graphite were employed as reinforcing fillers of various polymeric materials [5, 6]. Amongst all these fillers, graphite garnered in much interest owing to its unique properties such as abundant availability, low cost and easy functionalization [7].

The polymer/graphite composites exhibited a high thermal conductivity and an electrical conductivity at a fairly low concentration. Polymer/graphite composites have been used in many applications including structural, aerospace and sporting goods. Most recently, researchers have focused their attention on the development of polymer/graphite composites for applications whereby thermal conductivity is needed [8, 9]. It is documented [7] in the study that the significance of thermal conductivity and/or thermal diffusivity in polymer composites is related to the need for considerable levels of thermal conductivity in circuit boards and heat exchangers. According to the studies [10], conductive composites are frequently used in wide applications such as heating elements, temperature-dependent sensors, self-limiting electrical heaters, switching devices, antistatic materials for electromagnetic interferences and shielding of electronic devices. This chapter reviews recent development on the thermal conductivity of polymer/graphite composites.

2. Graphite

Graphite is a carbon-based layered material whose structure is composed of successive layers of graphene sheets (carbon) and received much interest owing to its exceptional thermal, mechanical and electrical properties [5, 11, 12]. It is thermodynamically stable and soft with the successive layers being parallel to the base plane. The layers are bonded together by van der Waals forces. Graphite consists of carbons that are hexagonally bound to each other by covalent bonds with an interatomic separation of 0.142 nm and an interlayer separation of 0.335 nm. It is sp^2-hybridized with three of four valence electrons of hexagonally attached carbons that are linked to the valence electrons of the neighbouring carbon by σ-bonding. Therefore, the fourth electron resonates freely within the graphene layer but it is no longer interacting with a specific carbon atom. Van der Waals forces acting between adjacent graphene layers result from the delocalization of π-electrons. Thus, the interatomic interaction within the single graphene layer is stronger, that is, 75 times when compared to the interaction between the adjacent layers [11]. Hence, there has been much graphite modification that takes place in between the layers in order to improve its dispersion in different polymeric materials. Graphite can be classified into two types: natural and synthetic graphite as shown in **Figure 1**.

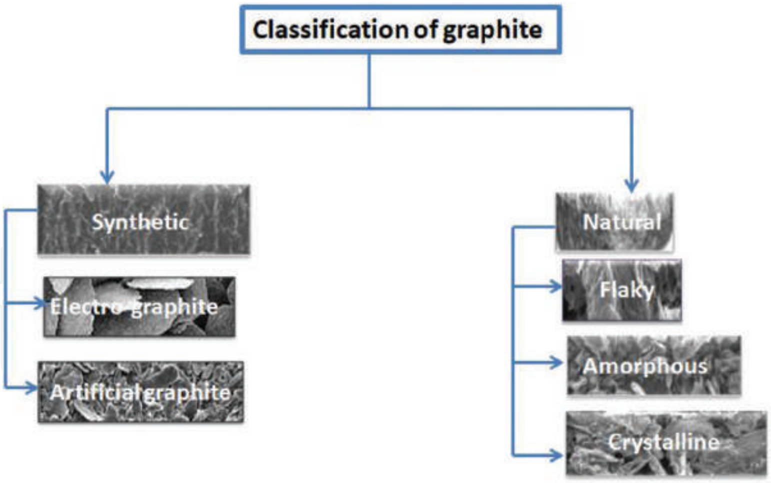

Figure 1. Schematic representation of graphite classification.

2.1. Natural graphite

Naturally occurring abundant graphite is classified into three categories depending on the geological environment, that is, amorphous, flake and highly crystalline [11]. Amorphous graphite has a content of graphite ranging from 25 to 85% depending on the geological conditions. It is usually derived from mesomorphic environment such as shale, slate and coal. Amorphous graphite is regarded as the less pure form of graphite with lack of considerable ordering and presence of microcrystalline structure. It has been applied in different applications where graphite is often utilized; however, its utilization depends on the degree of purity. Flake graphite is formed in either metamorphic or igneous geologic environments. It is obtained through froth floatation which results in 80–90% graphite. Flake graphite is less abundant as compared to amorphous graphite and has good electrical properties. It has been employed in various applications of graphite such as secondary steel manufacture, lubricants, pencils, powder metallurgy and coatings. Despite being found almost all over the world, crystalline (Vein/lump) graphite is commercially mined in Sri Lanka. It originates from crude oil deposits that through time, temperature and pressure were converted to graphite. As reflected by its name, it has a higher degree of crystallinity due to its direct deposition from a high-temperature fluid phase and its purity is more than 90%. Thus, it has good electrical and thermal conductivity. Vein graphite enjoyed its success in different applications such as batteries, lubricants, grinding wheels and powder metallurgy.

2.2. Synthetic graphite

Synthetic graphite is produced by treating carbonaceous precursors such as coal, petroleum and synthetic or natural organic chemicals in inert atmosphere to temperatures above 2400°C as well as thermal treatment of nongraphitic carbons, graphitization or chemical vapour deposition (CVD) from hydrocarbons under temperatures of 1883°C [11]. High temperatures are often employed to facilitate solid-state phase transition effect in order to produce graphite crystals. The production method is the primary factor that influences the resulting graphite properties. Synthetic graphite can also be categorized into two, that is, electro-graphite and artificial graphite. Electro-graphite is a pure carbon-shaped graphite produced from coal tar pitch and calcined petroleum pitch in the electric furnace, while artificial graphite results from the thermal treatment of calcined petroleum pitch at 2800°C. In general, the synthetic graphite has a low density, a high electrical resistance and porosity. Synthetic graphite is employed in different applications such as energy storage, carbon brushes and aerospace. Further modifications are often not required for its application in various fields. To avoid confusion, graphite will be used in this document without discriminate, whether it is synthetic or natural-based.

3. Modification of graphite

Modification of graphite has been subject of research in order to afford interaction with large polymer molecules and to achieve a better graphite dispersion [5, 11]. Many efforts have been done to overcome the absence of functional groups on the surface of graphite (or graphene sheets) and space between the sheets. There are three classic forms of modified graphite, that is, graphite-intercalated compounds (GICs), graphene oxide (graphite oxide (GO)) and expanded graphite (EG).

Graphite-intercalated compounds (*GICs*): GICs result from the insertion of atomic or molecular layers of different chemical species called intercalant between graphene sheets of the host graphite material [5, 12–14]. GIC can be categorized into two depending on the character of their bonding, that is, covalent GICs and ionic GICs. Covalent GICs include graphite oxide (GO), carbon monofluoride and tetracarbon monofluoride, whereas ionic GICs include graphite salts, graphite-alkali-metal compounds, graphite-halogen compounds and graphite-metal chloride compounds. Ionic GICs received much interest due to the capability of changing the electronic properties of graphite. The latter result in the presence of π-bonds in graphite that can accept/donate electrons from/to the intercalation. Further classification of ionic GICs depends on the staging of the GIC which is associated with the number of graphite layers between each intercalant layer. In the first stage (stage 1), the intercalant and graphite layers are alternating in which one layer of graphite is separated by one layer of intercalant. In a stage 2 GIC, there are two adjacent layers of graphite sheets between each intercalant layer. The intercalation of graphite results in increasing its interlayer spacing, weakening the interlayer interactions. The latter facilitate the exfoliation of the GICs by mechanical or thermal treatments.

Graphite oxide (*GO*): GOs are known as pseudo-two dimensional solid materials with covalent between the layers. Graphite oxide is often prepared by heat treatment of graphite flakes with oxidizing agents such that polar groups are introduced on the graphite surface [5, 15, 16]. This treatment also widens the interlayer spacing between the graphene sheets.

Expanded graphite (*EG*): The exposure of intercalated graphite to thermal treatment beyond critical temperature or microwave radiation leads to a large expansion of graphite flakes along the *c*-axis than in-plane direction as shown in **Figure 2**. The resulting material, which is known

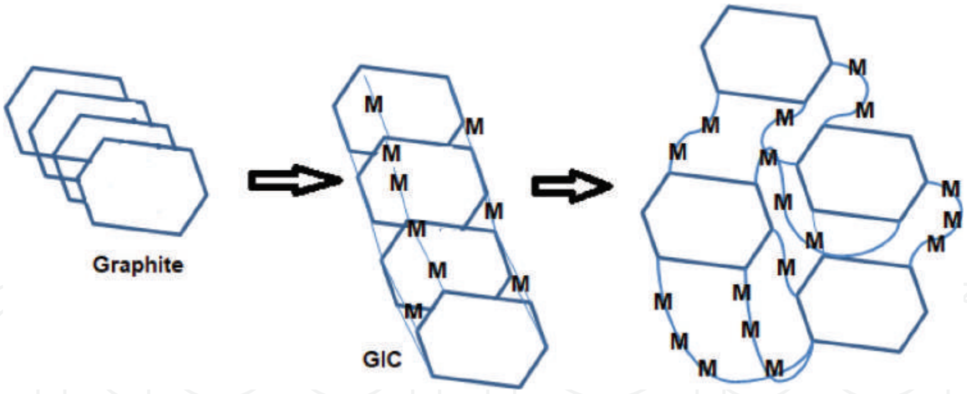

Figure 2. Schematic presentation of the preparation of expanded graphite (EG).

as expanded graphite (EG), has a vermicular or a worm-like structure with a low density, a high-temperature resistance and a high conductivity [6, 17, 18]. A mixture of sulphuric acid and nitric acid is usually employed for graphite intercalation followed by heat or microwave treatment to produce expanded graphite [5, 19].

Graphene: Graphene is a monolayer of sp^2-hybridized carbon atoms arranged in a two-dimensional lattice. It has been produced using different methods such as growth by chemical vapour deposition (both of discrete monolayers onto substrate and agglomerated powders), micro-mechanical exfoliation of graphite, and growth on crystalline silicon carbide [5]. These methods afford defect-free material with excellent physical properties; however, the yield is not large enough for use as a composite filler. The thermal conductivity of graphene ranges between 600 and 5000 W m^{-1} K^{-1} with Young modulus of 1 TPa and a tensile strength of 130 GPa [20].

4. Graphite composites

In order to broaden the applications of polymers, the incorporation of a suitable filler with required functionality is the most cost-effective and reliable method [17]. Some of the polymers fall short when it comes to electrical, thermal and mechanical as compared to ceramics and steel. However, the unique properties of polymers such as lightweight and mouldability into different shapes make them suitable candidates for various applications. Amongst other fillers, graphite features unique properties such as a high thermal and electrical conductivity, a low coefficient of thermal expansion, an exceptional thermal resistance, a high thermal shock resistance, improved stiffness and an increased strength. It is abundantly available and easily functionalized to afford various applications. The thermal conductivity of the graphite and/or its composites is of significant importance considering the demands as thermal conductance in heat exchangers, circuit boards, machinery, electronic appliances and many other applications as explained in Section 1.

4.1. Preparation of graphite composites

Beside the modification of graphite, the major contributor to the distribution of graphite in the polymeric matrix relies on the selected preparation method. Classic preparation methods for graphite/polymer composites are *in situ* polymerization, melt intercalation and solution-casting techniques [21–24]. Complete dispersion of the graphite particles leads to poor thermal conductivity due to lack of conductive network path within the composite product. **Figure 3** shows a schematic presentation of the resulting morphologies depending on the preparation method.

4.1.1. In situ polymerization

In situ polymerization involves the polymerization of monomer (or/and oligomer) in the presence of the filler [6, 21, 24–26]. This method is one of the most effective processes to facilitate the dispersion of the filler in the polymeric material. Moreover, it enhances strong interaction between the composite component; hence, the mechanical properties of the resulting composite are superior to the composite prepared by either solution casting or melt intercalation [25]. This technique, however, is associated with some limitations such as polymer and filler selection and limited to laboratory scale. Moreover, it is environmentally unfriendly process which makes it not feasible for composite preparation.

4.1.2. Solution casting

In solution casting, the polymer is dissolved in suitable solvents and then the filler is added into the polymer solution [22, 27]. In order to improve the dispersion of the fillers, the sonication step is usually adopted [27, 28]. Some polymers are, however, not soluble in most available solvents which then limit the choice of a polymer for this technique. This process is not environmentally friendly due to the fact that the solvent has to be evaporated from the system which can be harmful except if the solvent is water. For industrial production, this technique will be expensive with regard to the recovery of the solvent used. Nevertheless, the mechanical

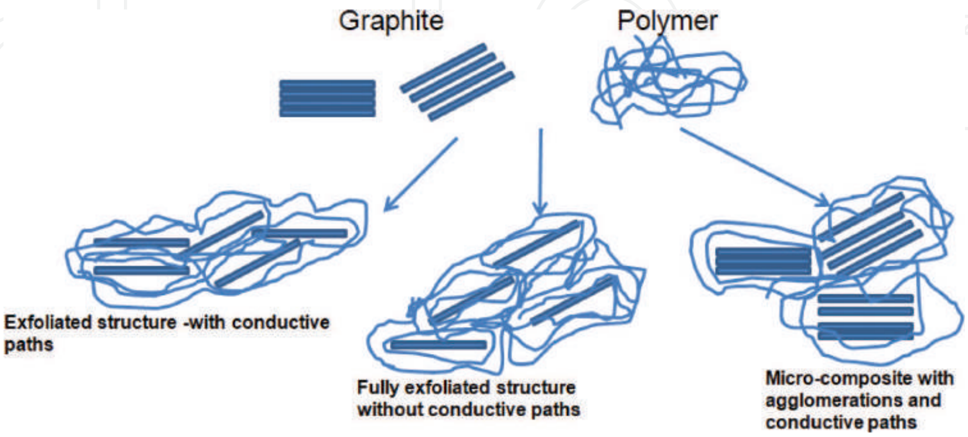

Figure 3. Different types of composites arising from and interaction between the host polymer and graphite layers obtained from different preparation methods.

properties of the resulting composites are superior to melt intercalation due to the sufficient time given for the filler to interact with each other as well as the polymeric matrix. A comparison between solution casting as well as solution casting followed by melt pressing was conducted by Bai et al. [22]. It was reported that solution-casted samples had high ability to form the percolated filler network as compared to solution casting followed by melt pressing. The percolation network is essential for the conduction paths within the composite material. However, the appropriate solvent can be chosen to avoid the formation of micro-voids within the composite [29]. The solution casting followed by hot pressing serves as a good procedure to eradicate the voids within the composite material [29].

4.1.3. Melt intercalation

Melt intercalation is the most favourable process with regard to industrial and environmental perspectives [23, 30, 31]. Polymer and filler are mixed together in the melt-compounding technique which leads to exposure to high shear and heat. The mixture is heated to a temperature above the melting temperature of the polymer for certain period to allow homogeneity. Classic compounding techniques include a single-screw extruder, a twin-screw extruder and an internal mixer. All these techniques can be utilized alone or in combination to afford better dispersion of the fillers. Injection moulding and/or melt pressing are usually used to mould the composite for characterization. In general, the percolation threshold is little bit higher than the other processing techniques, that is, solution casting and in situ polymerization [30]. Interestingly, the balance between the mechanical properties and other properties such as electrical conductivity can be achieved through this method which is of significance towards the commercialization of the resulting composite products. Its limitations involve the choice of polymer/filler, limited filler distribution and thermal degradation of the host polymer [23]. The properties of the polymer such as molecular weight, viscosity and chain length play a major role on the properties of the resulting composite product, hence influencing conclusions reached by different authors [11].

4.1.4. Other processing techniques

The combination of solution casting followed by melt intercalation/pressing has also been reported [28, 32, 33]. The main was to ensure the interaction between the fillers in order to promote the conductance path network within the host matrix. On the other hand, electrospun graphite composites were also reported in the study [34]. Despite the advantages associated with these techniques, *viz*. cost-effective, possibility of scaling up, control over the morphology of the resulting fibres and almost all polymers can be processed, there are only few studies based on the electrospun graphite composites [34, 35]. In situ melt mixing was carried out by mixing low-temperature expendable graphite with LDPE [36]. The expandable graphite expanded during the mixing process which is of significant importance considering the contact between the graphite particles. It is, however, recognized that such a process can lead to a large number of agglomeration with an increase in the filler's content. In the case of adhesive resins (e.g. epoxy resin), curing at a certain temperature over a certain period is usually utilized to prepare the composite products [37, 38].

5. Thermal conductivity

5.1. Graphite composites

Numerous researchers studied the thermal conductivity of polymer composites with regard to their importance to reach appreciable levels of thermal conductance in circuit boards, heat exchangers, appliances and machinery as summarized in **Table 1** [7, 17, 39]. Amongst all thermal conductive fillers, graphite merits special interest not only due to its high thermal conductivity, that is, 25–470 W m^{-1} K^{-1}, but high thermal stability, exceptional chemical resistance and mechanical properties [40]. A comparative study of the thermal conductivity between graphite and other conductive fillers (*viz*. copper powder (Cu), aluminium powder (Al), silver powder (Ag), zinc oxide (ZnO), boron nitride (BN), aluminium oxide (Al_2O_3) and diamond) particles was done by Fu et al. [37]. It was reported that the highest thermal conductivity was obtained at the filling load of 44.3 wt% of graphite due to the layered structure of graphite forming heat pathways within the matrix. The thermal conductivities of diamond (29.14%), Cu (68.25%), Al (69.69%), Al_2O_3 (67%) and BN (35.5%) were 0.35, 0.74, 1.11, 0.57 and 0.59 W m^{-1} K^{-1}, respectively. Although the resulting thermal conductivities were not true reflection of the thermal conductivity of the particles, this was related to the different structural arrangement within the particles which controls the contact between them. The

System	**Maximum particle content**	**Preparation method**	**Thermal conductivity (W m^{-1} K^{-1})**	**Refs.**
LDPE/graphite	10 vol.%	Melt mixing	6.5	[39]
HDPE/graphite	7%	Melt mixing	1.59	[40]
LDPE/low-temperature expandable graphite	50 wt%	Melt mixing followed by pan milling and dilution with neat LDPE	5.04	[51]
LDPE/untreated low-temperature expandable graphite	50 wt%	Melt mixing	7.02	[51]
LDPE/low-temperature expandable graphite (LTEG)	37 vol% (60 wt%)	Melt mixing	11.24	[36]
Ethylene vinyl acetate/natural graphite	7.5	Melt mixing	~0.29	[52]
Ethylene vinyl acetate/expanded graphite (EG)	7.5	Melt mixing	~0.31	[52]
Ethylene vinyl acetate/expanded graphite (EG)	4 phr	Solution casting followed by melt pressing	0.87	[33]
Ethylene vinyl acetate/natural graphite (NG)	4 phr	Solution casting followed by melt pressing	0.48	[33]
Epoxy resin/graphite	44.3 wt%	Oven curing	1.68	[37]
Epoxy resin/graphite	4.5 wt%	Oven curing	1.0	[38]
Epoxy resin/graphite	2 wt%	Oven curing	1.0	[50]

Table 1. Selected studies based on the thermal conductivity of graphite composites.

graphite being a cheaper material performed better than other expensive conductive particles. In general, the thermal conductivity increases almost linearly with an increase in graphite content, regardless of processing method as shown in **Figure 1** [39–43]. This can be attributed to the high thermal conductivity of the graphite when compared to pristine polymeric matrix.

Mu and Feng [41] prepared graphite/silicone rubber composites using solution-casting and melt-mixing processing techniques. They reported that the thermal conductivity increased with an increase in graphite content; however, solution-casted composites had a high conductivity as compared to melt-mixed ones. The authors reported that the thermal conductivity of solution-casted composites reached a value of 0.32 W m^{-1} K^{-1} at 9 per hundred rubber (phr) of graphite, whereas for melt-mixed it was only 0.24 W m^{-1} K^{-1}, which is the conductivity level similar to solution-casted composite at 4 phr. This was attributed to the conducting path networks created by contact between the graphite layers at a fairly low content in the case of solution casting compared to the reduction of surface-to-volume ratio in the case of melt mixing as shown in **Figure 4**. The latter resulted in a higher content of graphite required so that they can abut or contact in order to form the conducting paths. A comparison between two commercial graphite (EG-10, synthetic graphite, SGL Carbon, UK, and KS-15, synthetic graphite, Lonza, Switzerland) in two different polymeric matrices (high-density polyethylene (HDPE) and polystyrene (PS)) was conducted by Krupa and Chodák [7]. They reported a nonlinear increase of thermal conductivity with an increase in graphite content regardless of matrix and graphite type. It was, however, reported that the graphite KS displayed higher thermal conductivities than the thermal conductivities of EG-filled material especially for PS composites at a higher graphite content. The graphite KS had smaller particles with a narrow particle size distribution as well as a higher specific surface than graphite EG which corroborate the fact that the size of the particles did not influence the thermal conductivity, however, the contact between the graphite particles even if they are agglomerated. In another study, it was reported that the crystallinity of the polymer also plays a major role on the thermal conductivity of the resulting composite product [44]. It was reported that high-density polyethylene (HDPE)-based composites displayed high thermal conductivities over the whole graphite composition as compared to less crystalline low-density polyethylene (LDPE). Similarly, Deng et al. investigated the effect of chain structure on the thermal conductivity of expanded graphite/polymer composites [45]. Expanded graphite (EG) was blended with three different polymers, that is, polyphenylene sulphide (PPS), syndiotactic polystyrene (sPS) and amorphous polystyrene (aPS). The thermal conductivities of the neat aPS, sPS and PPS

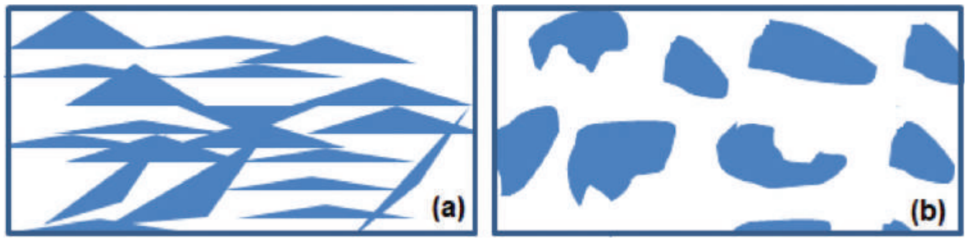

Figure 4. Schematic presentation of the proposed mechanism for thermal conductive paths for (a) solution-casted and (b) melt-mixed samples.

samples were reported as 0.18, 0.23 and 0.24, respectively. This was ascribed to the crystallinity of polymers. Similar result of observation was reported elsewhere in the study [46, 47]. The EG/PPS composites showed the highest thermal conductivity throughout the whole range in comparison to the two counterpart composites (**Figure 5**). The observed behaviour was attributed to the difference in polymer matrices with varied chain structures which may result in different crystallizations and interactions of composites.

Sefadi et al. [48] studied the influence of graphite treatment with sodium dodecyl sulphate (SDS) in water on the thermal conductivity. Moreover, the authors exposed the samples to 50-KGy electron beam irradiation to improve the interaction between graphite and ethylene vinyl acetate (EVA), as host matrix. They reported an increase in thermal conductivity with an increase in filler content due to high conductivity of graphite, regardless of the treatment. However, the thermal conductivity of the irradiated samples was slightly lower than unirradiated samples. This was attributed to the restriction of the polymer chains *via* cross-linking which reduced the vibration of phonons. There are a number of factors which contribute to the overall thermal conductivity of a composite product such as the dispersion of filler, matrix crystallinity and crystal structure, degree of interfacial thermal contact between the components, and scattering of phonons. Thus, these factors may counterbalance each other such that the obtained thermal conductivity does not reflect the percentage of the conductive filler added into the host matrix. For instance, Shen et al. [49] reported that the

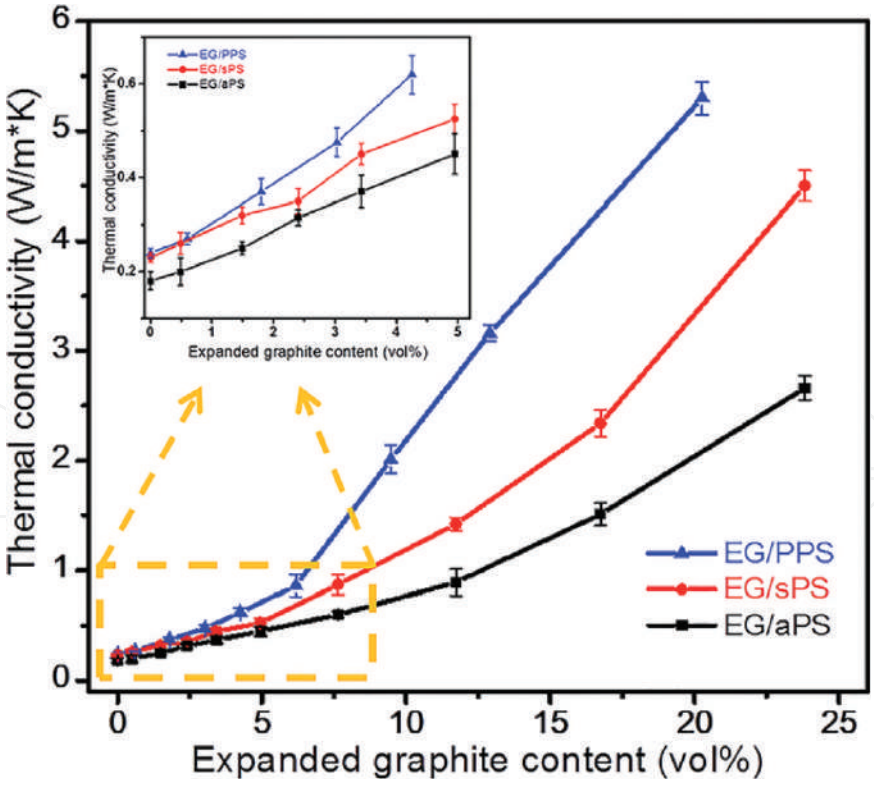

Figure 5. The thermal conductivity of EG/polymer composites as a function of EG volume contents (the error bar is marked). The inset shows the thermal conductivity at a low content [45].

functionalization of the filler can promote dispersion as well as interaction between composite components, but at the expense of thermal conductivity. Hence, it is of significant importance to choose functionalization of the filler while taking into account the lateral size of the filler for high thermal conductive materials. Li et al. [50] also reported that the treatment of the graphite with UV/O_3 did not have an influence on the thermal conductivity of the resulting composite materials. On the contrary, Wang and Tsai [20] reported that functionalized fillers exhibited superior thermal enhancements more than pristine filler. This was attributed to the increase in interfacial thermal conductivity (ITC) between the filler and the host matrix.

5.2. Graphite with other fillers (ternary systems)

There has been an ever-increasing interest in incorporating additional conductive filler into a graphite composite product to overcome the limitation of these materials [22, 31, 53–55]. It can be argued that the maximum thermal conductivity value achieved in graphite composites is 11.24 W m^{-1} K^{-1} (see **Table 1**). It is envisaged that the incorporation of the second filler can further enhance the thermal conductivity of the resulting composite products [31, 53, 56]. Lebedev et al. [53] reported that the inclusion of 1 wt% of carbon nanotubes (CNT) into polylactic acid (PLA)/natural graphite composites improved thermal conductivity by more than 40% of magnitude. The thermal conductivity was increased from 0.93 W m^{-1} K^{-1} for neat polymer to 2.73 W m^{-1} K^{-1} after the addition of 30 wt% graphite, whereas after the inclusion of 1 wt% CNT, the thermal conductivity value reached 3.8 W m^{-1} K^{-1}. This is ascribed to the additional CNT bridges which closely adjoin the surface of graphite. A similar study using HDPE as the polymeric matrix was recent conducted by Che et al. [31]. The authors reported that the thermal conductivity further increased with the addition of CNT compared to that with EG composites. In another study, it was demonstrated that a small content of a second filler, that is, below 2 wt%, has no significant influence on the thermal conductivity when compared to EG composites due to the fillers being wrapped in between the graphite layers [57]. A maximum increase of 38.5% compared to single filler-based composite was achieved at 5 wt% of the second filler. Self-hybrid composites of EG by crushing EG using a high-speed crusher to obtain different particle sizes were recently studied by Kim et al. [54]. The composites were prepared by mixing the crushed EG and raw EG with polycarbonate (PC) using melt extrusion. Hybrid composites (10 wt% crushed EG and raw EG) displayed a higher thermal conductivity by 12 and 20.7% compared to 20 wt% raw EG and crushed EG composites. The thermal conductivity value reached 2.62 W m^{-1} K^{-1} compared to 2.34 and 2.17 W m^{-1} K^{-1} for raw-EG and crushed EG-based composites due to synergistic effect. Various thermal conductive particles rather than carbon-based ones can also be used to enhance the thermal conductivity. Kostagiannakopoulou et al. [58] also reported that the thermal conductivity of the epoxy system increased significantly by increasing the filler content. However, the inclusion of the second filler, that is, multiwalled carbon nanotubes (MWCNTs) did improve the thermal conductivity at a higher graphite content (5, 10 and 15%). The highest enhancement percentage was 48 at 15% of graphite. The highest increase of ~176 was achieved in the case of 15% wt of the filler. A combination of graphite and aluminium nitride (AIN) was reported by Yuan et al. [59] and the thermal conductivity reached a value of

2.77 W m^{-1} K^{-1} that was 14.6 times that of neat polymeric matrix by combining only 50 wt% AIN and 6 wt% graphite.

6. Conclusions and remarks

The design of composites from graphite is inexpensive and available in abundance. This has initiated new ideas in the field of science for the development of a wide range of novel functional materials. Generally, the addition of graphite improved the thermal conductivity of the host polymer matrix irrespective of filler functionalization, the type of polymer and the method of preparation. Various processing techniques such as solvent casting melt blending and pan milling and masterbatch melt mixing have been used for the preparation of graphite composites. The type of mixing method seemed to have had an effect on the resultant thermal conductivity of the graphite/polymer composites. For instance, solution-casted composites had a high thermal conductivity as compared to melt-mixed system. It is understood that during solution casting, the EG particles will have a sufficient surface-to-volume ratio; as a result, they can contact easily and form conducting path networks at low EG contents. However, for melt mixing, one is of the idea that the EG particles' shape is changed during the melt-mixing process, resulting in a decrease of surface-to-volume ratio. Therefore, only a higher content of EG can contact and form conductive paths. Furthermore, the type of polymer had an influence on the thermal conductivity of the polymer/graphite composites, with the crystalline polymers having a higher thermal in the composites. It was further observed that the type of treatment on the graphite or its polymer composites also played a significant role in the improvement or non-improvement of the thermal conductivity of the polymer graphite composites. For example, the silane-treated graphite composites showed a higher thermal conductivity than the non-silane-treated graphite composites. In some cases, the treatment of the graphite with UV/O_3 did not have an influence on thermal conductivity of the resulting composite materials. Lately, the incorporation of the second filler with graphite can further enhance the thermal conductivity of the resulting composite products and widen the application of graphite composites.

Author details

Teboho Clement Mokhena[1], Mokgaotsa Jonas Mochane[1], Jeremia Shale Sefadi[2]*,
Setumo Victor Motloung[3] and Dickson Mubera Andala[4]

*Address all correspondence to: jeremia.sefadi@spu.ac.za

1 Department of Chemistry, University of Zululand, KwaDlangezwa, KwaZulu Natal, South Africa

2 Department of Chemistry, Sol Plaatje University, South Africa

3 Sefako Makgatho Health Science University, Medunsa, South Africa

4 Chemistry Department, Multimedia University of Kenya, Nairobi, Kenya

References

[1] Ho BT, Roberts TK, Lucas S. An overview on biodegradation of polystyrene and modified polystyrene: The microbial approach. Critical Reviews in Biotechnology. 2017;**38**(2):308-320. DOI: 10.1080/07388551.2017.1355293

[2] Restrepo-Flórez J-M, Bassi A, Thompson MR. Microbial degradation and deterioration of polyethylene-a review. International Biodeterioration & Biodegradation. 2014;**88**:83-90. DOI: 10.1016/j.ibiod.2013.12.014

[3] Wei R, Zimmermann W. Microbial enzymes for the recycling of recalcitrant petroleum-based plastics: How far are we? Microbial Biotechnology. 2017;**10**(6):1308-1322. DOI: 10.1111/1751-7915.12710

[4] Yasmin A, Luo J-J, Daniel IM. Processing of expanded graphite reinforced polymer nanocomposites. Composites Science and Technology. 2006;**66**(9):1182-1189. DOI: 10.1016/j.compscitech.2005.10.014

[5] Potts JR, Dreyer DR, Bielawski CW, Ruoff RS. Graphene-based polymer nanocomposites. Polymer. 2011;**52**(1):5-25. DOI: 10.1016/j.polymer.2010.11.042

[6] Chen G, Weng W, Wu D, Wu C. PMMA/graphite nanosheets composite and its conducting properties. European Polymer Journal. 2003;**39**(12):2329-2335. DOI: 10.1016/j.eurpolymj.2003.08.005

[7] Krupa I, Chodák I. Physical properties of thermoplastic/graphite composites. European Polymer Journal. 2001;**37**(11):2159-2168. DOI: 10.1016/S0014-3057(01)00115-X

[8] Ezquerra T, Kulescza M, Balta-Calleja F. Electrical transport in polyethylene-graphite composite materials. Synthetic Metals. 1991;**41**(3):915-920. DOI: 10.1016/0379-6779(91)91526-G

[9] Blaszkiewicz M, McLachlan DS, Newnham RE. The volume fraction and temperature dependence of the resistivity in carbon black and graphite polymer composites: An effective media-percolation approach. Polymer Engineering & Science. 1992;**32**(6):421-425. DOI: 10.1002/pen.760320606

[10] Klason C, MCQueen DH, Kubát J. Electrical Properties of Filled Polymers and Some Examples of Their Applications, Macromolecular Symposia. Manhattan, America: Wiley Online Library. 1996;**24**(2):110-117. DOI: 10.1002/masy.1996108012

[11] Nasir A, Kausar A, Younus A. Polymer/graphite nanocomposites: Physical features, fabrication and current relevance. Polymer-Plastics Technology and Engineering. 2015;**54**(7):750-770. DOI: 10.1080/03602559.2014.979503

[12] Dresselhaus MS, Dresselhaus G. Intercalation compounds of graphite. Advances in Physics. 2002;**51**(1):1-186. DOI: 10.1080/00018730110113644

[13] Smith RP, Weller TE, Howard CA, Dean MP, Rahnejat KC, Saxena SS, Ellerby M. Superconductivity in graphite intercalation compounds. Physica C: Superconductivity and Its Applications. 2015;**514**:50-58. DOI: 10.1016/j.physc.2015.02.029

[14] Xu J, Dou Y, Wei Z, Ma J, Deng Y, Li Y, Liu H, Dou S. Recent progress in graphite intercalation compounds for rechargeable metal (Li, Na, K, Al)-ion batteries. Advanced Science. 2017;**4**(10):1-14. DOI: 10.1002/advs.201700146

[15] Olanipekun O, Oyefusi A, Neelgund GM, Oki A. Synthesis and characterization of reduced graphite oxide–polymer composites and their application in adsorption of lead. Spectrochimica Acta Part A: Molecular and Biomolecular Spectroscopy. 2015;**149**:991-996. DOI: 10.1016/j.saa.2015.04.071

[16] Shin HJ, Kim KK, Benayad A, Yoon SM, Park HK, Jung IS, Jin MH, Jeong H-K, Kim JM, Choi J-Y, Lee YH. Efficient reduction of graphite oxide by sodium borohydride and its effect on electrical conductance. Advanced Functional Materials. 2009;**19**(12):1987-1992. DOI: 10.1002/adfm.200900167

[17] Mochane MJ, Motaung TE, Motloung SV. Morphology, flammability, and properties of graphite reinforced polymer composites. Systematic review. Polymer Composites. 2017. DOI: 10.1002/pc.24379

[18] Tsai K-C, Kuan H-C, Chou H-W, Kuan C-F, Chen C-H, Chiang C-L. Preparation of expandable graphite using a hydrothermal method and flame-retardant properties of its halogen-free flame-retardant HDPE composites. Journal of Polymer Research. 2011;**18**(4): 483-488. DOI: 10.1007/s10965-010-9440-2

[19] Shen X, Lin X, Jia J, Wang Z, Li Z, Kim J-K. Tunable thermal conductivities of graphene oxide by functionalization and tensile loading. Carbon. 2014;**80**:235-245. DOI: 10.1016/j.carbon.2014.08.062

[20] Wang T-Y, Tsai J-L. Investigating thermal conductivities of functionalized graphene and graphene/epoxy nanocomposites. Computational Materials Science. 2016;**122**:272-280. DOI: 10.1016/j.commatsci.2016.05.039

[21] Milani MA, González D, Quijada R, Basso NR, Cerrada ML, Azambuja DS, Galland GB. Polypropylene/graphene nanosheet nanocomposites by in situ polymerization: Synthesis, characterization and fundamental properties. Composites Science and Technology. 2013; **84**:1-7. DOI: 10.1016/j.compscitech.2013.05.001

[22] Bai Q-q, Wei X, Yang J-h, Zhang N, Huang T, Wang Y, Zhou Z-w. Dispersion and network formation of graphene platelets in polystyrene composites and the resultant conductive properties. Composites Part A: Applied Science and Manufacturing. 2017;**96**:89-98. DOI: 10.1016/j.compositesa.2017.02.020

[23] Anandhan S, Bandyopadhyay S. Polymer nanocomposites: From synthesis to applications. In: Nanocomposites and Polymers with Analytical Methods. Rijeka: InTech; 2011. DOI: 10.5772/17039

[24] Ding P, Su S, Song N, Tang S, Liu Y, Shi L. Highly thermal conductive composites with polyamide-6 covalently-grafted graphene by an in situ polymerization and thermal reduction process. Carbon. 2014;**66**:576-584. DOI: 10.1016/j.carbon.2013.09.041

[25] Patole AS, Patole SP, Kang H, Yoo J-B, Kim T-H, Ahn J-H. A facile approach to the fabrication of graphene/polystyrene nanocomposite by in situ microemulsion polymerization. Journal of Colloid and Interface Science. 2010;**350**(2):530-537. DOI: 10.1016/j.jcis.2010.01.035

[26] Zheng G, Wu J, Wang W, Pan C. Characterizations of expanded graphite/polymer composites prepared by in situ polymerization. Carbon. 2004;**42**(14):2839-2847. DOI: 10.1016/j.carbon.2004.06.029

[27] Guo H, Li X, Li B, Wang J, Wang S. Thermal conductivity of graphene/poly (vinylidene fluoride) nanocomposite membrane. Materials & Design. 2017;**114**:355-363. DOI: 10.1016/j.matdes.2016.11.010

[28] Zhang W-B, Zhang Z-x, Yang J-H, Huang T, Zhang N, Zheng X-T, Wang Y, Zhou Z-W. Largely enhanced thermal conductivity of poly (vinylidene fluoride)/carbon nanotube composites achieved by adding graphene oxide. Carbon. 2015;**90**:242-254. DOI: 10.1016/j.carbon.2015.04.040

[29] Ding P, Zhang J, Song N, Tang S, Liu Y, Shi L. Anisotropic thermal conductive properties of hot-pressed polystyrene/graphene composites in the through-plane and in-plane directions. Composites Science and Technology. 2015;**109**:25-31. DOI: 10.1016/j.compscitech.2015.01.015

[30] Han Y, Wu Y, Shen M, Huang X, Zhu J, Zhang X. Preparation and properties of polystyrene nanocomposites with graphite oxide and graphene as flame retardants. Journal of Materials Science. 2013;**48**(12):4214-4222. DOI: 10.1007/s10853-013-7234-8

[31] Che J, Wu K, Lin Y, Wang K, Fu Q. Largely improved thermal conductivity of HDPE/expanded graphite/carbon nanotubes ternary composites *via* filler network-network synergy. Composites Part A: Applied Science and Manufacturing. 2017;**99**:32-40. DOI: 10.1016/j.compositesa.2017.04.001

[32] Xiao Y-j, Wang W-y, Chen X-j, Lin T, Zhang Y-t, Yang J-h, Wang Y, Zhou Z-w. Hybrid network structure and thermal conductive properties in poly (vinylidene fluoride) composites based on carbon nanotubes and graphene nanoplatelets. Composites Part A: Applied Science and Manufacturing. 2016;**90**:614-625. DOI: 10.1016/j.compositesa.2016.08.029

[33] George JJ, Bhowmick AK. Ethylene vinyl acetate/expanded graphite nanocomposites by solution intercalation: Preparation, characterization and properties. Journal of Materials Science. 2008;**43**(2):702-708. DOI: 10.1007/s10853-007-2193-6

[34] Huang Z-X, Liu X, Wong S-C, Qu J-p. Electrospinning polyvinylidene fluoride/expanded graphite composite membranes as high efficiency and reusable water harvester. Materials Letters. 2017;**202**:78-81. DOI: 10.1016/j.matlet.2017.05.067

[35] Tu Z, Wang J, Yu C, Xiao H, Jiang T, Yang Y, Shi D, Mai Y-W, Li RKY. A facile approach for preparation of polystyrene/graphene nanocomposites with ultra-low percolation

threshold through an electrostatic assembly process. Composites Science and Technology. 2016;**134**:49-56. DOI: 10.1016/j.compscitech.2016.08.003

[36] Wu H, Lu C, Zhang W, Zhang X. Preparation of low-density polyethylene/low-temperature expandable graphite composites with high thermal conductivity by an in situ expansion melt blending process. Materials & Design (1980-2015). 2013;**52**:621-629. DOI: 10.1016/j.matdes.2013.05.056

[37] Fu Y-X, He Z-X, Mo D-C, Lu S-S. Thermal conductivity enhancement with different fillers for epoxy resin adhesives. Applied Thermal Engineering. 2014;**66**(1-2):493-498. DOI: 10.1016/j.applthermaleng.2014.02.044

[38] Wang Z, Qi R, Wang J, Qi S. Thermal conductivity improvement of epoxy composite filled with expanded graphite. Ceramics International. 2015;**41**(10):13541-13546. DOI: 10.1016/j.ceramint.2015.07.148

[39] Lebedev SM, Gefle OS. Evaluation of electric, morphological and thermal properties of thermally conductive polymer composites. Applied Thermal Engineering. 2015;**91**:875-882. DOI: 10.1016/j.applthermaleng.2015.08.046

[40] Ye CM, Shentu BQ, Weng ZX. Thermal conductivity of high density polyethylene filled with graphite. Journal of Applied Polymer Science. 2006;**101**(6):3806-3810. DOI: 10.1002/app.24044

[41] Mu Q, Feng S. Thermal conductivity of graphite/silicone rubber prepared by solution intercalation. Thermochimica Acta. 2007;**462**(1-2):70-75. DOI: 10.1016/j.tca.2007.06.006

[42] Mochane M, Luyt A. The effect of expanded graphite on the flammability and thermal conductivity properties of phase change material based on PP/wax blends. Polymer Bulletin. 2015;**72**(9):2263-2283. DOI: 10.1007/s00289-015-1401-9

[43] Mochane M, Luyt A. The effect of expanded graphite on the thermal stability, latent heat, and flammability properties of EVA/wax phase change blends. Polymer Engineering & Science. 2015;**55**(6):1255-1262. DOI: 10.1002/pen.24063

[44] Krupa I, Novák I, Chodák I. Electrically and thermally conductive polyethylene/graphite composites and their mechanical properties. Synthetic Metals. 2004;**145**(2-3):245-252. DOI: 10.1016/j.synthmet.2004.05.007

[45] Deng S, Wang J, Zong G, Chen F, Chai S, Fu Q. Effect of chain structure on the thermal conductivity of expanded graphite/polymer composites. RSC Advances. 2016;**6**(12):10185-10191. DOI: 10.1039/c5ra26272k

[46] Hay J, Luck D. The conformation of crystalline poly (phenylene sulphide). Polymer. 2001;**42**(19):8297-8301. DOI: 10.1016/S0032-3861(01)00335-4

[47] Langer L, Billaud D, Issi J-P. Thermal conductivity of stretched and annealed poly (p-phenylene sulfide) films. Solid State Communications. 2003;**126**(6):353-357. DOI: 10.1016/S0038-1098(03)00110-8

[48] Sefadi JS, Luyt AS, Pionteck J, Piana F, Gohs U. Effect of surfactant and electron treatment on the electrical and thermal conductivity as well as thermal and mechanical properties of

ethylene vinyl acetate/expanded graphite composites. Journal of Applied Polymer Science. 2015;**132**(32). DOI: 10.1002/app.42396

[49] Shen X, Wang Z, Wu Y, Liu X, Kim J-K. Effect of functionalization on thermal conductivities of graphene/epoxy composites. Carbon. 2016;**108**:412-422. DOI: 10.1016/j.carbon.2016.07.042

[50] Li J, Sham ML, Kim J-K, Marom G. Morphology and properties of UV/ozone treated graphite nanoplatelet/epoxy nanocomposites. Composites Science and Technology. 2007;**67**(2):296-305. DOI: 10.1016/j.compscitech.2006.08.009

[51] Wu H, Sun X, Zhang W, Zhang X, Lu C. Effect of solid-state shear milling on the physicochemical properties of thermally conductive low-temperature expandable graphite/low-density polyethylene composites. Composites Part A: Applied Science and Manufacturing. 2013;**55**:27-34. DOI: 10.1016/j.compositesa.2013.08.009

[52] Tavman I, Çeçen V, Ozdemir I, Turgut A, Krupa I, Omastova M, Novak I. Preparation and characterization of highly electrically and thermally conductive polymeric nanocomposites. Archives of Materials Science. 2009;**40**(2):84-88

[53] Lebedev S, Gefle O, Amitov E, Berchuk DY, Zhuravlev D. Poly (lactic acid)-based polymer composites with high electric and thermal conductivity and their characterization. Polymer Testing. 2017;**58**:241-248. DOI: 10.1016/j.polymertesting.2016.12.033

[54] Kim HS, Na JH, Jung YC, Kim SY. Synergistic enhancement of thermal conductivity in polymer composites filled with self-hybrid expanded graphite fillers. Journal of Non-Crystalline Solids. 2016;**450**:75-81. DOI: 10.1016/j.jnoncrysol.2016.07.038

[55] Kim HS, Kim JH, Yang C-M, Kim SY. Synergistic enhancement of thermal conductivity in composites filled with expanded graphite and multi-walled carbon nanotube fillers via melt-compounding based on polymerizable low-viscosity oligomer matrix. Journal of Alloys and Compounds. 2017;**690**:274-280. DOI: 10.1016/j.jallcom.2016.08.141

[56] Yu A, Ramesh P, Sun X, Bekyarova E, Itkis ME, Haddon RC. Enhanced thermal conductivity in a hybrid graphite nanoplatelet–carbon nanotube filler for epoxy composites. Advanced Materials. 2008;**20**(24):4740-4744. DOI: 10.1002/adma.200800401

[57] Wu K, Xue Y, Yang W, Chai S, Chen F, Fu Q. Largely enhanced thermal and electrical conductivity via constructing double percolated filler network in polypropylene/expanded graphite-multi-wall carbon nanotubes ternary composites. Composites Science and Technology. 2016;**130**:28-35. DOI: 10.1016/j.compscitech.2016.04.034

[58] Kostagiannakopoulou C, Fiamegkou E, Sotiriadis G, Kostopoulos V. Thermal conductivity of carbon nanoreinforced epoxy composites. Journal of Nanomaterials. 2016;**2016**:1-12. DOI: 10.1155/2016/1847325

[59] Yuan W, Xiao Q, Li L, Xu T. Thermal conductivity of epoxy adhesive enhanced by hybrid graphene oxide/AlN particles. Applied Thermal Engineering. 2016;**106**:1067-1074. DOI: 10.1016/j.applthermaleng.2016.06.089

IntechOpen